Computational Fluid Dynamics and Process Co-simulation Applied to Carbon Capture Technologies

Yang Fei

Submitted in accordance with the requirements for the degree of
Doctor of Philosophy

The University of Leeds
Energy Technology Innovation Initiative
School of Chemical and Process Engineering

September, 2015

The candidate confirms that the work submitted is his own, except where work which has formed part of jointly authored publications has been included. The contribution of the candidate and the other authors to this work has been explicitly indicated below. The candidate confirms that appropriate credit has been given within the thesis where reference has been made to the work of others.

The work performed in Chapter 6 of this thesis has been published in the following publication:

Y. Fei, S. Black, J. Szuhánszki, L. Ma, D.B. Ingham, P.J. Stanger, M. Pourkashanian, Evaluation of the potential of retrofitting a coal power plant to oxy-firing using CFD and process co-simulation, Fuel Processing Technology, 131 (2015) 45-58.

I developed the reduced order models in order to link the CFD predictions to the process modelling and also developed the oxy-coal power plant process model. Sandy Black and Janos Szuhanszki provided valuable assistance in setting up the CFD models. Penelope Stange gave meaningful suggestions on the process power plant. Lin Ma, Derek Ingham and Mohammed Pourkashanian are supervisors who provided helpful guidance on the overall direction and innovation for the research.

Acknowledgements

I would like to pass my thanks to Dr. Lin Ma for leading me the right way to learn and understand the background of chemical engineering; you always discussed with me so patiently on every academic or daily issue and helped me find the right way to work out problems. I would like to express my gratitude to Prof. Derek Ingham whose profound knowledge and kind personality continuously inspired me and he was always ready to help me with professional advices and experience. My sincere thanks should also go to Dr. Kevin Hughes, who helped me with so many academic and software issues. Thank you Prof. Mohamed Pourkashanian for always encouraging me with a big smile and providing professional suggestions when I was worried about the simulation results or the research progress. Thank you Prof. Gale, for spending so much time and energy to offer me strong support after the ETII team's move to Sheffield. Also I would like to thank Sandy Black and Alastair Clements for helping me with CFD simulations. Thank Janos Szuhánszki for providing me the experimental data for the 250 kW_{th} combustion test facility in Chapter 4.

My best friend Wen-lei Luo in Leeds, I remember the first day when I came to Leeds and it was you that picked me up at the train station in the midnight.

I would like to acknowledge the China Scholarship Council and ETII, University of Leeds, for providing me with the financial support to perform this research work. RWE npower is acknowledged for the MOPEDS validation data. EPSRC is acknowledged for the meaningful support.

Abstract

In the energy supply sector, coal will still remain as a dominate role in the foreseeable future because: it is comparatively cheap and widely distributed around the world and more importantly, carbon capture and storage (CCS) technologies make it possible to depend on coal with almost zero emission of carbon dioxide (CO_2). CCS involves capturing and purifying CO_2 from the emission source and then sequestering it safely and securely to avoid emission to the atmosphere. Both the post-combustion and the oxy-fuel technologies can be applied to existing power plants for CCS retrofit. Accurate prediction of the performance of a CCS plant plays an important role in reducing the technical risk of future integration of CCS with existing power plants. This research combines the fundamental computational fluid dynamics (CFD) and system process simulation technologies so that an efficient co-simulation strategy can be achieved.

A 250 kW_{th} coal combustion facility combined with a CO_2 post capture plant is taken to test the conception of the CFD and process co-simulation approach. The CFD models are employed to account for the combustion facility and the predicted results on the outlet gas compositions, temperatures and mass flow rates are used to generate reduced order models to linked to the model for the PACT CO_2 post capture plant so that a pilot scale whole plant model is achieved and validations have been made where it is possible.

Afterwards, the a large scale conventional air-coal firing power plant is taken into investigation: the CFD models for the boiler and the process models for the whole plant have been developed. Further, the potential of retrofitting this power plant to oxy-firing is evaluated using a CFD and process co-simulation approach. The CFD techniques are employed to simulate the coal combustion and heat transfer to the furnace water walls and heat exchangers under air-firing and oxy-firing conditions. A set of reduced order models has been developed to link the CFD predictions to the whole plant

process model in order to simulate the performance of the power plant under different load and oxygen enrichment conditions in an efficient manner. Simulation results of this 500 MW_e power plant indicate that it is possible to retrofit it to oxy-firing without affecting its overall performance. Further, the feasible range of oxygen enrichment for different power loads is identified to be between 25% and 27%. However, the peak temperature on the superheater platen 2 may increase in the oxy-coal mode at a high power load beyond 450 MW_e.

Table of content

List of Tables

List of Figures

Nomenclature

Abbreviations

ASU	air separation unit
CAD	computer-aided design
CBK	carbon burnout kinetics
CCS	carbon capture and storage
CFD	computational fluid dynamics
Cov	covariance
CPD	chemical percolation devolatilisation
CPU	CO_2 compression and purification unit
CPU	central processing unit
CTF	combustion test facility
DNS	direct numerical simulation
DOE	design of experiments
DOM	discrete ordinates method
DTM	discrete transfer method
EDM	eddy dissipation concept model
Eq	equation
EDCM	eddy dissipation concept model
ESP	electrostatic precipitator
FG-DVC	functional group-depolymerisation vaporization cross-linking
FGC	flue gas condensation
FGD	flue gas desulphurisation
FGR	flue gas recycle
FRH	final reheater

FSCK	full spectrum correlated-k
HPC	high pressure column
IGCC	integrated gasification combined cycle
LBL	line-by-line
LES	large eddy simulation
LPC	low pressure column
MEA	monoethanolamine
MHT	main heat exchanger
Mtoe	million tonnes of oil equivalent
PACT	pilot-scale advanced capture technology
PDF	probability density function
Plat1	superheater platen 1
Plat2	superheater platen 2
PRH	primary reheater
PSA	pressure swing adsorption
RANS	reynolds-averaged navier-stokes
PCA	principal component analysis
ROM	reduced order model
RSM	reynolds stress model
RTE	radiation transfer equation
SCR	selective catalytic reduction
SGS	sub-grid-scale
SNB	statistical narrow band
SSH	secondary superheater
SST	shear stress transport
UDF	user defined function
UKCCSRC	United Kingdom carbon capture and storage research centre

WSGG	weighted sum of gray gas

Latin alphabet

A	effective heat transfer area	m^2
a_λ	absorption coefficient	$1/m$
b	dimensional scaling coefficients	-
C_p	heat capacity	J/kg
F	mass flow rate of the feed stream	kg/s
f	number of degrees of freedom of the gas molecules	-
$\mathbf{f}$	kernel function vector	-
$\mathbf{F}$	response vector	-
g	gravity constant	N/kg
h	mass specific enthalpy	J/kg
I_λ	radiation intensity	W/m^2
k	turbulent kinetic energy in Section 2.2.2	m^2/s^2
k	chemical reaction rate in Section 2.3.1	mol/s
K_{XR}	an empirical constant describing the pressure drop	-
L	mass flow rate of the liquid	kg/s
m	mass fraction	-
M	mass holdup	kg
n	refractive index	-
p	pressure	Pa
Q	heat, energy	J
$\dot{Q}$	total heat flow	J/s
$\vec{\mathrm{r}}$	position vector	m

r	CO_2 absorption rate	mol/s
$\mathbf{R}$	the correlation matrix	-
$\vec{s}$	direction vector	-
t	time	s
T	temperature	K
u	velocity of the fluid in Chapter 2	m/s
u	mass specific internal energy in Chapter 5	J/kg
V	mass flow rate of the vapour in Section 5.2.2.1	kg/s
V	volume flow rate in Section 5.2.2.2	m^3/s
V	volume in Sections 5.2.2.3, 5.2.2.4, 5.2.2.4 and 6.2.2	m^3
W	adiabatic power	J/s
x	mole fraction in Section 5.2.2.2	-
y	height of the riser	m

Greek alphabet

β	geometry coefficient of the furnace	-
$\boldsymbol{\beta}$	regression coefficient vector	-
δ	Kronecker delta	
θ	correlation parameter	-
λ	wavelength in Chapter 2	m
λ	index of the components in Chapter 5	-
ε	rate of dissipation of turbulent kinetic energy	m^2/s^2
γ	adiabatic index of the gas	-
σ	Stefan-Boltzmann constant, 5.669X10^{-8} W/m^2K^4 in Section 2.2.1	

σ	square root of the process variance in Section 6.3.1	-
Ω'	solid angle	-
Φ	scattering phase function	-
ϕ	fugacity coefficient	Pa
μ	dynamic viscosity	$kg/m \cdot s$
ρ	density	kg/m^3
ω	specific dissipation rate $= \varepsilon/k$ in Chapter 2	$1/s$
ω	mass fraction in Chapter 6	
κ	mixed convection/radiation coefficient	-

Subscripts

ad	adiabatic flame
av	average
$circ$	circulation
d	steam drum
eff	effective
$evap$	evaporative
gen	electricity generator
dc	downcomer
in	inlet
liq	liquid
mix	mixture
out	outlet
ox	oxygen
R	riser
ref	reference

s	steam
sat	saturation
tfr	heat transfer
vap	vapour
WDC	water in the downcomer
w	wall of the heat exchanger
XR	water/steam mixture

Chapter 1. Introduction and Motivation

In this chapter, the motivation for this investigation is introduced. The challenge of global warming and the necessity of using coal in the world energy mix are discussed in Section 1.1 and the use of coal and its impacts on the environment are analysed in Section 1.2. The solution for the continuous use of coal while achieving a low carbon emission, namely, the carbon capture and sequestration (CCS) technologies, are introduced in Section 1.3. A brief introduction on power generation system modelling techniques is presented in Section 1.4. Finally, the aims, novelties and the scope of this thesis are outlined in Section 1.5.

1.1 Energy consumption and the role of coal

Investment shows that the world energy consumption will drastically increase from 8,769 million tonnes of oil equivalent (Mtoe) in 1992 to 16,534 Mtoe in 2030 [1]. Further, there has been a worldwide upward in the demand of energy, with Brazil, Russia, India and China being the most likely biggest four economies in terms of energy consumption and demand over the next 2 decades, whose consumption levels of primary energy are even predicted as surpassing the OECD by 2030 [1]. Population growth has always been, and will remain, one of the key drivers of energy demand, along with economic and social development. The world population is expected to reach 8.1 billion in 2025 and 9.6 billion in 2050 [2], which leads to a more extensive demand on energy. Therefore, in order to maintain and improve people's living standards, an increase in energy production is required.

Various types of fuels are used in the power producing industries to generate electricity: fossil fuels (coal, oil and natural gas), hydro, nuclear and renewables and Figure 1.1 describes the increasing trend of the demand on different fuels from 1988 to 2013. Figure 1.1 also reveals that the fossil fuels are the most depended energy sources and a more significant increase in the amount of consumption of coal is witnessed for the past two decades. Meanwhile, the use of coal always takes a remarkable role, which approximately occupies 30% of the total amount, in the whole mix.

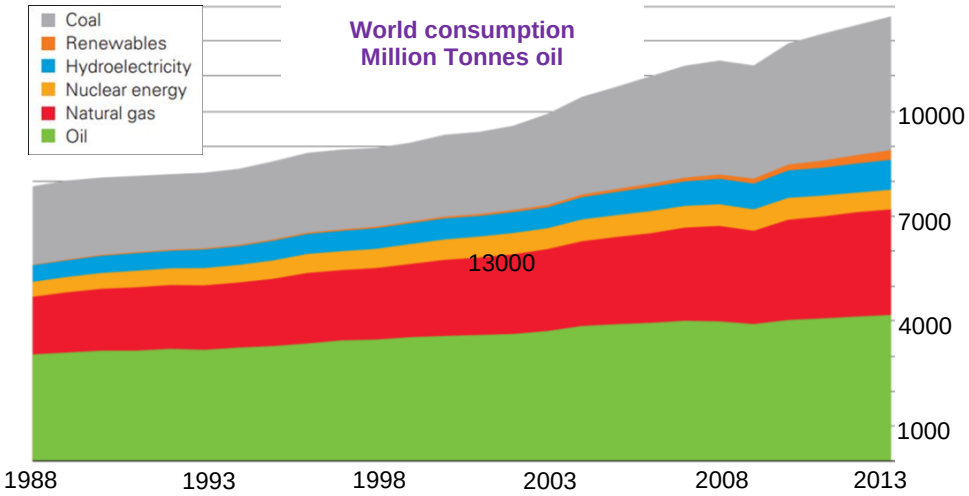

Figure 1.1 World energy consumption by fuel [3].

Due to environmental policies, prices and technology developments, the demand on different fuels is always changing and Figure 1.2 shows the fuel use in the electricity supply in the UK from 1998 to 2013. It can be seen that the coal and gas contributions to electricity are significantly higher than those of other fuels. Moreover, since 2008, the use of gas has dropped gradually while the demand on coal has become relatively stable and even shown a mild rise.

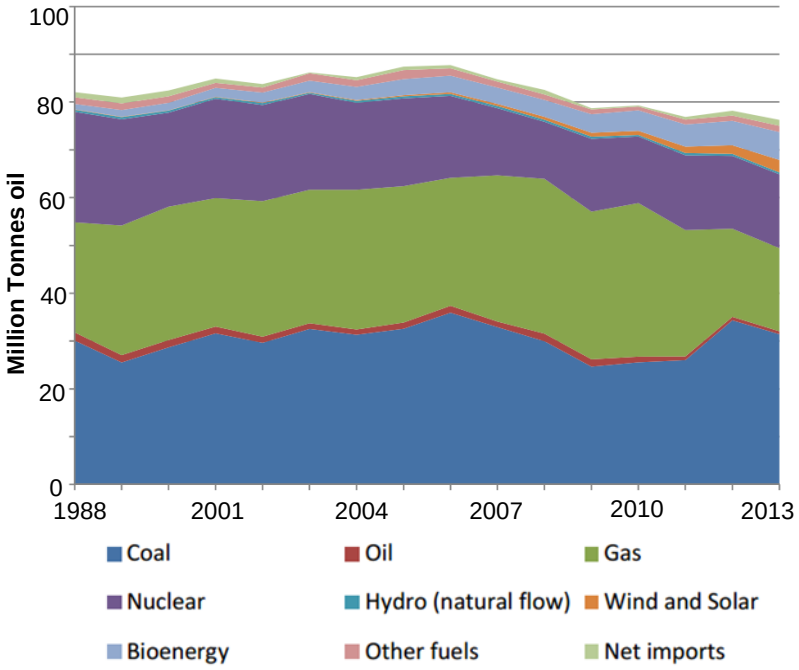

Figure 1.2 Fuel used in electricity generation in the UK over the last 15 years [1].

Currently, fossil fuels are the most widely used sources for the electricity production. Considering the safety, economy, and abundance of the fossil fuels, coal comes first in accommodating human society's demand. The reason is that the security, stability and capacity of supply are important actual issues that need to be considered:

(i) Although the Middle East countries have large amounts of oil reserve, the severe political and security environment of this region may become a barrier for the stable and continuous oil output; on the other hand, for some major developing countries (e.g. China and India) which are short of oil and gas but have considerably large amounts of coal reserve on which they can depend on and even export.

(ii) The clean energies, such as wind, solar and hydro, are environmental friendly and renewable. However, their capacities are too limited to meet all the demands and the stability of supply cannot be guaranteed since the weather and atmospheric conditions which they depend on always change.

(iii) Nuclear power is an attractive alternative since it is considered the only kind of energy that has the potential to replace the fossil fuels for its high electricity producing capability. In addition, nuclear power is clean and does not bring in any unwanted gas emissions, such as CO_2, SO_X or NO_X. However, the disastrous nuclear accidents (Chernobyl 1986 [2] and Fukushima, Daiichi's 2011 [4] nuclear disasters) have warned people about the safety issues of the nuclear power. Following the Fukushima nuclear disaster, many countries have reshaped their nuclear development policies [5], e.g. Germany has decided to close all of its nuclear power stations by 2022 [5]. Fierce debates on nuclear power took place in Italy soon after the Fukushima nuclear disaster and its further nuclear development had been pending so far [5].

(iv) Biomass provides a new option for the energy mix. Biomass energy is mainly produced from plants, animals or other organic sources. It enjoys superiority in terms of sustainability due to the fact that burnt organic sources can release back CO_2 and H_2O into the air and a reproduction of plants and animals could be used to guarantee the circulation of energy generation. More importantly, the NO_X or SO_X emissions by burning biomass

are significantly lower than those of fossil fuels. However, depending on the biomasses can be expensive and its reproduction requires lots of land which may conflict with other demands for the use of land.

To summarise, in the foreseeable future, the demand on energy use will continuously increase and coal will still play a crucial role in meeting this demand.

1.2 Coal combustion and its impacts on the environment

1.2.1 Coal combustion in conventional power stations

The most important usage of coal is in electricity generation. The process of coal consumption in the traditional power plant can be seen in Figure 1.3.

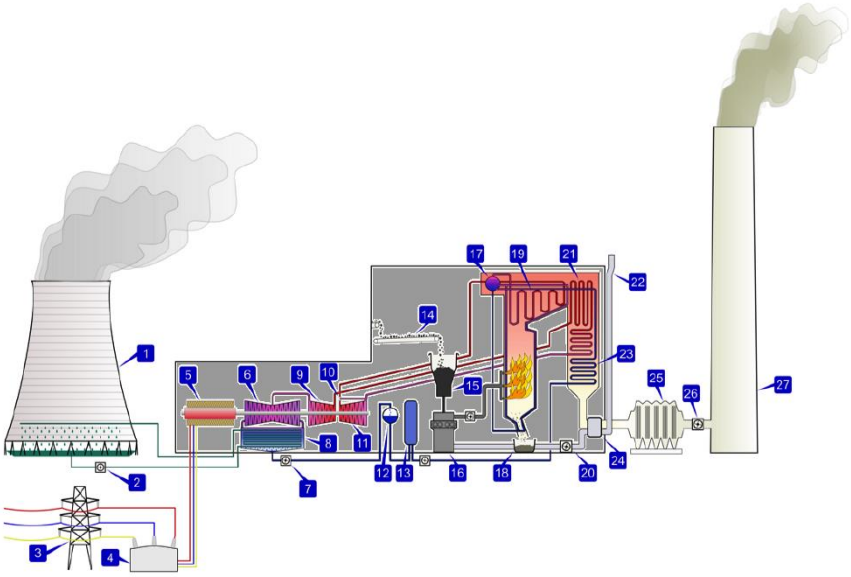

1. Cooling tower
2. Cooling water pump
3. Pylon
4. Unit transformer
5. Generator
6. Low pressure turbine
7. Boiler feed pump
8. Condenser
9. Intermediate pressure turbine
10. Steam governor
11. High pressure turbine
12. Deaerator
13. Feed heater
14. Coal conveyor
15. Coal hopper
16. Pulverise fuel mill
17. Boiler drum
18. Ash hopper
19. Superheater
20. Forced draught fan
21. Reheater
22. Air intake
23. Economiser
24. Air preheater
25. Precipitator
26. Included draught fan
27. Chimney stack

Figure 1.3 Schematic of a coal fired sub-critical power plant.

In the furnace, the process water is converted to high pressure steam by the heat released from the coal combustion. The hot steam then goes through a set of steam turbines where the internal energy of the steam is turned into the mechanical energy of the turbines which drives the generator to produce electricity.

The heat transfer from the coal combustion to the heat exchangers is critical in the steam cycle. These heat exchangers, including the water walls, superheaters, reheaters and economisers, consist of several tube banks in order to enhance the effective area for heat transfer. The steam drum, which is located at the top of the boiler, is also an important component. Before entering the steam drum, the feed water passes through the economiser, which is a convective heat exchanger near the outlet of the furnace. Then the water in the steam drum goes down and into the tubes of the water wall, which surrounds the boiler. As the water passes through the water wall, the water is heated and becomes partially vaporised. This results in a decrease in the density of the water/steam along the water wall, thus the water/steam recirculates back into the steam drum. In the steam drum, the steam is separated from the water/steam mixture and is then passed to the superheaters to be further heated before entering the high pressure turbine. After driving the high pressure turbine, the steam recirculates back to the boiler to be reheated in the reheater, which is next to the superheaters. Then the reheated steam sequentially goes through the intermediate pressure turbine and low pressure turbine. The mechanical energy of the steam turbines is converted into electricity by a downstream generator. At the outlet of the low pressure turbine, the steam is condensed by the cooling water and then goes back to the economiser where another steam circle repeats.

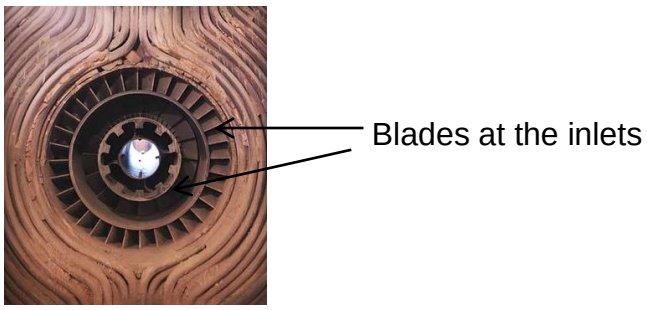

Figure 1.4 Coal burner in a furnace in a power station [6].

As a dominant fuel used by the conventional power plants, coal is firstly ground in the mills to be very fine particles in order to enhance the combustion efficiency and then the pulverised coal is blown into the furnace with the carrying air via the burners. These burners are typically designed in order to reduce the pollutant formation and improve the combustion efficiency by bringing in strong turbulence/mixing between the coal particles

and the oxidant gas, which is achieved by adding swirled blades at the inlets of the burner (see Figure 1.4).

The furnace is the place where the coal combustion takes place and the chemical energy stored in the coal is converted into thermal energy which is transferred to the water wall and the superheaters mainly by radiation. As the high temperature flue gas passes through the superheaters, the gas temperature continues to decrease. When the flue gas reaches the economiser, the convection becomes the dominant form of heat transfer. Further, the flue gas contains some harmful acid gas, e.g. NO_x and SO_x, and therefore additional treatments for the acid gas removal are required before the flue gas is emitted into the atmosphere. Typical devices for the flue gas treatments are: electrostatic precipitator (ESP) to remove the particulate matter (soot or fly ash), the flue gas desulphurisation (FGD) equipment to remove the SO_x and the selective catalytic reduction (SCR) unit to remove the NO_x.

1.2.2 Impacts on the environment

The increase in the concentrations of the greenhouse gases is believed to be the reason for global warming and CO_2 is recognised as the most important greenhouse gas. Global warming is an environmental phenomenon and the world's average temperature has been continuously increasing since the industry revolution. The correlation between the CO_2 emissions and the increase in temperature is simple: too much CO_2 in the atmosphere obstructs the thermal radiation from the surface of the Earth to the outer space – like a thick quilt. Figure 1.5 shows a record of CO_2 emissions since 1900 and it is clear that due to human activities, the global CO_2 emissions have increased by more than 1000% since 1900. Consequently, the average atmospheric CO_2 concentration level has increased by over 30% from about 296 ppm in 1900 to about 390 ppm in 2010 (see Figure 1.6).

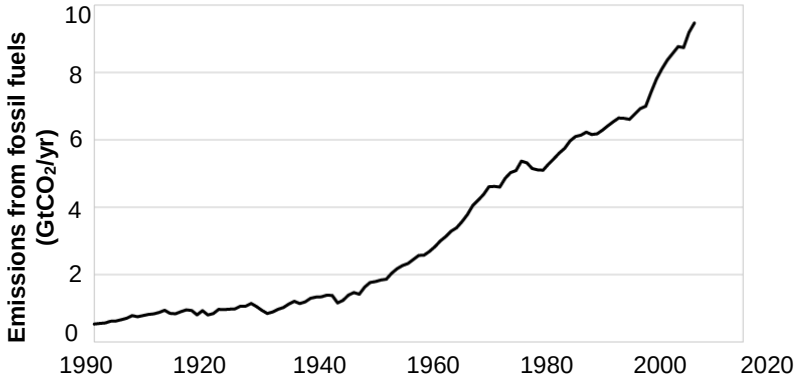

Figure 1.5 Global CO2 emissions since 1900 [7].

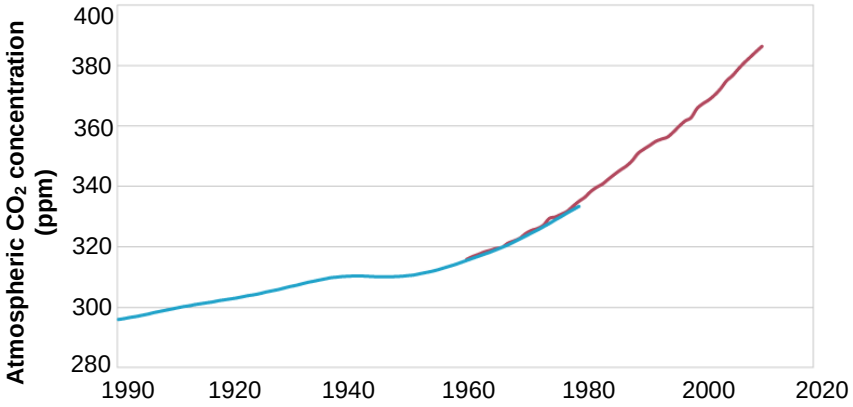

Note: Concentration from two sources: measurements up to 1978 from Antarctic ice cores (blue), and direct atmospheric sampling at Hawaii since around 1960 (red).

Figure 1.6 Average atmospheric CO2 concentration since 1900 [7].

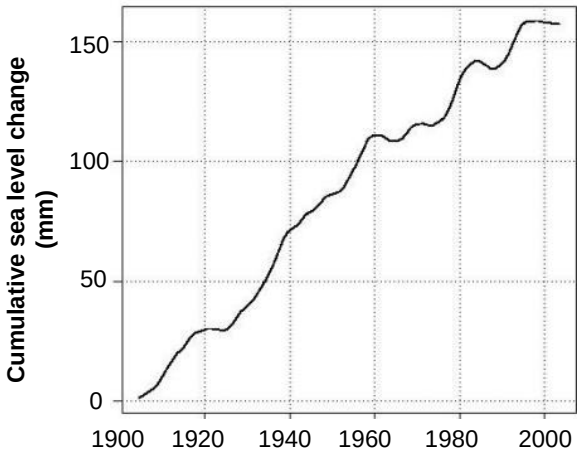

Figure 1.7 Sea level rise over the last 100 years [8].

One of the most concerned worries triggered by global warming is the melting of the huge glaciers around the world, which directly raises the sea level. It has been recorded that the sea level has risen by more than 150 mm

over the last 100 years (see Figure 1.7). If we allow global warming to continue to develop without any control, then in several centuries that most of the land will be under the sea.

Facing this challenge, national and international efforts have been made to reduce greenhouse gas emissions. The Kyoto Protocol international agreement announced in 1997 that in order to commit countries who are members of the United Nations Framework on Climate Change (UNFCC) to reduce greenhouse gas emissions [9]. In Europe, short term and long term targets have been made regarding to greenhouse gas emission reduction: EU members have committed themselves to reducing greenhouse gas emissions by 20%, while increasing the share of renewables in the energy mix to 20% by 2020 [10]. In 2011, the EU confirmed a long term objective of reducing greenhouse gas emissions by 80-95% by 2050 compared to 1990 [10].

The UK, under the framework of UNFCC and the EU, aims to reduce 34% of the greenhouse gas emissions by 2020 and have a further reduction to 80% by 2050 compared to the 1990 level. Other major countries, such as China, United States, Canada, India and Brazil, have started their own program and policies to reduce greenhouse gas emissions [11].

1.3 Carbon capture technologies

The typical CO_2 emission rate from a conventional coal-fired power plant can be as high as about 906 kg/MWh [12]. Therefore, coal-fired power plants are regarded as one of the most significant boosters to the atmospheric CO_2 level. For example, from the top 50 dirtiest power plants in the USA, only less than 1% of the total number, produced 50% of all the USA's vehicle carbon emissions [13]. Considering the importance of coal (see Section 1.1), coal still occupies a large share of the energy mix and will do so in the foreseeable future. Current environmental situations and government policies push energy extensive industries, especially coal-fired power plants, to develop new low carbon technologies.

Carbon Capture and Storage (CCS) represents a set of technologies that can capture more than 90% of the CO_2 produced from burning fossil fuels in

electricity generation and other industrial processes, thus preventing the CO_2 from being emitted to the atmosphere. The captured CO_2 is liquefied and then transported by either pipe lines or ships to a suitable underground storage site which can be saline aquifers or depleted oilfields. Moreover, the stored CO_2 can be utilised in other industrial sectors where pure CO_2 is required. It has been acknowledged that the utilisation of CCS is a necessary way that people can keep fossil fuels in the world's electricity supply mix while still meeting the greenhouse gas reduction requirements [14].

Generally, CCS technologies can be classified into three categories using different technique procedures, and these are pre-combustion, post-combustion and oxy-fuel combustion and the following part of this section provides a brief introduction to these three types of CCS technologies.

1.3.1 Pre-combustion

Figure 1.8 shows a simplified process diagram of the pre-combustion process. In pre-combustion technique, the CO_2 is captured before the combustion process [15]. In the beginning, an air separation unit is used to produce pure O_2, which is then mixed with a suitable amount of coal/fuel in a gasifier where a synthesis gas mainly consists of CO and H_2 [15]. Further, the synthesis gas is passed to a reactor where the shift reaction with water takes place so that a mixture of CO_2 and H_2 is produced. Then, the CO_2 can be captured, compressed and sequestered while the H_2 can then be combusted in a gas turbine or a burner to generate thermal energy and more importantly the flue gas (mainly H_2O) from combustion is 100% clean.

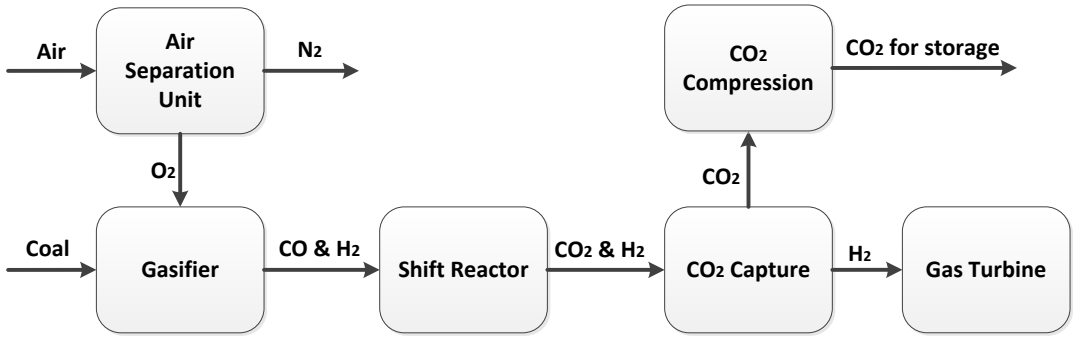

Figure 1.8 A simplified diagram for the pre-combustion process [16].

In the electricity generation sector, the pre-combustion technology can be used with carbon capture in an integrated gasification combined cycle (IGCC) power plant. A significant advantage of the IGCC power plant with carbon

capture is that its efficiency is about 7 - 9% higher compared to those of the oxy-fuel or post-combustion power plants [17]. However, the construction of IGCC power plants requires a high capital investment and this technology cannot be applied to the existing coal-fired power plants. Currently, pre-combustion technology is not yet fully commercialized. In the UK, several IGCC power plant projects are under consideration/construction, namely the Teesside Low Carbon Project (450 MW) with a CO_2 capture ratio of 85%, the C.GEN North Killingholme Project (450 MW) in Yorkshire and the Don Valley Power Project (650 MW) in Yorkshire [18]. However, up to now, these projects have not been commissioned.

1.3.2 Post-combustion

Figure 1.9 represents a simplified process diagram of the post-combustion process where the CO_2 capture process takes place after the combustion in the furnace [19]. The capture of CO_2 could be achieved by allowing the flue gas to pass through some chemical solvent, which can be monoethanolamine (MEA) or methylenedioxyethylamphetamine (MDEA) or mixtures of them [19]. Then the CO_2-rich solvent is heated to release the captured CO_2 which is almost pure and ready for compression, and meanwhile the CO_2-lean solvent is regenerated and recycled to the CO_2 capture loop. In addition, just before the CO_2 capture process, a gas cleaning process, where a flue gas desulphurisation (FGD) unit is employed, it is necessary to remove the SO_2, which has an oxidative degradation effect on the MEA/MDEA solvent [20].

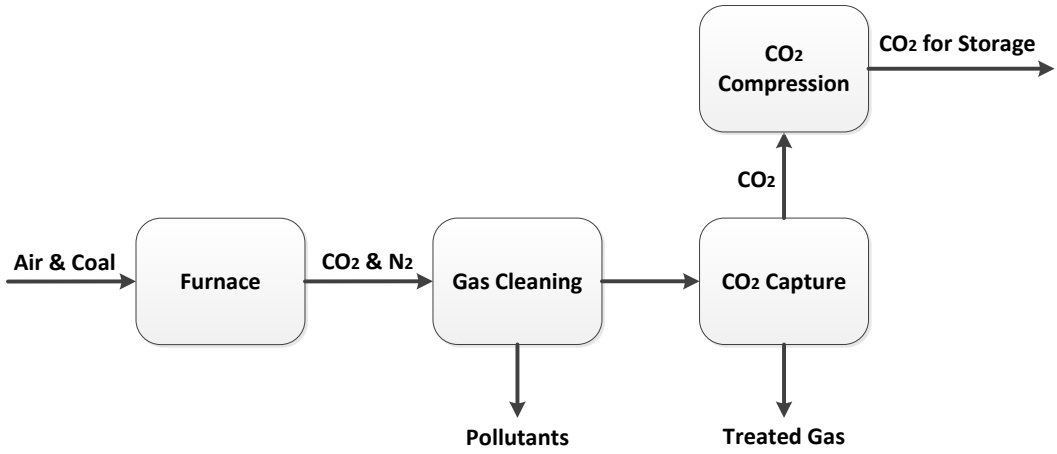

Figure 1.9 A simplified block diagram for the post-combustion process [16].

Post-combustion technology is a promising candidate for carbon capture and storage because it can be directly used to retrofit the existing coal-fired power plants. However, the integration of this technology would result in an efficiency penalty (about 10% of the efficiency penalty with 90% of the CO_2 captured [21]) to the power plant because the regeneration of the lean solvent requires a steam extraction from the steam turbine to provide the necessary heat for the chemical reactions.

The world's first commercial-scale post-combustion CCS project (SaskPower Integrated Carbon Capture and Storage Demonstration Project [22]) has been in operation in Canada. At full capacity, the post-combustion facility captures over 1 million metric tons of CO_2 per year, reflecting a 90% CO_2 capture ratio from a 139 MW coal-fired unit [22]. In July 2014, the world's largest commercial post-combustion project (Petra Nova Project [23]) was announced in the USA. This project aims to install the post-combustion technology to the coal-fired W.A. Parish Generating Station to annually capture 1.4 million metric tons of CO_2 from a 240 MW coal-fired facility, with a 90% CO_2 capture ratio [23]. In the UK, a commercial post-combustion project, based on the Peterhead gas-fired power station in Aberdeenshire is under consideration [24] and the planning application is expected to be submitted in 2015.

1.3.3 Oxy-fuel combustion

Oxy-fuel combustion technology offers a viable low carbon pathway for the existing coal-fired power plants to enable CO_2 capture and storage. The conventional coal-fired furnaces use air as the oxidant in the combustion process where the CO_2 concentration in the flue gas is diluted by the nitrogen. In contrast, as is shown in Figure 1.10, the oxy-coal combustion in a furnace takes a mixture of oxygen and recycled flue gas as the oxidant gas in order to significantly increase the concentration of CO_2 in the flue gases [25]. Generally, the purity (vol%) of the O_2 used in the oxy-coal combustion is not less than 95% and for this purpose an ASU is employed [25]. The recycled flue gas is for the purpose of the flame temperature control and makes up the volume of the separated N_2 to ensure there is sufficient gas to transfer the combusted heat to the heat exchangers. After the oxy-coal combustion, a flue gas, mainly consisting of H_2O and CO_2, is produced,

which is ready for compression and storage after a gas cleaning process where the SO_x is removed [25].

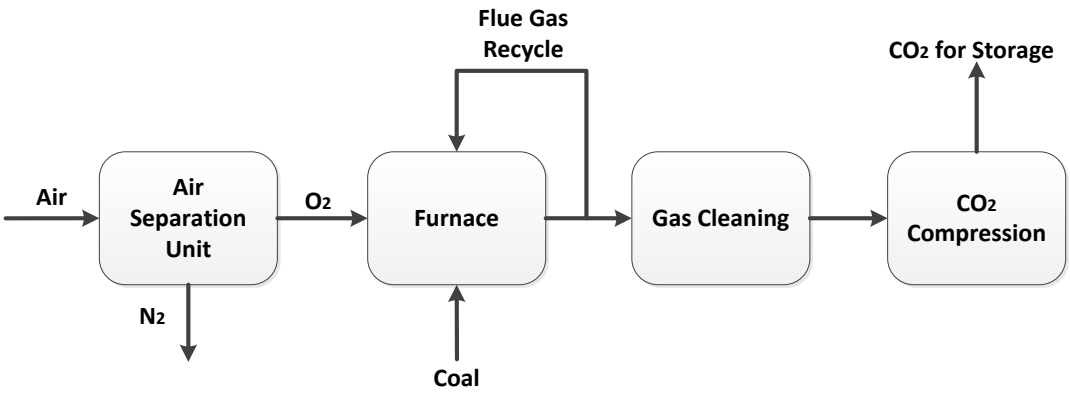

Figure 1.10 A simplified block diagram for the oxy-fuel combustion process [16].

It should be noted that the use of an ASU in this technology brings in an energy penalty of about 10% [26] to the power generation system. The preferred method for the ASU is cryogenic distillation, since this technology currently is commercialised and is capable of producing a large amount of high purity oxygen compared to other oxygen separation technologies [27].

At the moment, oxy-fuel technology has not been commercialised and the Callide Oxy-fuel Project [28] is the only demonstration project of a oxy-fuel power plant in the world. The air-coal Callide-A power station in Queensland having a full load of 30 MW is retrofitted to an oxy-coal power plant.

In the UK, a oxy-fuel demonstration project with a gross output of 448 MW, named the White Rose CCS project [29], has been announced and the oxy-fuel power plant will be situated near to the Drax Power Station.

1.4 Power generation system modelling

System computer modelling techniques enable engineers to research and evaluate the power plant operation, optimisation and control policies so that the potential risk and cost of operating/constructing the power plant can be reduced.

In the modelling of a coal-fired power plant, accurate modelling of the boiler is important because even a small change in the combustion environment of the boiler may pose a significant impact on the overall performance of the

plant. In the boiler, the complex coal combustion process takes place and energy is released from the coal. The combustion process involves several steps: (i) the coal particle is preliminarily heated when entering the boiler; (ii) the moisture content in the coal is evaporated; (iii) as the coal particle absorbs more heat, the devolatilisation process takes place so that the volatile matters and tar is released; (iv) the char content left in the particle combusts as it is further heated. Correspondingly, in order to accurately model the combustion process in the boiler, the devolatilisation, volatile combustion and char combustion processes must be properly modelled. In addition, the strong turbulence in the boiler as the turbulence has an effect on the combustion process. Fortunately, computational fluid dynamics (CFD) is an important modelling technology in researching the combustion and fluid flow characteristics in the boiler and typically a commercial CFD code, named ANSYS FLUENT, can be used to cover these problems. ANSYS FLUENT employs the finite volume method to discretize the fluid domain enclosed by the boiler into a huge number of cells based on which the transport equations for the mass, momentum and energy balances are solved. The continuum gas phase is solved in an Eulerian frame [30] while the motion of the discrete coal particles is predicted in the form of a Larganian frame [30].

Apart from the boiler, a coal-fired power generation system contains many other components, such as the steam drum, steam turbines and the condenser. In addition, the air separation unit and the amine capture plant are involved in the whole system if carbon capture technologies are applied. It is impossible to wholly depend on CFD techniques to model all of these components due to the expensive computational resources and time required. Fortunately, process simulation techniques can cover this gap and there are several commercial process simulators available for this purpose, such as ASPEN Plus, gPROMS, PRO/II, DYNSIM, etc. Generally, process simulation employs simple mass and energy balance equations (zero or one-dimensional) to describe the modelled unit and numerous empirical parameters are employed. Therefore, the computational effort required is quite small compared to that employed in the CFD modelling.

In order to take advantages of both the CFD and process modelling techniques, integrated CFD and process co-simulation methods are becoming state-of-the-art in the research on the performance and integration of the power plant. It is clear that a 3D boiler CFD simulation usually takes a long time to obtain converged results while the process simulation accounts for the other components is much faster. Then if CFD and process modelling techniques are directly linked in such a way that the CFD simulation has to be performed at each of the operational conditions that are required in the plant process model. This approach is straightforward but requires an unacceptable amount of time for the CFD calculations to cover a whole range of operational conditions of a power plant [31]. Therefore, the efficient integration of CFD and process simulation techniques needs to be considered. Hence the reduced order model (ROM) technology provides a possible solution which is able to take the place of CFD models to very quickly obtain the necessary information (such as the heat flux to the water wall) to drive the process simulation [31].

1.5 Research aims, novelties and scope of the thesis

1.5.1 Research aims and novelties

Carbon Capture has been recognised as playing an important role in reducing the CO_2 emissions from coal-fired power plants so that coal can be continued to be used in the energy mix. Both CFD modelling and process modelling techniques have been confirmed as important methods for investigating the application of the Carbon Capture technologies in the coal-fired power plants. Therefore, this research aims to develop a CFD and process co-simulation technique that can be depended upon to efficiently evaluate the operations of the power plants using carbon capture techniques.

The novelties of this research are as follows:

i) More accurate reduced order models (ROM) have been developed to link the CFD to the whole plant process model.

ii) A new approach has been suggested for estimating the potential of retrofitting an existing power plant to oxy-firing.

iii) A feasible range of oxygen enrichments for the retrofitted power plant has been identified at different power loads.

1.5.1 Scope of the thesis

Concerning the technical issues discussed in Section 1.4, the research to be performed in this thesis can be divided into several milestones:

(i) In Chapter 2, a detailed literature review on oxy-coal system modelling techniques is presented, which involves CFD modelling and process simulation techniques. In the following Chapter 3, the experimental facility and data that are required for the model set up and validation in the thesis are summarised.

(ii) In Chapter 4, a set of combined CFD and process simulations is performed on an experimental facility, which involves a 250 kW_{th} coal combustion furnace and a MEA based CO_2 capture plant. The CFD techniques are employed to solve the turbulence, chemical reactions, and heat transfer in the coal combustion furnace while the process modelling techniques are used to account for the modelling of the CO_2 capture plant. Then the reduced order models based on the CFD simulation results of the furnace are linked to the process model for CO_2 capture plant.

(iii) In Chapter 5, the research objective is extended to the modelling of a large-scale coal firing power plant. A three dimensional CFD model for the utility boiler of this power plant and a process model for the whole power plant are developed. These efforts are the necessary preparations for developing a CFD and process co-simulation approach that can be employed to predict the operations of a power plant under both air-coal and oxy-coal firing conditions.

(iv) Based on the CFD and process models developed in Chapter 5, a new approach has been developed in Chapter 6 in order to estimating the potential of retrofitting an existing power plant to oxy-firing. The three dimensional CFD boiler model developed in Chapter 5 has been employed to simulate the complex coal combustion and heat transfer to the boiler heat exchangers under air-firing and oxy-firing conditions. Then, a set of reduced order models has been developed to link the CFD predictions to the whole plant process model, developed in Chapter 5, in order to simulate the

performance of the power plant under different load and oxygen enrichment conditions if retrofitted to oxy-firing. The reduced order models are generated based on the CFD simulations of the boiler using a non-linear Kriging interpolation method. With this new CFD-process co-simulation approach, the potential of retrofitting the Didcot-A power plant to oxy-coal firing is analysed.

Chapter 2. Literature Review

This chapter provides a detailed literature review on the modelling technologies with regard to the CO_2 capture technologies that can be applied to the existing or new built coal firing power plants. The combustion process of the coal particles and modelling techniques are discussed in Section 2.1. The considerations of heat transfer and turbulence in CFD modelling are reviewed in Section 2.2. The process modelling approaches for the CO2 capture techniques that can be used in coal-fired power plants are discussed in Section 2.3. Finally, a brief summary about this chapter is provided in Section 2.4.

2.1 Coal combustion process modelling

Appropriate description and modelling of the combustion process of a single coal particle is important as it is fundamental for the modelling of the coal combustion in large scale boilers. The combustion process of a coal particle undergoes four major stages as described in Figure 2.1. In the evaporation process, the moisture content in the coal particle is evaporated; as the coal particle is further heated, the devolatilisation process takes place, where the volatile contents (light gases and tars) start to be released and react with the oxygen, which is known as volatile combustion. Then, as the temperature of the coal particle further increases, the char combustion process occurs, where the remaining char is oxidised at a lower rate compared to the devolatilisation and volatile combustion.

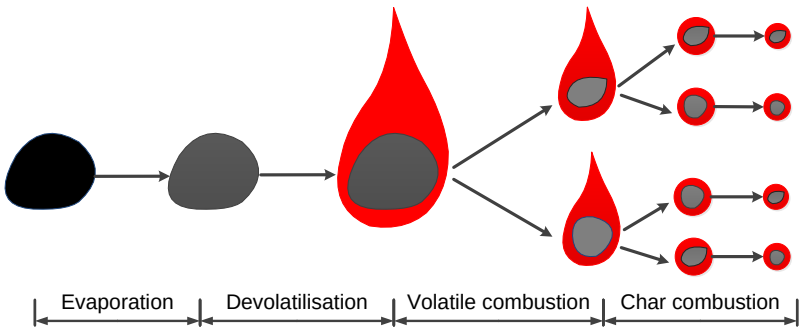

Figure 2.1 Schematic of the combustion process of a coal particle [32].

It should be noted that the above description on the combustion process of a coal particle assumes that each stage takes place in a sequential order and this assumption is adopted in the current CFD codes. However, in fact, some of the stages may overlap.

2.1.1 Evaporation and devolatilisation

As the coal particle is heated by the surrounding gas quickly, the water evaporates fiercely once the temperature reaches the boiling point and the water escapes from the surface of the particle through many pores in the particle. During the evaporation process, the particle may shrink or break into smaller pieces, but this effect is currently not considered in the modelling techniques.

When the temperature increases further to about 600 K [33, 34], the light gases and tars, namely the volatile contents, begin to leave the particle through pores to the external gas phase and their subsequent oxidisation generates mainly CO_2 and H_2O. The physical structure of the coal particle changes significantly, which is related to the release of the volatile matter, and a swelling phenomenon can be observed [35]. The devolatilisation process is fundamentally affected by the coal type, temperature, pressure and the species of the surrounding gas [34]. After the devolatilisation process, the solid material remaining in the particle is the char, which has a porous structure. In fact, the structure and reactivity of the char is affected by the devolatilisation process [32, 36].

Clearly, the amount of volatile content released from devolatilisation varies for different coal types. Coal can be classified into three main categories, namely the lignite, bituminous and anthracite, according to their ages [32]. As the youngest coal, lignite is comparatively soft and mainly contains moisture and volatile matters with low fixed carbon, while the anthracite, as the oldest coal, is comparatively hard and mainly contains fixed carbon with little moisture and volatile matter [32]. The amount of volatile matter present in the bituminous coal lies between the other two types of coal [32]. In addition, it had been found that the amount of volatile matter released could be enhanced by a higher peak temperature and higher heating rates [37-39]. The amount of the volatile matter in the coal can be measured from a drop-

tube furnace with controls on the heating rate. A factor called the ‘high temperature volatiles yield ratio’ is usually employed to describe this enhancement by comparing the amount of the obtained volatiles to that measured from a standard proximate analysis [37].

The rate of devolatilisation can be modelled by a single-rate model [39] using a single Arrhenius formation where the devolatilisation rate is assumed to be proportional to the volatiles remaining in the particle. As a matter of fact, the volatile mater leaves the particle at various rates, thus the single-rate model may be insufficient to accurately describe the process. A more suitable solution with higher fidelity would be the two-competing rate model, which was developed by Kobayashi et al. [40]. The two-competing rate model relies on six parameters and is capable of modelling most coals, if the corresponding data for the coal is available. Silaen et al. [41] investigated different devolatilisation models as a part of a CFD code. They found that the two-competing rate model predicted a slower devolatilization rate than the single-rate model but produced a higher exit gas temperature and higher CO_2 mass fractions. However, experiments were not performed. The Sandia National Laboratories [42] performed a number of experiments and found that the model constants used by Kobayashi et al. [40] could not give satisfying predictions on some coals, while the constants used by Ubhayakar et al. [43] appeared to increase the accuracy.

Network models, such as the chemical percolation devolatilisation (CPD) model [44], the functional group-depolymerisation vaporization cross-linking (FG-DVC) model [45] and FLASHCHAIN [46], can predict the devolatilisation rate and the yields of gases and tars under different heating rates if the structure parameters of the coal particle are available. Jones et al. [47] evaluated different devolatilisation models and concluded that the network models could provide satisfactory devolatilisation rates. William et al. [48] performed experiments on a drop-tube furnace for a range of coals and the experimental results were compared to the predictions from the CPD, FG-DVC and FLASHCHAIN models and the predictions on the volatile yields were in generally good agreement with the experimental data, although these models predicted slightly different results.

Rastko et al. [49] implemented the single rate, two competing rates, CPD and FG-DVC model as a part of a CFD code in order to numerically determine the ignition point of a bituminous coal in a laboratory ignition test facility under air and oxygen enriched environments. The predictions suggested that the network models (CPD and FG-DVC) provide more accurate results compared to the single rate and the two competing rates models and the best performance was achieved by the FG-DVC model. However, the authors indicated that the use of the FG-DVC model would require much more computational resources, since the additional transport equations for the volatile species need to be solved. The results also revealed that the devolatilisation models, which were originally developed for conventional air combustion, can be applied to oxygen enriched combustion conditions. Moreover, Shaddix et al. [50] found that the switching to an oxygen enriched combustion environment has little impact on the devolatilisation process if the combustion temperatures are kept the same.

2.1.2 Volatile combustion

The volatile matters are released from coal particles mainly contain CO, CO_2, H_2O and many hydrocarbons [36]. The volatiles then react with the surrounding oxidiser gas to produce CO_2 and H_2O with numerous intermediate products. Therefore, the accurate description of the volatile combustion process involves a large number of intermediate reactions and species [32], which would pose a significant challenge for the CFD modelling as numerous chemical mechanisms and transport equations need to be solved. A popular solution and simplification is a global mechanism, which assumes the reaction rates to be very fast and greatly reduces the number of reactions and species. The global mechanism assumes the volatile matters to be a single material $C_xH_yO_z$ and its oxidisation can be represented as the following two step reaction [51]:

$$C_xH_yO_z + \alpha O_2 \rightarrow xCO + \frac{y}{2}H_2O, \quad \text{where } \alpha = \frac{2x+y-2z}{4} \tag{2.1}$$

$$CO + \frac{1}{2}O_2 \rightarrow CO_2 \tag{2.2}$$

In this global mechanism, an intermediate species ‘CO’ is introduced to describe the char oxidation occurring on the particle surface and the

intermediate CO is further oxidised to CO_2. In fact, the complex combustion process is highly determined by the turbulent mixing, which affects the kinetic rates of the reactions.

For the laminar flames, the reactions in the combustion gas phase can be described by the kinetic rates. However, in a pulverized coal combustion furnace, the volatile combustion is significantly coupled with the strong turbulence. It is known that strong turbulence may greatly enhance the reaction rates [52] and this makes the global mechanism theoretically applicable. In fact, the proper selection of an approach to model the volatile combustion involves several aspects that need to be considered: accuracy, the ability to describe the chemical reactions and the computational requirement.

The eddy dissipation model (EDM) [53] relates the reaction rates with the turbulence level. However, this model ignores the chemical kinetics, thus it does not account for the intermediate species and can be only used with the global mechanism. The EDM has been widely used for modelling the pulverized coal combustion process [54-57]. The eddy dissipation concept model (EDCM) [58], as an expansion of the EDM, takes the detailed chemical kinetics into consideration and therefore this model can describe the intermediate reactions and products. However, this requires the solution of the transport equations for each species, and thus the demand on the computational resources is significantly higher.

The laminar flamelet model [59] treats the turbulent flame as a set of laminar flamelet regions. This model considers a larger number of chemical reactions and intermediate species. The characteristic of this model is that the density, species fractions and the temperature profile near the flamelet are described by the mixture fraction and the scalar dissipation rate [60]. However, the scalar dissipation rate needs to be modelled separately. Combined with a PDF, the flamelet model can be used to model the turbulent flames.

The application of the probability density functions (PDF) [61] provides a promising option to address the chemical kinetics in the combustion flows. The significance of this approach is that the chemical source term can be

easily expressed. However, this approach is computationally expensive. The mathematic formation of the PDF needs to be assumed, such as the β-PDF. William et al. [48] compared the PDF model to the finite rate model in the CFD calculations and found that the predictions from the PDF model showed a better agreement with the experimental data.

2.1.3 Char combustion

Once the volatile matters have been released from the coal particle, the remaining material is the char content, which mainly includes free carbon and incombustible matters. The combustion process of the char involves a number of issues that need to be considered, such as the temperature, coal type, particle size, surface area, oxygen fraction in the surrounding gas and the resident time in the high temperature flame region [32]. Although a large amount of research has been devoted, both numerically and experimentally, the char combustion mechanism is not yet fully identified due to the complex pore development and mass transfer in the char combustion process [62].

The char combustion is mainly dominated by the reaction between the carbon and the oxygen, which produces CO and further CO_2. The fractions of CO and CO_2 are fundamentally determined by the local temperature. A higher CO fraction is usually found at high temperature locations (such as the particle surface), where the CO_2 fraction is quite low [32]. In addition, the gasification of the carbon by CO_2 and H_2O may occur at high temperatures, therefore the char reactions can be described by the following equations:

$$C + \frac{1}{2}O_2 \rightarrow CO \tag{2.3}$$

$$C + CO_2 \rightarrow 2CO \tag{2.4}$$

$$C + H_2O \rightarrow CO + H_2 \tag{2.5}$$

It should be noted that when the oxygen concentration is comparable to the CO_2 concentration, the gasification reactions become less important [63], especially in the pulverized coal fired boiler of a power plant. Therefore, the gasification reactions were ignored in these CFD investigations [56, 57, 64] on the pulverized coal combustion process in coal fired boilers and this results in a satisfactory agreement with the experimental data being obtained.

The diffusion limited model, which was developed by Baum and Street [33], calculates the reaction rate based on the oxygen diffusion rate to the char surface, but this model ignores the impact of the chemical kinetics. As an improvement, the kinetics-diffusion limited model [33] takes both the oxygen diffusion rate and the chemical kinetics into consideration. Simulation results using the kinetics-diffusion limited model were performed in [65] and the predictions on the temperature showed a good agreement with experimental data. However, it should be noted that these methods do not consider the exact char shape or the particle swelling.

Clearly, the char porosity enhances the reaction area of the char particle, which has a fundamental impact on the char oxidisation. Therefore, in order to account for the effects introduced by this factor, the intrinsic model [66] was proposed, which considers the char porosity and the change in the surface area throughout the combustion process. Specially, this model regards the reaction rate as a combination of the pore surface diffusion and the intrinsic reactivity [67]. The simulation results obtained from the intrinsic model and the kinetics-diffusion limited model were separately compared to the experimental data in [48] and found that the intrinsic model predicted more accurate results.

The carbon burnout kinetics (CBK) model [68] was developed based on the intrinsic model and this model considers more effects, such as thermal annealing, statistical kinetics, statistical densities, and ash inhibition in the late stages of the char combustion [68]. Gharebaghi et al. [69] employed the CBK model to investigate the char combustion kinetics under oxy-coal combustion conditions and modifications have been made on the CBK model in order to make it applicable to oxygen-enriched environments. It was found that the modified CBK model improved the accuracy of the burnout prediction under both air-coal and oxy-coal conditions.

In a CO_2/O_2 environment, Kuhr et al. [70] numerically found that the consideration of the C-CO_2 reaction improved the oxygen predictions compared to the experimental data. This investigation reveals that in the CFD simulations for oxy-coal combustion systems, the consideration of the gasification effects may be important. However, oxygen concentration is

usually higher near the burner region, where the gasification reactions are less important, while the oxygen concentration near the boiler exit is usually much lower (0-5%) and gasification effects become important, but in the exit region, most of the particles have been burnt out.

2.1.4 Pollutant formation

Coals contain small fractions of sulphur and nitrogen and the fractions vary with different coal types. The sulphur and nitrogen content can produce pollutants, such as SO_x and NO_x, during coal combustion. These pollutants are harmful to the environment, thus it is necessary to model the mechanisms for the SO_x and NO_x formation during coal combustion. However, the detailed pollutant formation mechanisms can be safely ignored if the CFD simulation is focused on the overall heat transfer characteristics [56, 57], since the quantities of the pollutant gases are quite small compared to other species. During the coal combustion process, NO_x is mainly generated through three different manners: thermal NO_x, prompt NO_x and fuel NO_x and NO is considered as the most significant form of NO_x, since it accounts for about 90% of the total NO_x produced.

2.1.4.1 NO_x formation

In the thermal NO_x mechanism, NO is formed from the reaction between O_2 and N_2 at high temperatures, which can be described by the Zeldovich mechanism:

$$O + N_2 \rightleftharpoons NO + N \tag{2.6}$$

$$N + O_2 \rightleftharpoons NO + O \tag{2.7}$$

A combination expression of the above two reactions can be written as:

$$O_2 + N_2 \rightleftharpoons 2NO \tag{2.8}$$

where overall reaction rate is highly temperature dependent and its mathematical expression can be found in [32]. Since the overall reaction is slow, equilibrium concentrations of NO are built up only in situations where the residence time is sufficient, i.e. in large boilers. In smaller boilers, the thermal NO formation is limited by the lower residence time.

The prompt NO mechanism was found by Fenimore [71] and it accounts for the formation of NO from reactions involving N_2 and carbon-containing free

radicals, which can be the intermediate species from the volatile combustion. The formation of prompt NO involves a number of reactions which have been summarised in [32]. Prompt NO mainly occurs in fuel-rich flames with short residence times and only accounts for a small part of the total NO.

The fuel NO mechanism is the dominant form of NO production throughout the coal combustion process. The fuel-N contained in the coal is separated into two groups after the devolatilisation process: one group is named volatile-N and the other one is called char-N [72]. The volatile-N is mainly HCN and little NH_3 [32]. Then the volatile-N is oxidised to produce NO or N_2 and their relative amounts depend on the concentration of the fuel-N in the fuel; if rich, all HCN would produce N_2 [32]. The char-N mainly forms NO and more than 75% of N is converted to NO in high temperature regions. The difficulty for modelling the fuel NO is the accurate prediction of the ratios of the char-N and volatile-N and the ratios can be directly obtained by experiments or by the devolatilisation models described in Section 2.1.

Álvarez et al. [73] integrated different network models with CFD techniques to predict the volatile-N and char-N formation from several types of coals under both air-coal and oxy-coal conditions. The HCN to NH_3 ratio from the volatile-N can be directly obtained by the network models; as for the char-N, the HCN to NH_3 ratio was approximated by a conversion coefficient. The network model FG-DVC was found to produce accurate predictions for all the investigated coals. Álvarez et al. [74] also investigated the NO formation using FG-DVC model and found that FG-DVC could give reasonable predictions at different temperatures and heating rates, but also found that the results for the air-coal and oxy-coal conditions showed little difference.

Several approaches are available to reduce the NO production during, such as, the low-NO_x burner, the SCR (selective catalytic reduction) and the reburning technique.

2.1.4.2 SO_x formation

Coal also contains sulphur and the sulphur content can be oxidised to produce SO_2 or SO_3, which are known as acid gases and may corrode the process devices with the presence of moisture. The release of sulphur is similar to the release of fuel-N during devolatilisation, and therefore the

sulphur can be similarly regarded as volatile-S and char-S. It was found that the formation of SO_2 in oxy-coal combustion is significantly higher than that in air-coal conditions [75]. However, the SO_3 formation is lower than that under air-coal conditions.

2.1.4.3 Soot formation

Soot is a mixture of impure carbon particles due to the incomplete combustion of the hydrocarbons. Soot is a pollutant, which is believed to disturb the radiative performance of the combustion gas, and a previous investigation [76] indicated that the neglecting of the soot in the coal combustion modelling would cause large errors in the temperature predictions. However, the soot formation mechanism is not yet fully understood and further modelling and experimental work is required [77].

A widely used model for modelling the soot formation was proposed by Brown et al. [76]. However, this model depends on some empirical parameters, which were obtained from air-coal combustion experiments, thus it could be only applied to air-coal combustion modelling with confidence. It has been found that the soot formation depends upon the stoichiometry in the combustion regions [78], thus this ignored the differences between the air-coal and oxy-coal conditions. However, a further investigation [79] found that the soot formation in the oxy-coal environments is lower than that in air-coal environments.

2.2 Heat transfer and turbulence

Computational fluid dynamics (CFD) techniques provide a viable tool for investigating the coal combustion process, since CFD techniques incorporate the complex geometries of the coal fired boilers and detailed numerical models on heat transfer and turbulence. The finite volume method (FVM) is widely used by most CFD codes to discrete the governing conservation equations over the computational regions characterised by a number of computational cells. The use of non-uniform grids can ease the difficulty in meshing the burners or other complex geometries. The proper meshing of the geometries is important as its quality may affect the accuracy of the solutions, even if the sub-models for the particle combustion, heat

transfer and turbulence are properly set. Therefore, a large number of meshing tutorials can be accessed online.

In fact, in order to accurately perform CFD simulations on the coal combustion process in a coal fired boiler, it does not only include the detailed models accounting for the coal particle oxidisation (Section 0), but also involves proper sub-models incorporating heat transfer and turbulence.

2.2.1 Heat transfer

During the coal combustion process in a boiler, heat is released and then transferred to the water/steam inside the water wall tubes surrounding the furnace and the hanging tube heat exchangers. Heat transfer includes three approaches: convection, conduction and radiation, and radiation is the dominant form of heat transfer in the furnace region. However, in the region far away from the furnace section, the gas temperature has been significantly reduced, thus convection becomes dominant.

Radiation is quite extensive in the furnace, since it is proportional to the fourth power of the temperature. Radiation is governed by the following radiation transfer equation (RTE) [80]:

$$\frac{dI_\lambda(\vec{r},\vec{s})}{ds} = a_\lambda n^2 \frac{\sigma T^4}{\pi} - (a_\lambda + \sigma_{s,\lambda}) I_\lambda(\vec{r},\vec{s}) + \frac{\sigma_{s,\lambda}}{4\pi}\int_0^{4\pi} I_\lambda(\vec{r},\vec{s}')\Phi(\vec{s},\vec{s}')d\Omega' \quad (2.9)$$

where λ is the wavelength, $\vec{r}$ is the position vector, $\vec{s}$ is the direction vector, $\vec{s}'$ is the scattering direction vector, s is the path length, a_λ is the absorption coefficient, n is the refractive index, $\sigma_{s,\lambda}$ is the scattering coefficient, σ is the Stefan-Boltzmann constant ($5.669\times10^{-8} W/m^2K^4$), I_λ is the radiation intensity, T is the local temperature, Φ is the phase function and Ω' is the solid angle.

The radiation intensity I_λ is determined by the wavelength λ, spatial position $\vec{r}$, direction $\vec{s}$ and the solid angle Ω'. In order to accurately predict the radiation, these techniques need to be wisely selected: a proper approach to solve the RTE as well as the model to account for the absorption and scattering properties of the gas and particles.

There are several approaches available to solve the RTE, namely the P-N method [81], the discrete ordinates method (DOM) [82], the discrete transfer method (DTM) [83], and the Monte Carlo method [84]. Both the P-N and the discrete ordinates methods are applicable to the combustion flows since these methods are able to conveniently incorporate the scattering, absorption, and the emission effects of the combustion gas and particles. The discrete transfer method is a ray-tracking approach which directly tracks the paths of rays until the rays reach other surfaces. However, this method neglects the scattering effects brought by the particles, which need to be considered for the coal combustion environments as the interactions between the particle-radiation are extensive. The Monte Carlo method is also a ray-tracking approach and it employs statistical techniques to calculate the radiation intensity that travels through the medium. This method is considered to be accurate as it completely randomizes the directions of the rays, however, the demand on the computational power significantly increases.

In the boiler, the heat is released from the combustion of the coal particles, which have strong interactions to the radiation field as they can either emit or absorb the radiations. A simple solution that accounts for the effects of the particles is to apply a gray assumption, which ignores the impacts introduced by the different wavelengths. In this assumption, the particle-radiation interactions are determined by the particle temperatures, size of the particles and special distributions. A previous study [85] compared the particle-radiation and the gas-radiation interactions under both air-coal and oxy-coal conditions and found that the particle-radiation interactions are much more extensive than the gas-radiation interactions.

In addition, the combustion gas contain some species with strong absorption capacities, such as CO_2 and H_2O, and it should be noted that the CO_2 concentration in the oxy-coal combustion is much higher compared to that in the air-coal combustion. Therefore, the radiative properties of the combustion gas needs to be addressed in the radiation modelling.

A number of approaches can be used to account for the radiative properties of the gas phase and these approaches can be classified as the following

groups: line-by-line (LBL) models, band models and the global models [16]. Although the line-by-line models are considered to be accurate, the huge demand on the computational power by the line-by-line models limit their applications to the CFD investigations [86]. The band models can be classified into narrow band and wide band models according to how they treat the full spectrum. The narrow band models [87] directly split the full spectrum into a set of intervals, while the wide band models [88] only consider the important intervals whose wavelengths are more interacted with the radiation field. Thus the wide band models are more computationally efficient but it should be noted that these band models can be only solved with ray-tracking approaches.

As a widely used global model, the WSGG model [89] employs a set of polynomials, as functions of the temperature, to calculate the absorption coefficients of the gas phase and the most widely used model parameters were proposed by Simth et al. [90]. However, these parameters need to be modified for the oxy-coal simulations as the original values could only be applied in the combustion simulations where the CO_2 concentration is much lower than that in oxy-coal conditions [91]. Therefore, appropriate WSGG parameters for oxy-coal combustion need to be obtained and a straightforward approach is to fit the WSGG polynomials from the predictions by the more fundamental models, such as the statistical narrow band (SNB) model [92] or the line-by-line model [93, 94].

Based on the SNB model, Johansson et al. [91, 92] proposed new WSGG parameters that are applicable in the oxy-coal simulations with different concentration ratios of CO_2/H_2O and found that the new WSGG correlations improved the accuracy of the radiation predictions. Compared to the band models, the computation time was greatly reduced. Further, other new WSGG parameters for oxy-coal combustion were developed by Kangwanpongpan et al. [94]. The new WSGG parameters were fitted from the results obtained by the LBL model and the accuracy of the radiation predictions was improved.

The full-spectrum correlated-k (FSCK) model [86] is also a global model that has been used in oxy-coal simulations. Porter et al. [95] employed the non-

gray FSCK model and the gray WSGG model to calculate the radiative properties under both air-coal and oxy-coal cases. It was found that the non-gray FSCK method provided predictions with better agreement with the benchmark data for all of the cases, while the gray WSGG model tended to give over-predicrions. However, the computation time required by the FSCK model is much higher than the gray WSGG model.

2.2.2 Turbulence

Strong turbulence can be observed in coal-fired boilers and turbulence is an important factor that needs to be properly considered as it affects every aspect of the coal combustion process, including mass transfer, chemical reactions and heat transfer. Turbulent models in CFD can be classified into three groups, namely direct numeric simulation (DNS), large eddy simulation (LES) and the Reynolds-averaged Navier-Stokes (RANS) method, according to their ability to model the details of the turbulence [80].

2.2.2.1 Direct numerical simulation (DNS)

The DNS approach dynamically solves the entire range of turbulent scales, which is quite computationally expensive [80]. Thus this method is currently not suitable to be applied to modelling the coal combustion process in boilers, where strong turbulence and complex chemical reactions take place. It should be noted that DNS is accurate, and therefore it can provide validation data for the LES and RANS when the experimental data is not available [96].

2.2.2.2 Reynolds-averaged Navier-Stokes (RANS) method

The RANS method is widely employed in the industry as it is much less expensive in terms of computational demand, and more importantly it can give satisfactory predictions if the model is properly set. RANS takes a statistical view on the flow field and completely averages the control equations. From the view of RANS, the field variables, such as the velocity u, contain a mean component ($\overline{u}$) and a fluctuating component (u'). The fluctuating component is assumed to have a mean value of 0 ($\overline{u}' = 0$). Therefore, u can be decomposed as:

$$u = \overline{u} + u' \tag{2.10}$$

Applying the RANS decomposition to the momentum equation, the averaged momentum equation, namely the RANS equation, can be written as:

$$\frac{\partial(\rho u_i)}{\partial t}+\frac{\partial(\rho u_i u_j)}{\partial x_i}=-\frac{\partial p}{\partial x_i}-\frac{\partial}{\partial x_j}(\rho\overline{u_i' u_j'})+\frac{\partial}{\partial x_i}\left(\mu(-\frac{2}{3}\delta_{ij}\frac{\partial u_l}{\partial x_l}+\frac{\partial u_i}{\partial x_j}+\frac{\partial u_j}{\partial x_i})\right) \tag{2.11}$$

Temporal term | Convention term | Pressure difference | Reynolds stress | Viscosity

In the above equation, the additional term “Reynolds stress” is the product from the RANS decomposition that needs to be modelled by the turbulent models, which includes the eddy-viscosity models and the Reynolds stress models.

The eddy-viscosity models are based on the Boussinesq hypothesis [97], which assumes the Reynolds stress is proportional to the mean strain rate and the Reynolds stress is modelled as:

$$-\rho\overline{u_i' u_j'}=\mu_t(\frac{\partial u_i}{\partial x_j}+\frac{\partial u_j}{\partial x_i})-\frac{2}{3}(\rho k+\mu_t\frac{\partial u_k}{\partial x_k})\delta_{ij} \tag{2.12}$$

where μ_t is the turbulent eddy viscosity, k is the kinetic energy and δ_{ij} is the Kronecker delta. It should be noted that the turbulent eddy viscosity μ_t needs to be modelled and a number of models have been developed for this. The Prandtl mixing length model [98] is a zero-equation model that assumes that the turbulent viscosity is proportional to the square of the length scale. The Spalart Allmaras model [99] is a one-equation model that solves a viscosity variable in a transport equation, then the viscosity variable can be used to calculate the turbulent viscosity. In addition, the two one-equation models for modelling the turbulent viscosity include the $k-\varepsilon$ and the $k-\omega$ models, which employ two additional transportation equations for the turbulent kinetic energy k and either the turbulent dissipation rate ε or the specific dissipation rate ω ($\omega=\varepsilon/k$). The turbulent viscosity μ_t is calculated as a function of k and ε or ω. A main advantage of these models is their comparatively low requirements on the computational resources.

The $k-\varepsilon$ models have a number of variants, such as the standard $k-\varepsilon$ [100], RNG $k-\varepsilon$ [101] and the realisable $k-\varepsilon$ model [102]. The standard

$k-\varepsilon$ model assumes that the flow is completely turbulent and ignores the effects of the molecular viscosity, thus this model can be only used for fully turbulent conditions. In order to apply the standard $k-\varepsilon$ model to other situations, modifications have been made, and hence the RNG $k-\varepsilon$ and the realisable $k-\varepsilon$ models were proposed. The RNG $k-\varepsilon$ model is based on the statistical renormalisation group approach and it introduces an additional term for the ε equation so that the accuracy for the low-Reynolds and strained flows is improved. The RNG $k-\varepsilon$ model has been used in the pulverised coal combustion simulations [103, 104]. As another variant, the realisable $k-\varepsilon$ model depends on a modified ε transport equation so that the model satisfies certain mathematical constraints on the Reynolds stress, which are not realised in the standard $k-\varepsilon$ or the RNG $k-\varepsilon$ models. It should be pointed out that both the RNG and realizable $k-\varepsilon$ models are able to give more accurate predictions of the flows involving strong vortices and rotations, compared to the standard $k-\varepsilon$ model. The standard $k-\omega$ model [105] and the shear-stress transport (SST) $k-\omega$ model [106] both employ transport equations for k and ω. The standard $k-\omega$ model is suitable for the low-Reynolds number and shear flows. The SST $k-\omega$ model blends the accuracy and the robustness near the wall and employs an additional derivative term in the ω transportation equation. Therefore, the SST $k-\omega$ model can be applied to a wider range of flows with adverse pressure gradients and separating effects.

The Reynolds stress model (RSM) [107, 108], is a more advanced RANS model as it does not require the isotropic assumption which is used in the previously introduced turbulent models. In order to solve the Reynolds-averaged Navier-Stokes equations, the RSM introduces additional transport equations for the Reynolds stress as well as the dissipation rate. Therefore, seven transport equations are involved in a three dimensional problem, which results in the computational cost being increased.

2.2.2.3 Large eddy simulation (LES)

A turbulent flow contains numerous eddies with different temporal and spatial scales. The RANS approaches apply a Reynolds-average on all the eddies, and thus all instantaneous information of the eddies are ignored. In

the LES method, only the small eddies are modelled, while the larger eddies are directly resolved. Therefore, the overall computational cost required by LES lies between those of RANS and DNS.

Compared to DNS, much coarser grids and larger time steps are allowed in LES, since only the large eddies are resolved. However, when compared to RANS, LES requires a much finer grid and smaller time steps, and thus a LES simulation requires much larger computational resources and longer computation time in order to obtain converged predictions. The practical use of LES in the industry needs to be implemented by the employment of high-performance computers.

In order to distinguish the larger eddies from the small eddies, the LES applies a filter [109] to the Navier-Stokes equations, and the filtered momentum equation can be written as:

$$\frac{\partial(\rho u_i)}{\partial t}+\frac{\partial(\rho u_i u_j)}{\partial x_i}=-\frac{\partial p}{\partial x_i}+\frac{\partial}{\partial x_i}\left(\mu(-\frac{2}{3}\delta_{ij}\frac{\partial u_l}{\partial x_l}+\frac{\partial u_i}{\partial x_j}+\frac{\partial u_j}{\partial x_i})\right) - \frac{\partial}{\partial x_j}(\rho\overline{u_i u_j}-\rho u_i u_j) \tag{2.13}$$

A new term ($\rho\overline{u_i u_j}-\rho u_i u_j$) on the right-hand side of the equation, namely the sub-grid-scale (SGS) stresses, is generated from the filtering and needs to be modelled for the small scale eddies. The SGS stresses contain a deviatoric and a isotropic part, which can be treated as the filtered static pressure [110]. A number of models have been developed to solve the SGS, such as the Smagorinsky-Lilly model [111], the dynamic Smagorinsky model [112, 113], and the wall-adapting local eddy-viscosity model [114].

Edge et al. [54] employed a LES approach in a CFD model to simulate the firing of a pilot-scale pulverised coal furnace under both air-coal and oxy-coal conditions. The predictions from the LES was compared to the experimental data as well as the results predicted by a RANS approach incorporating the standard $k-\varepsilon$ model. The comparison indicated that the LES approach is able to give more accurate predictions on the recirculation and flame properties than the RANS method .

Similarly, Gharebaghi et al. [55] employed LES and RANS to simulate a 1 MW_{th} combustion test facility under both air-coal and oxy-coal environments. The predictions from LES were compared to RANS and experimental data and it was found that although LES was able to capture more realistic details of the flame, the improvement on the temperature predictions was not significant. The authors suggested that further fundamental investigations and improvements on the physical sub-models are necessary. In this case, Clements et al. [115] evaluated the LES and the RANS models in the simulation of a pilot-scale 250 kW_{th} furnace under both air-coal and oxy-coal conditions. The investigation employed the grey WSGG model and the non-grey FSCK model to calculate the radiative properties of the gas phase. It should be noted that both the WSGG and the FSCK models were integrated with RANS, while only the FSCK model was used with LES. The simulation results indicated that the variation in the gaseous radiative property models does not significantly change the temperature or heat transfer predictions for the RANS cases, while the LES combining with the FSCK model was observed to provide more accurate results compared to the RANS model. However, the interaction between LES and the grey WSGG model was not investigated, thus a conclusion on the efficiencies for different combinations of the turbulent and radiation models could not be drawn.

Considering the complexity as well as the high computational demand of LES, a RANS approach rather than the LES is used to model the turbulence in the later part of this thesis. It should be pointed out that CFD simulation of the coal combustion in a boiler is not the final target. This thesis integrates the CFD techniques with process simulation approaches in the simulation of the carbon capture technologies so that a number of three dimensional CFD simulations need to be performed, and thus it is not necessary to depend on LES.

2.3 Carbon capture process modelling

The post combustion and the oxy-coal combustion technologies are the carbon capture technologies that can be applied to either the existing or the new built coal (or biomass) fired power plants. System process simulation plays an important role in the development of the industries because it

assists engineers to better understand the operations, responses and performances of the whole system and it is able to predict the optimised operating conditions of the system, and therefore a large amount of expenditure on experiments can be saved. This section provides a brief literature review on the process modelling techniques with regard to these two technologies.

2.3.1 Chemical absorption process modelling

A well identified advantage of using the post combustion techniques is that this type of technologies requires the least modification to the original combustion system. Post combustion technology refers to a set of approaches that capture the CO_2 from the flue gas after the combustion process and the major approaches are the chemical absorption, adoption and membrane separation [116]. However, chemical absorption is the only technology that has the potential to be applied in large-scale commercial power plants.

2.3.1.1 General process treatment

In the chemical absorption process, CO_2 in the gas phase is absorbed by a chemical solvent via chemical reactions to generate an unstable intermediate compound, which then can be post-processed to regenerate the original chemical solvent and release a high-purity CO_2 stream [117]. A number of amine solvents can be used to absorb CO_2 and these solvents have different absorption capacities, chemical stability and different corrosion factors [118]. Currently, MEA is the most popular solvent for capturing CO_2 from pulverised coal power plants [19], as it is able to treat the flue gas containing low CO_2 concentrations.

Before the absorption process, some trace gases in the flue gas, such as SO_x and NO_x, need to be removed because they may react with the MEA to form other salts, thus the MEA solvent may be degraded. The removal of SO_x can be achieved by allowing the flue gas pass to through a flue gas desulphurisation (FGD) equipment, while the NO_x can be removed by a selective catalytic reduction (SCR) device. In addition, the ash particles in the flue gas has to be separated out as the solid particles may accumulate

and block the pipe lines of the CO_2 capture plant and the removal of the ash content can be performed by an electrostatic precipitator (ESP).

In Figure 2.2, the flow diagram demonstrates a CO_2 absorption process using a MEA solvent. Flue gas entering the absorber has to be cooled down to about 320 K, which is identified as a feasible temperature range that could reduce the solvent loss from evaporation and provide a suitable initial temperature for the absorption reactions [119]. In the absorber, the rising flue gas contacts with the downward lean MEA solvent flow and CO_2 is absorbed, and therefore a rich solvent is produced at the bottom of the absorber. The typical CO_2 loading of the lean MEA solvent is between 0.1-0.3 (mol CO_2 per mol MEA), while a rich loading is usually between 0.4-0.5 [120]. During the CO_2 absorption, heat is released from the chemical reactions and the temperature of the lean solvent increases, which leads to the evaporation of the water content, and thus the MEA solvent becomes more concentrated. Therefore, in order to maintain the water balance in the solvent, the treat flue gas undergoes a water wash process so that the moisture can be condensed and recycled to the solvent.

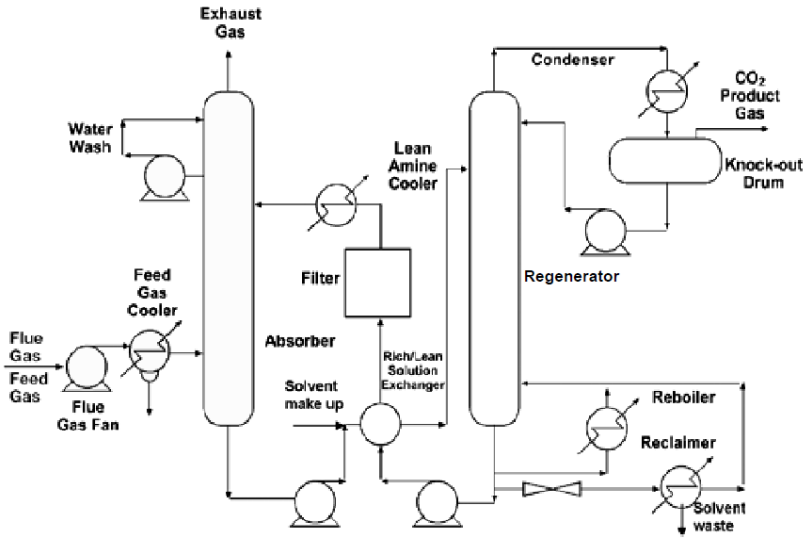

Figure 2.2 A process flow diagram for CO2 capture using chemical absorption approach [117].

The rich solvent from the absorber is pre-heated in a lean/rich solvent cross-heat-exchanger by the regenerated lean solvent produced from the regenerator (or “stripper”). Then the pre-heated rich solvent is passed to the top of the regenerator, where the temperature generally varies between 373-

413 K [117]. The regeneration of the lean solvent and the release of CO_2 requires an external heat input, which can be supplied to the reboiler at the bottom of the regenerator. In a power station that incorporates a CO_2 capture plant, the high temperature steam, which can be extracted from the intermediate or the low pressure steam turbine, is passed to the reboiler to provide the required heat input. However, the steam extraction would cause a significant energy penalty to the power plant. At the top of the regenerator, a condenser is used to recycle the steam and MEA and thus further purify the CO_2 stream.

2.3.1.2 Reaction kinetics for the CO_2 absorption using MEA solvent

Vaidya et al. [121] summarised the major chemical mechanisms describing the CO_2 absorption by alkanolamines, namely the Zwitterion, Termolecular and the Base-catalyzed hydration mechanisms. As a primary amine, MEA absorbs CO_2 through a set of reactions occur in the liquid, which can be described by the Zwitterion mechanism. The Zwitterion mechanism, developed by Caplow [122], assumes that the reaction between CO_2 and amine (denoted as AmH) can be split into two steps, but in the first step a Zwitterion ($\mathrm{AmH^+COO^-}$) is introduced as an intermediate compound:

$$\mathrm{CO_2 + AmH \underset{k_2}{\overset{k_1}{\rightleftharpoons}} AmH^+COO^-} \tag{2.14}$$

where $\mathrm{k_1}$ and $\mathrm{k_2}$ respectively, denote the forward and backward reaction rate. Then the Zwitterion undergoes deprotonation by a base B, therefore a carbamate is formed:

$$\mathrm{B + AmH^+COO^- \xrightarrow{k_3} AmCOO^- + BH^+} \tag{2.15}$$

where $\mathrm{k_3}$ is the rate of deprotonation. Then combining the reactions (2.14) and (2.15), the absorption rate of CO_2 can be written as:

$$r = \frac{k_1[\mathrm{CO_2}][\mathrm{AmH}]}{1 + \dfrac{k_2}{k_3[\mathrm{B}]}} \tag{2.16}$$

where $k_3[\mathrm{B}]$ is the deprotonation rate of the Zwitterion by the base B, which could be $\mathrm{H_2O}$, $\mathrm{OH^-}$ and AmH or a combination of bases. When the deprotonation occurs at a much faster rate compared to the backward

reaction in (2.14), i.e. $k_3[\mathrm{B}] \gg k_2$, then the absorption rate of CO_2 can be simplified as follows:

$$r = k_1[\mathrm{CO_2}][\mathrm{AmH}] \tag{2.17}$$

and the rate constant k_1 was given in [123] as follows:

$$\log(k_1) = -\frac{2152}{T} + 10.99 \tag{2.18}$$

Adversely, when the deprotonation rate is much slower than the backward reaction in (2.14), i.e. $k_2 \gg k_3[\mathrm{B}]$, absorption rate of CO_2 becomes:

$$r = \frac{k_1 k_3[\mathrm{B}]}{k_2}[\mathrm{CO_2}][\mathrm{AmH}] \tag{2.19}$$

In this condition, the contribution of amine to Zwitterion becomes important and the overall reaction is second-order with respect to the amine.

2.3.1.3 Modelling approaches

Generally, two types of modelling methods are available to model the CO_2 absorption process, namely the equilibrium-based and the rate-based approaches. The gas-liquid phase equilibrium is assumed in the equilibrium-based approach, which employs a set of efficiency factors to describe the efficiencies of the thermal stages [124], while the rate-based approach directly solves the conservation equations for the mass transfer, heat transfer and reaction kinetics [125].

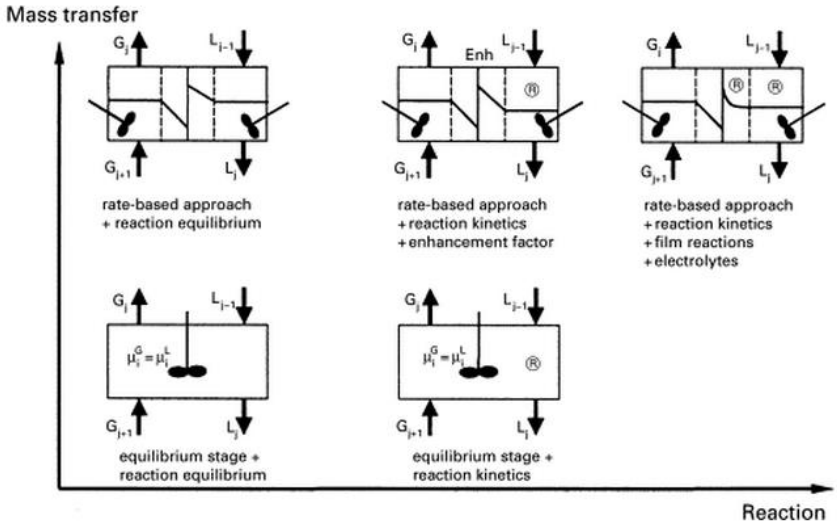

Figure 2.3 Descriptions of reactive absorption models with different abilities to describe the mass transfer and reaction kinetics [125].

A set of model descriptions of the chemical absorption process has been summarised and classified in [125] according to their ability to treat the complexity of the mass transfer and reaction kinetics. These descriptions are shown in Figure 2.3.

In Figure 2.3, the simplest model ignores the reaction kinetics and assumes the mass transfer is so fast that equilibrium is reached instantly. Moving rightwards, the model abilities are improved by considering more effects, such as the reaction kinetics in the bulk phase or in the liquid film. Moving upwards, the actual dynamic mass transfer effect is considered, and hence the models become rate-based so that other considerations, such as the effects of the electrolyte, can be included. Therefore, the kinetic model at the top right of Figure 2.3, which involves the mass transfer effect accelerated by the reactions in the liquid film, is considered to have the highest fidelity, however, the computational cost is significantly increased.

2.3.1.4 Mass transfer methods

In the rate-based models, the main approaches for describing the mass transfer phenomena between the vapour phase and the liquid phase are the two-film theory [126] and the penetration theory [127].

The two-film theory assumes that both the liquid phase and the vapour phase have very thin film regions adjacent to the bulk regions. The liquid film and the vapour film are separated by an interface between the phases. In the bulk regions of the liquid and vapour, the compositions are assumed to be uniform. Also the two-film theory assumes that the resistance for the mass and heat transfer is concentrated in the films and the resistance is a function of the film thickness, physical and chemical properties of the liquid and vapour species [128].

The penetration theory assumes that the molecules in the liquid phase move randomly in various directions and these molecules could reach the interface and remain exposed to the vapour phase for the same length of time. During the exposure time, some molecules penetrate the interface and the rest is mixed back to the bulk. The length of the exposure time is determined by the hydrodynamic properties [128].

2.3.1.5 Modelling activities on CO_2 capture using chemical absorption

Process modelling is an important tool that assists in the design and demonstration of the post-combustion CO_2 capture process for power plants. A number of investigations, using process modelling techniques, has been performed to identify different characteristics of running the CO_2 capture process alone or with power plants.

Kvamsdal et al. [129] numerically investigated a 450 MW_e natural gas combined power plant with a post-combustion CO_2 capture plant using MEA. It was found that the 90% CO_2 capture level would bring a 9% energy penalty to the original power plant.

Liu et al. [130] studied post-combustion CO_2 capture with MEA for a super-critical coal fired power plant. Different positions for the steam extraction from the steam turbines were evaluated and it was found that the efficiency penalty was slightly lower (about 12.3%) if the steam was extracted at a lower pressure. In addition, by using the waste heat from the CO_2 capture process and some other minor modifications to the original diagram of the process models, the energy penalty can be further reduced by about 2.5%.

Nagy et al. [131] developed a computer based absorber-desorber model to evaluate the CO_2 capture from different types of flue gases and the simulation results indicated that the rate-base model could give more accurate predictions compared to the equilibrium stage model. In addition, the authors concluded that the fuels having low carbon content and high heating values are helpful to achieve a higher net CO_2 removal efficiency.

Lawal and Biliyok et al. [132, 133] performed dynamic modelling of the post combustion CO_2 capture process using MEA. Both the equilibrium-based approach and the rate-based approach were used in the dynamic absorber model and their results were compared to the experimental data and it was found that the rate-based approach could produce more realistic predictions. In addition, the dynamic simulations revealed that the normal operation of the absorber can be maintained under part load conditions if the liquid/gas ratio is maintained the same. However, variation in the CO_2 loading of the lean MEA solvent would disturb the performance of the absorber. Further, Lawal et al. [134] found that the performance of the absorber is more likely

to be affected by the liquid/gas ratio than the mass flow rates of the lean MEA solvent and flue gas. Again, Lawal et al. [135] integrated a large-scale post-combustion CO_2 capture plant model with a 500 MW_e sub-critical power plant model in a dynamic scheme and found that the CO_2 capture plant has a slower response than the power plant. Also the results indicated that higher MEA concentration in the lean solvent could bring a higher plant efficiency, however, it should be noted that a high MEA concentration in the solvent is more likely to cause corrosion.

2.3.2 Oxy-coal combustion process modelling

The oxy-coal technology provides a promising alternative for reducing the CO_2 emissions from conventional coal-fired power plants by employing an air separation unit (ASU) and a flue gas recycle (FGR) loop. Oxy-coal technology is able to significantly increase the CO_2 concentration in the flue gas and this makes the following CO_2 sequestration efficient and convenient. System process simulation has been successfully applied in predicting and optimising the operation of the power plants using oxy-coal techniques. This section reviews the current investigations on the process simulation of the oxy-coal power plants.

Hu et al. [136] performed process analyses on a power generating system with a oxy-coal CO_2 capture technique. Different locations for recycling the flue gas were evaluated to show their impacts on the radiative properties of the recycled flue gas. It was indicated that the disturbances to the gas emissivity and absorptivity are about 15%and 20%, respectively, thus the overall effects on the heat transfer can be about 20%. However, the authors used simplified empirical correlations to calculate the gaseous emissivity and absorptivity and no experimental data was available.

Haryanto et al. [137] developed a numerical model for an oxy-coal combustion boiler system with a flue gas recycle. The authors simplified the mass and energy balance equations to a set of linear equations based on a steady-state operating condition. The simulation results were found to have satisfactory agreement with the experimental data. Again, the heat transfer properties of the gaseous were predicted using empirical equations, which were originally developed for air-coal firing conditions.

Jin et al. [138] performed dynamic simulations in order to investigating the switching process between the air-coal firing and the oxy-coal scenarios in a 600 MW_e oxy-coal combustion system. The results obtained showed that “manipulating oxygen and recycled flue gas streams with different ramp rates of corresponding valve positions during different switching stages while manipulating air stream with a constant ramp rate of air valve position throughout the switching process could be an effective switching strategy” [138]. In addition, an optimal switching time of 17 min was suggested as it could achieve a stable switching process between the air-coal and the oxy-coal firing conditions.

Gopan et al. [139] investigated a staged-pressurized oxy-fuel combustion process, which may increase the overall plant efficiency by reducing the power required by the auxiliary devices for the flue gas recycle and flue gas post-processing. The simulation results showed that this oxy-fuel combustion approach was able to increase the plant efficiency by about 6% compared to the traditional oxy-fuel combustion technologies. However, this approach requires substantially more modifications to the original air-coal firing power plants, and thus this approach requires more installation expenditure and may not be suitable for the existing air-firing power plants.

2.3.3 CFD and process co-modelling activities

It should be noted that the previous investigations that were introduced in the Sections 2.3.1 and 2.3.2 completely depend on process simulation techniques, which are usually based on zero or one-dimensional equations with empirical constants to calculate the heat transfer properties of the combustion gas in the boiler. However, these constants, which were usually identified for conventional air-coal firing conditions, may not be appropriate to be employed in oxy-coal combustion conditions with confidence. In addition, these equations are insufficient to consider the exact geometries and arrangements of the heat exchangers in the boilers, which could affect the distribution fractions of the heat transfer to different heat exchangers in the boiler. Also these distribution fractions may vary between the air-coal and the oxy-coal firing conditions, however, in traditional process simulations these fractions are treated as constants.

Therefore, it becomes the state-of-the-art to use the CFD and process co-simulation techniques, as CFD is able to accurately incorporate the three-dimensional boiler geometries, heat transfer distributions and the fundamental properties of the combustion gas, which are difficult to be properly modelled in pure process simulations. However, it is impractical to fully depend on the CFD modelling techniques to simulate the whole chain of the system in addition to the boiler, which include other components such as the steam turbines, fluid transport pipes, fluid pumps, compressors, columns and flash drums, because three-dimensional CFD modelling normally requires far more computational time and resources compared to the process modelling, hence a combined CFD and process co-simulation strategy is necessary.

Few investigations have been performed attempting to integrate the CFD modelling approach with process modelling with regard to the oxy-fuel combustion technique. However, no such attempt has been performed on the post-combustion technique.

Lee et al. [140] performed CFD and process co-simulations for a biomass fast pyrolysis process, which provides a meaningful reference for modelling the carbon capture technologies. The authors employed a simplified two-dimensional CFD modelling approach to account for the pyrolysis reactor and the process simulation platform directly outputs the inlet conditions to the CFD simulation software, which then returns the predicted outlet results to the process modelling tool so that a direct co-simulation can be achieved. However, this direct coupling between CFD and process modelling is impractical to be applied to three-dimensional combustion boiler simulations, which demand much more extensive computational expenditures compared to the two-dimensional simulations where the size of the computational mesh is smaller by tens to hundreds of times.

Edge et al. [141] developed reduced order models from the air-coal and oxy-coal firing CFD simulations for a 500 MW_e large-scale boiler of a power plant. The reduced order models were obtained by post-processing the CFD heat transfer predictions along the height of the boiler. Then, these reduced order models were integrated to the energy equations for the heat transfer to the

water walls, superheaters and reheaters of the boiler. With this co-simulation approach, the predicted steam generation from the boiler matched well with the benchmark data. Further, the authors extended this boiler model to a full-scale power plant model in order to identify an optimal oxygen enrichment for oxy-coal operations where the heat transfer characteristics and overall performances can be matched to the original air-coal power plant [142]. It should be noted that each reduced order model developed in these investigations can only account for a single operating scenario of the boiler under a specified oxygen concentration. However, in this case, if a different operating scenario needs to be investigated, then a corresponding CFD simulation needs to be performed. Therefore, this isolated integration between CFD and process modelling cannot efficiently cover the full working range of the power plants. In this case, further improvements on properly building the reduced order models is necessary and this part of work will be described in Chapter 6.

2.4 Summary

This chapter provides a detailed critical literature review on the modelling technologies with regard to the CO_2 capture technologies that can be applied to the existing or new built coal firing power plants.

In the first place, the fundamental combustion process of the pulverized coal is described and the corresponding modelling techniques accounting for the different stages of the coal combustion are discussed. These sub-models describe the coal combustion processes that have been integrated into the popular CFD codes, such as ANSYS FLUENT. Secondly, the treatment of the heat transfer and turbulence in CFD is discussed. Further, the process modelling techniques for the CO_2 capture approaches that can be applied to coal-fired power plants are reviewed. Considering the limitations of the process modelling, the combination of the process modelling and CFD modelling to achieve a co-simulation strategy is necessary. Relevant investigations on the CFD and process co-modelling techniques are discussed and their limitations are analysed.

Chapter 3. Experimental Facilities and Data

This chapter introduces the experimental facilities and the available data that are used for the system modelling and simulation in the upcoming chapters. In brief, the considered facilities are the Pilot-scale Advanced Capture Technology (PACT) facility, which consists of a 250 kW_{th} coal combustion test facility and an amine capture plant, and the large-scale Didcot-A 500 MW_e power station.

3.1 The 250 kW_{th} Combustion Test Facility (CTF)

This pilot-scale CTF is installed in an experimental site in Beighton, ward of Sheffield, and this is a part of the UK Carbon Capture and Storage Research Centre (UKCCSRC) Pilot-scale Advanced Capture Technology (PACT) facilities. Due to the lack of the first-hand documents on the configurations and measurements of this CTF, the content in the Sections 3.1.1, 3.1.2, 3.1.3 and 3.1.4 has been modified from [143] with the author's approval.

3.1.1 Facility introduction

This CTF is a vertically installed cylindrical furnace, which has a diameter of 0.9 m and a height of 4 m. A number of measurement probes are installed on the inner wall along the height of the furnace in order to take measurements on different operating conditions.

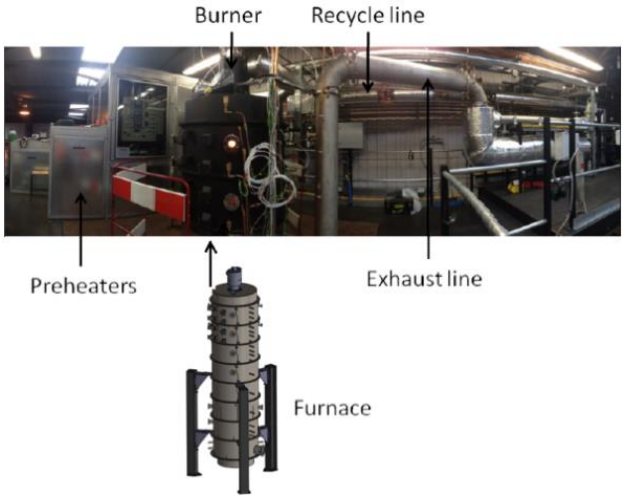

Figure 3.1 Layout of the 250 kW_{th} CTF and a CAD image of the furnace [143].

Figure 3.1 shows the layout of the CFT and also a CAD image of the furnace. The oxidant gas that enters the furnace can be preheated by a preheater and the flue gas can be directly emitted to the atmosphere via stack or treated by a MEA based CO_2 capture plant, which is also a part of the PACT facility.

It should be noted that a flue gas recycle line is also installed to recycle the flue gas into the furnace when a oxy-coal combustion operation is performed. The two and three dimensional imaging of the flow conditions inside the furnace can be achieved by employing the non-intrusive measurements, such as the particle image velocimetry (PIV) laser measurements. In addition, the temperature and the heat transfer conditions are measured by a set of intrusive measurements inside the furnace.

3.1.2 Burner description

A 250 kW_{th} low-NO_x burner produced by Doosan Babcock has been employed as the burner of the coal combustion furnace of the PACT facility.

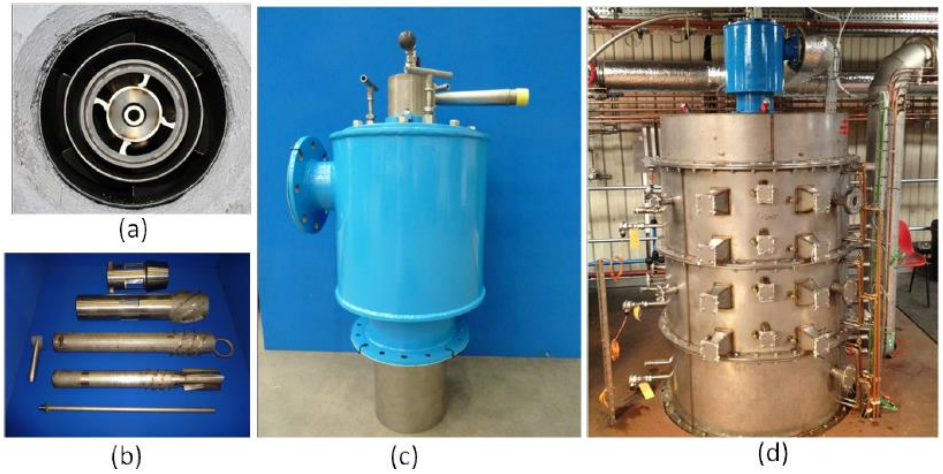

Figure 3.2 Images of the Doosan Babcock 250 kW_{th} coal burner [143]. (a) burner with the quarl; (b) disassembled view showing from top to bottom: damper for tertiary and secondary split, tertiary inner pipe, secondary inner pipe, primary inner pipe, gas pipe; (c) assembled burner before installation and (d) burner installed in the CTF.

Figure 3.2(a) presents the burner with the quarl, which is composed of a central inlet that offers an annulus transporting core air into the furnace to create the initial heating, a primary annulus with coal particles for the coal and carrier gas to get in the furnace, a flame holder that enhances the stability of the flame, and another two annuli (secondary and tertiary inlets) for the swirled oxidiser to be injected. The main components of the burner

are shown in a disassembled way in Figure 3.2 (b), while Figure 3.2 (c) shows the assembled burner that is installed on the top of the 200 mm deep refractory. In Figure 3.2 (d), a completely installed view of the burner is presented.

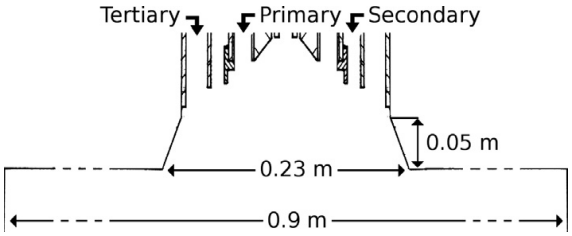

Figure 3.3 Sketch of the near burner region of the combustion rig.

There are three registers in the burner which are named the primary, secondary and tertiary, as marked in Figure 3.3. They function as the inlets for the combustion gases to be imported into the furnace, among which the primary annulus is used to deliver the coal and the secondary and tertiary ones are used to deliver the left oxidant gas.

3.1.3 Measurements

The gas temperature and radiative heat flux were measured in the experiments for the validation of the CFD models.

The gas temperature and the radiative heat flux in the furnace were measured for the validation of the CFD models.

The temperatures of the combustion gas are measured using a water-cooled IFRF Suction Pyrometer, which is shown in Figure 3.4. The gas temperatures are measured using a thermocouple, which is directly contacted with the flame, however, this could affect the original radiation in the surrounding region and this may introduce errors in the measurements [144]. The type R thermocouples are placed in the each 0.5 m section inside the furnace to measure the temperature. It should be noted that the type R thermocouples are not shielded, thus they could be affected by the radiation from the surrounding combustion gas, which may bring in some errors [143].

Figure 3.4 Images of the IFRF suction pyrometer showing the (a) rear view, and (b) front vi, showing radiation shield [143].

The Medtherm GTW-50-24-21 584 heat probes are used in each of the 0.5 m sections to measure the heat flux values and detached parts of the probe is shown in Figure 3.5. The probe contains a calcium fluoride window mount with a deflector that can deliver a nitrogen purge which cools the tip of the probe and deflects the combustion gases on the window. The window could also be removed and the deflector reattached to deliver a nitrogen purge and measure radiative heat transfer. With the window removed, the nitrogen could be turned off thus allowing the sensor to be exposed to conductive, convective as well as radiative heat transfer, resulting in total heat flux [143].

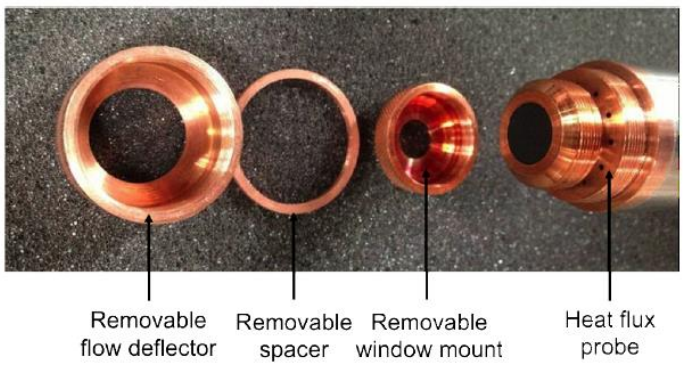

Figure 3.5 Images of a Medtherm GTW-50-24-21 584 heat probe [143].

3.1.4 Fuel specification

The fuel used was El-Cerrejon coal and the properties by ultimate and proximate analyses are presented in Table 3.1.

Ultimate analysis (w.t.%)		Proximate analysis (w.t.%)	
Carbon	73.67	Fixed carbon	59.26
Hydrogen	4.64	Volatile matter	40.74
Oxygen	11.32		
Nitrogen	2.48		
Sulphur	0.38	Calorific value (MJ/Kg)	
Ash	1.31	GCV	30.79
Moisture	5.81	NCV	29.49

Table 3.1 The El-Cerrejon coal analysis.

Normally, the coal particles are assumed to be spherical and such that the measured size distribution of the Pulverized El-Cerrejon coal can be fitted to a Rosin-Rammler size distribution [145], which assumes that the particle size distribution is governed by the Equation (3.1) for the mass fraction Y_d of particles with a diameter greater than d.

$$Y_d = e^{-(d/\bar{d})^n} \tag{3.1}$$

The exponential curve fit is illustrated in Figure 3.6 and the resulting parameters required to describe the size distribution are provided in Table 3.2.

Parameter	Value
Mean diameter $\bar{d}$ (μm)	110
Spread parameter n	1.1
Minimum diameter (μm)	1.0
Maximum diameter (μm)	600.0

Table 3.2 Parameters for Rosin-Rammler distribution.

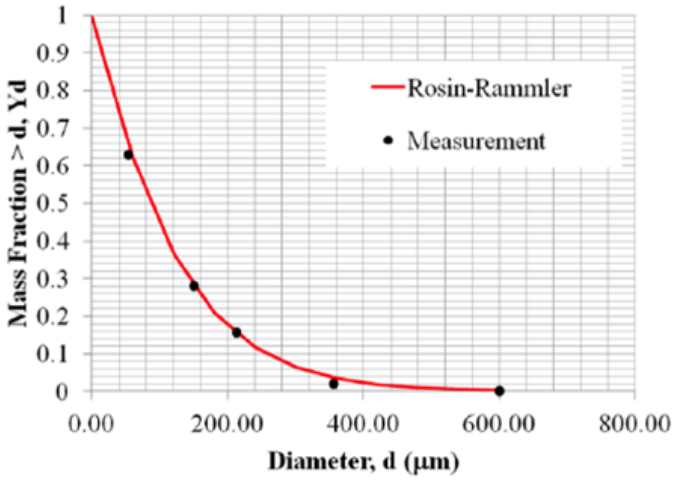

Figure 3.6 The fitted Rosin-Rammler curve [143].

3.1.5 Experimental settings

Two experiments were performed the thermal input of 200 kW_{th} under the air-coal firing condition. Table 3.3 shows the mass flow rates of the coal and air entering the furnace via the primary, secondary and tertiary inlets. In addition, the secondary and the tertiary air streams are preheated to be 524 K. In order to fully burn the fuel, the excess oxygen concentration by volume is controlled to be 3.5%.

Thermal input	200 kWth
Mass flow rate (kg/hr)	
Fuel (coal)	23.38
Primary	54.45
Secondary	93.35
Tertiary	124.44
Inlet air temperature (K)	
Primary	293
Secondary	524
Tertiary	524
Excess O2 (vol%)	3.5

Table 3.3 Operating conditions for the air-coal experiments.

In the experiments, measurements on the radiative heat flux and temperature were taken along the height of the furnace on the wall surface, and these results are represented in Figures 3.7 and 3.8.

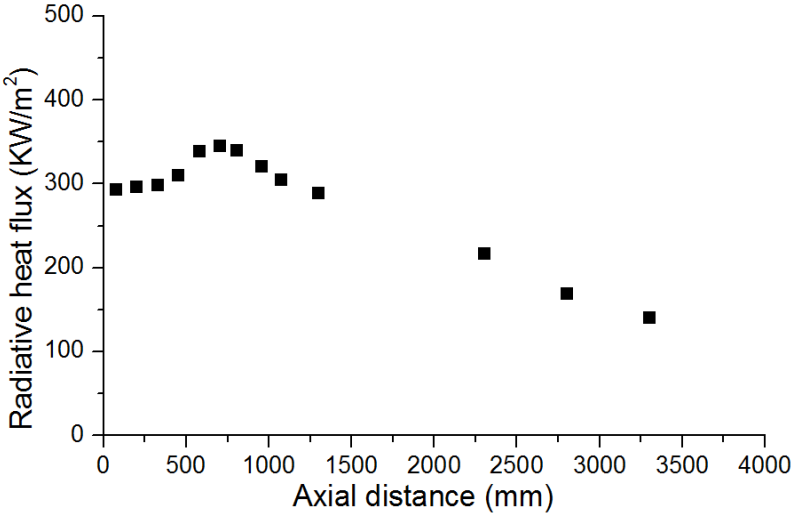

Figure 3.7 Measured radiative heat flux values along the inner wall of the furnace.

The radiation to the wall is directly affected by the temperature of the surrounding gas and thus the experimental data present a slight increase followed by a continuous decrease as the axial distance increases. It is interesting to find that along the axial direction, the gas temperature near the wall increases at first and then decreases due to the impact of the flame (its shape and contact to the wall).

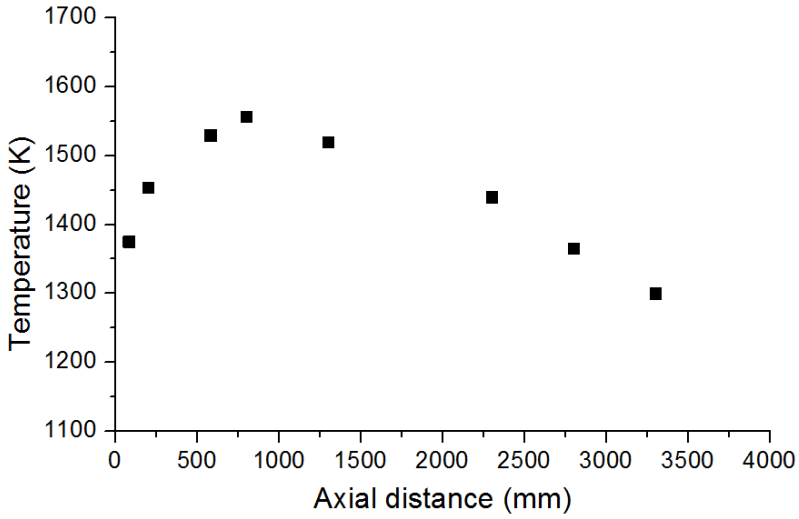

Figure 3.8 Measured temperature along the centre line inside the furnace.

It is observed that the gas temperature increases very quickly near the burner due to the ignition process in the quarl region then gradually decreases as the gas is further away from the burner.

3.2 The PACT amine capture plant

This CO_2 capture plant is a part of the PACT facility and it employs a MEA solvent to remove the CO_2 from the flue gas. As the flue gas leaves the coal combustion facility, the flue gas is cooled down to about 315 K in a direct contact cooler (DCC) and then passes through a flue gas desulphurisation (FGD) unit to remove the SO_2 content. After these treatments, the flue gas is passed to the PACT amine capture plant, which is described by a brief process flow diagram in Figure 3.9. The CO_2 capture section involves a absorber column, a water wash column and a stripper column. The water wash column is installed at the top of the absorber column in order to reduce the loss of MEA through evaporation. The stripper column has a condenser at the top and a reboiler at the bottom. The key operating parameters of the absorber and the stripper columns are shown in Table 3.4.

Parameters	
Height of packing (m)	6
Packing type	IMTP #40
Inner diameter (m)	0.303
Stripper condenser temperature (K)	315.2
Stripper reboiler temperature (K)	381.3
Norminal packing size (m)	0.0381
Packing specific area (m^2/m^3)	275

Table 3.4 The parameters for the absorber and the stripper columns.

The absorber and the stripper columns have the same values in the packing length, the nominal packing size and the specific packing area, which are 6 m, 0.0381 m and 275 m^2/m^3, respectively. The inner diameters of the absorber and the stripper columns are both 0.303 m. A more detailed description on the arrangement of the packing inside the absorber and the columns is shown in Figure 3.10 that both the columns have two sets of packing sections, each having a height of 3 m. The temperatures in the stripper condenser and reboiler are set to be about 315.2 K and 381.3 K, respectively, so that the required heat duties can be calculated and the sumps of the absorber and stripper can be modelled as buffer tanks.

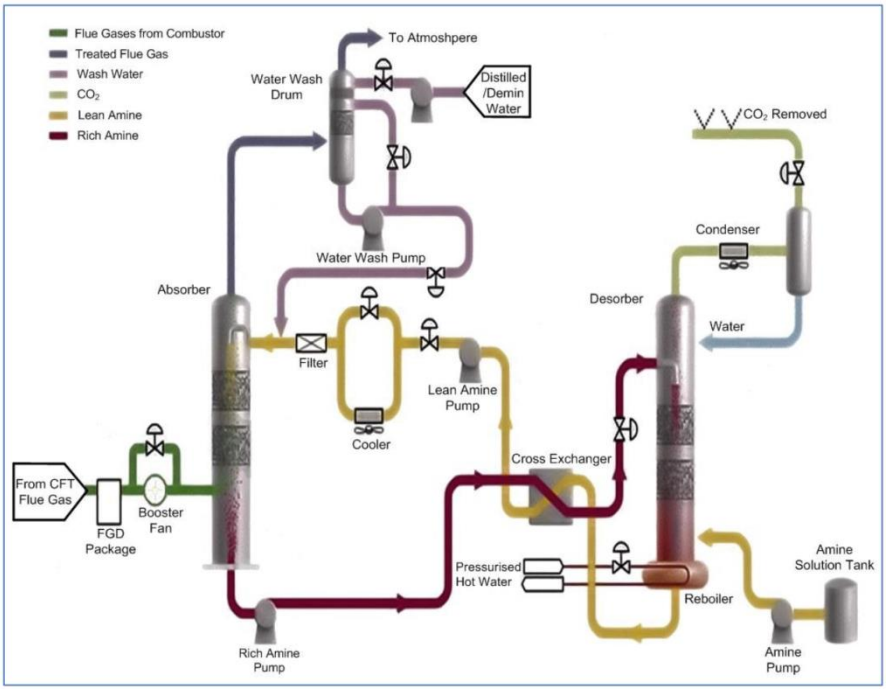

Figure 3.9 Process flow diagram of the PACT amine capture plant [146].

A cross heat exchanger between the lean and rich MEA is employed to reduce the additional heat duty required by the process. The lean MEA from the stripper is cooled by the rich MEA from the absorber, which operates at a lower temperature. However, the lean MEA solvent from the cross heat exchanger requires a further cooling down to about 313 K for optimal operation in the absorber and this is achieved by employing an additional cooler.

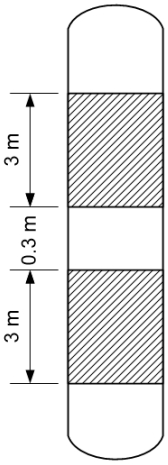

Figure 3.10 Configurations of the packing inside the absorber and stripper columns.

However, it should be noted that there is no experimental data from this CO_2 capture plant because this plant has been under retrofit since this research

started. Further information on the validation of the plant model will be provided in Chapter 4.

3.3 Didcot-A power plant

The 500 MW_e sub-critical Didcot-A coal-fired power plant [147] is employed to perform a set of large scale boiler CFD simulations as well as whole system process simulations in Chapters 5 and 6. A description of the power plant process is given in Section 3.3.1. The coal properties used by the furnace are provided in Section 3.3.2. The details of the furnace, and some of the some available measurement data from the furnace operation are supplied in Section 3.3.3. Further, some of the available measurement data from the furnace operation are summarised in 3.3.4. In addition, results from the RWE npower's in-house model for Didcot-A power plant are summarised in Section 3.4.

3.3.1 Configurations of the power plant

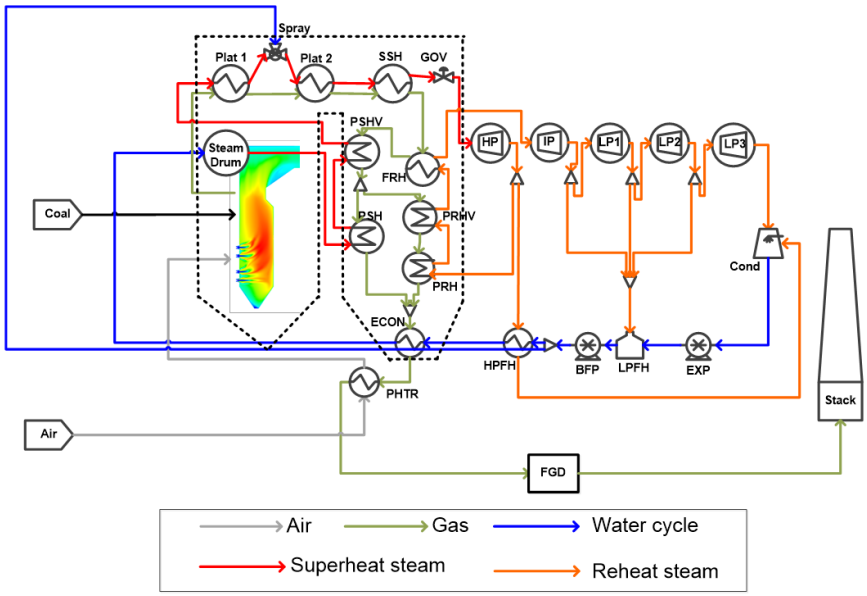

Figure 3.11 Layout of the Didcot-A power plant.

A brief layout of the Didcot-A power plant is shown in Figure 3.11 and the functionalities of the essential components are summarised in Table 3.5. In Figure 3.11, the material streams are defined as "Air", "Gas", "Water cycle", "superheat steam" and "reheat steam", according to the main materials contained in the stream. The main reason for defining specific material types is in order to show clearly the different pipe lines and their usages. A

detailed description on the working process of the power plant is provided in Chapter 5

Names of the units	Simple instructions for the units
Cond	Steam condenser
EXP, BFP	Pumps, pressurize the feeding water
ECON	Economiser, preheat the feed water
Furnace	Furnace
FGD	Flue gas desulphurisation
GOV	Governor valve, control the steam mass flow rate into the high pressure steam turbine
PHTR	Preheater, heating the inlet air or oxygen
Plat1, Plat2, SSH, FRH	Radiative superheaters Platen1, Platen2, SSH, FRH
PSHV, PSH, PRHV, PRH	Convective heat exchangers
HP, IP, LP1, LP2, LP3	Steam turbines, HP: high pressure, IP: intermediate pressure, LP: low pressure
Spray	Water spray, control the temperature of the steam goes into the Plat2
Steam Drum	Steam Drum, generating the high pressure steam
Stack	Exhaust the flue gas from air-coal firing or the impurities in the CO2 stream

Table 3.5 Essential components and instructions for the full plant.

3.3.2 Fuel specification

The fuel used in the power plant was a bituminous US coal, namely Pittsburgh 8, and a coal analysis is provided in Table 3.6.

Coal type: Pittsburgh 8			
Ultimate analysis (wt%)		Proximate analysis (wt%)	
Carbon	83.4	Fixed carbon	50.3
Hydrogen	5.5	Volatile matter	31.0
Nitrogen	1.6	Ash	10.3
Sulphur	2.6	Moisture	8.4
Oxygen	6.9	GCV (MJ/kg)	27.3

Table 3.6 The Pittsburgh 8 coal analysis

In order to improve the coal combustion efficiency, the coal needs to be pulverized before transporting to the furnace. The pulverized coal particle size distribution was obtained from a similar coal that was milled at Didcot-A

[141] and the distribution data indicates that most particle diameters lie between 1 and 300 μm with a mean of about 70 μm.

The devolatilisation rate of Pittsburgh 8 used in this study was documented in previous literature [104] and the tar combustion rate was chosen based on [47]. Arrhenius coefficients for char combustion were obtained from the experimental work performed by Williams et. al. [48] and are summarised in Table 3.7.

	Devolatilisation		Char combustion	
pre-exponential factor	A (s^{-1})	3.8×10^{14}	A_i $(\mathrm{kg\cdot m^{-2}\cdot Pa^{-1}\cdot s^{-1}})$	15.3
chemical activation energy	E_a $(\mathrm{J/kmol})$	2.3×10^{8}	E_{ai} $(\mathrm{J/kmol})$	1.52×10^{8}

Table 3.7 Coal combustion properties of Pittsburgh 8.

3.3.3 Boiler description

The coal-fired boiler is approximately 50m (height) × 30m (width) × 9m (depth). A Computer Aided Design (CAD) drawing of the coal-fired boiler and its burner is shown in Figure 3.12.

The heat released from the coal combustion in the boiler is transferred to the heat exchangers in order to evaporate water into high pressure steam which is then passed to the steam turbines to drive the generators and thus generate electricity. The boiler contains several heat exchange components, which are the water walls (surrounding the boiler), platen 1, platen 2, secondary superheater and the final reheater. Apart from these heat exchangers near the combustion zone, there are also heat exchangers further away from combustion zone and the heat transfer is dominated by convection. These convective heat exchangers are considered in the process modelling sector rather than in the CFD modelling. The heat exchanger platen 1 and 2 and the secondary superheater each contain 36 parallel tube banks and the final reheater has 74 tube banks. The wall thickness of these tube banks is about 5 mm. In addition, an ash hopper is installed at the bottom of the boiler in order to collect the ash from the coal combustion.

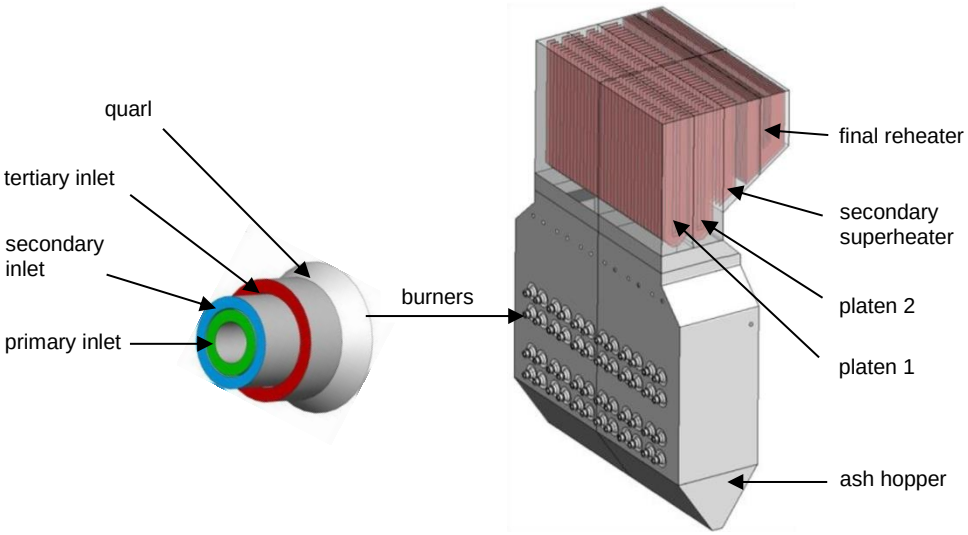

Figure 3.12 A CAD drawing of the boiler and its burner.

The boiler has 48 Doosan Babcock Mark-III low-NO_X burners and each burner contains 3 annular inlets, which are the primary inlet, the secondary inlet and the tertiary inlet. The pulverized coal enters the boiler via the primary inlets with the carrying air and the swirled air is delivered by the secondary and the tertiary inlets. The air mass flow split fractions and the swirl angels of the inlets are summarised in Table 3.8. The burner swirl direction may be clockwise or anti-clockwise and this is described in Table 3.9.

Inlets	Split fractions	Swirl angels
primary	20%	0^o
secondary	15%	25^o
tertiary	65%	50^o

Table 3.8 Flow split fractions and swirl angels of the burners.

Swirl directions (O = clockwise)		
XOXO	XOXO	XOXO
OXOX	OXOX	OXOX
XOXO	XOXO	XOXO
OXOX	OXOX	OXOX

Table 3.9 Swirl directions of the burners.

3.3.4 Boundary conditions and available data for the boiler

Some validation data was obtained from a typical air-coal firing case simulation, which was performed by the RWE npower's in-house MOPEDS

model [148] for the Didcot-A power plant simulation. The air-coal firing case modelled by MOPEDS was run at the full load condition and only 36 of the 48 burners were employed to inject the air and coal into the boiler. Table 3.10 outlines the boundary conditions of the air-coal firing case and Table 3.11 provides the predicted heat transfer values to different tube banks for the air-coal as obtained case from the MOPEDS model.

boundary conditions		
Total coal feed rate (kg/s)	46.7	
Air flow rates via different inlets of a burner (kg/s)	Primary	2.9
	Secondary	2.2
	Tertiary	9.5
Total air flow rate (kg/s)	525.6	
Inlet temperature (k)	Primary	363
	Secondary	530
	Tertiary	530

Table 3.10 Air-coal boundary conditions for the boiler at full load condition.

Heat transfer values from MOPEDS model (MW)	
Water walls	456
Platen 1	106
Platen 2	110
Secondary superheater	110
Final reheater	79
Total	861

Table 3.11 Heat transfer to different heat exchangers of the boiler at full load condition for the air-coal case obtained from MOPEDS.

Apart from the above heat transfer data, more results from the RWE npower's MOPEDS model are provided to validate the full plant model. These results include detailed predictions on the mass flows, temperatures and pressures of the whole plant system. Table 3.12 summarises the predicted gas and steam temperatures at the inlets and outlets of the heat exchangers. The predicted steam generation rate, pressure and steam pressure of the steam drum are presented in Table 3.13. Finally, the

predicted steam flows, pressures, temperatures and power outputs for the steam turbines are given in Table 3.14.

	Temperatures (K)			
	Gas		Steam/water	
	Inlet	Outlet	Inlet	Outlet
Plat 1	1656	1135	654	718
Plat 2	1441	1282	682	752
SSH	1338	1173	752	841
FRH	1173	1054	736	841
PSHV	1054	1027	648	654
PSH	1027	756	628	648
ECON	769	603	523	561
PRHV	1027	923	694	736
PRH	923	769	638	694

Table 3.12 The gas and steam temperatures of the main heat exchangers obtained by MOPEDS.

Steam generated (kg/s)	Drum pressure (bar)	Steam temperature (K)
390	178	628

Table 3.13 The steam generation rate, pressure and steam pressure of the steam drum obtained by MOPEDS.

	Steam flow (kg/s)		Pressure (bar)		Temperature (K)		Power output (MW)
	inlet	outlet	inlet	outlet	inlet	outlet	
HP	422.1	330.1	161	42.1	839	638	149
IP	330.1	328.6	40.4	6.46	814	585	169
LP1	337.2	310.2	6.46	3.33	583	522	40.7
LP2	310.2	291.3	3.33	0.82	522	399	72.5
LP3	291.3	291.3	0.82	0.05	399	306	89.4

Table 3.14 The steam flows, pressures, temperatures and power outputs from the steam turbines obtained by MOPEDS.

3.4 Summary

This chapter introduces a 250 kW_{th} pilot scale test facility and then the measurement technologies used in the facility is described. Specifically, the heat flux and gas temperature can be measured at several locations inside the test boiler. The air-coal firing experiments had been performed with the thermal inputs of 150 kW_{th} and 200 kW_{th} with this test facility so that the corresponding heat flux and temperature measurements were presented. This provides data required for the validation of the modelling and simulation work in Chapter 4.

Then the configurations of the PACT CO_2 capture plant are briefly introduced and this plant is used to capture the CO_2 from the flue gas generated by the 250 kW_{th} coal combustion facility. A CFD and process co-simulation on this whole system will be performed in Chapter 4. However, there is no experimental data available for the model validation of this CO_2 capture plant and this will be further discussed in Chapter 4.

In addition, a detailed description of a large scale power plant system, namely Didcot-A, and its boiler, has been presented. Particularly, the working procedures and the usages of the important components of the whole plant have been described. The high temperature combustion environment, especially in a large scale boiler, brings security issues for measurements. As a result, the measurement data is limited and hence the in-house model MOPEDS, developed by RWE npower for power plant simulation, can provide useful data. The MOPEDS model has been validated against the Didcot-A power plant's operation data so that the data obtained by this in-house model can be used as a validation for the whole system simulations in the upcoming chapters and the data from the MOPEDS model has been presented.

Chapter 4. Modelling and Simulation of a Pilot Scale CO_2 Capture System

In this chapter, a comprehensive CFD and process co-investigation on a pilot scale CO_2 capture system that was described in Chapter 3 is performed. In Section 4.1, predictions for the 250 kW_{th} air-coal combustion facility are completed using CFD techniques and the obtained results are compared to the available data from measuremental data. The flue gas from the 250 kW_{th} coal combustion facility is then passed an amine capture plant, as described in Chapter 3, so that the CO_2 in the flue gas is absorbed. However, it is unacceptable to use CFD techniques to model the CO_2 capture process in the amine capture plant since the CFD modelling of the complex chemical reaction processes and the multiphase flow inside the column are too expensive in terms of computational resources. Therefore, it is necessary to employ a process modelling approach to describe the CO_2 capture process in the amine plant and the newly announced commercial software gCCS [149] is used for this investigation. In Section 4.2, a detailed description on the process models developed in gCCS is provided and some model validations are performed where possible. In addition, the accurate prediction of the temperature and compositions of the flue gas entering the amine plant is important for the accurate simulation of the CO_2 capture process of the amine plant downstream of the combustion facility. Hence in Section 4.1, a set of reduced order models (ROMs) based on the CFD predictions of the combustion facility is developed in order to account for the temperature and compositions of the flue gas that leaves the combustion facility and enters the amine plant. So far, the CFD predictions have been linked to the process model for the amine plant via reduced order models. Then, this integrated CFD/process model is used to simulate the operations of the whole CO_2 capture system under different operating conditions and the results obtained are analysed. Finally, a brief summary on this chapter is provided in Section 4.3.

4.1 CFD modelling of the 250 kW_{th} air-coal combustion test facility

4.1.1 Numerical set-up

CFD techniques provide us useful tools to investigate numerous engineering configurations and each CFD simulation requires a mesh to be generated in order to represent the flow field around or inside the physical geometry that needs to be modelled. The significant capabilities of the commercial mesh generating softwares enable the complex geometries to be easily meshed. However, accurate meshing of the complex geometries usually results in a large number of mesh cells, which requires a large amount of computational resource (device and time) to solve the CFD problem. For instance, a large scale coal fired boiler used in a power plant may contain many heat exchange components, whose geometries are rather complicated, e.g. the water wall surrounding the furnace, the superheaters and the reheaters hanging at the top of the boiler and the economisers. In addition, the fuel burners installed on the boiler surface contain swirl blades and sub-inlets which make the geometry complex. It should be noted that the typical length scales describing the fluid flow in the boiler range from several centimetres (in the burners) to 30 - 50 meters. Accordingly, a large number of mesh cells are required in order to accurately represent the fluid regime in the boiler if the full details of fluid flow needs to be captured. However, this usually results in very high computational costs in solving the CFD problem and therefore, simplifications in the geometries of the coal fired burners are usually applied.

Considering the complexity of the burner and the measurement ports installed on the furnace wall of the 250 kW_{th} coal combustion facility, the geometries of the burner and the furnace are slightly simplified. Figure 4.1 shows a 3D CAD drawing, a 3D full mesh and a periodic mesh for the coal combustion facility and the meshes are generated using Ansys ICEM. The furnace is almost axisymmetric in the geometry, therefore a periodic mesh can be used. The hexahedral mesh is used to reduce the numerical error compared to the use of tetrahedral cells and the mesh is refined near the burner where the flow speed is the highest in the furnace and this refinement

is gradually reduced away from the burner exit where the flow speed is much lower.

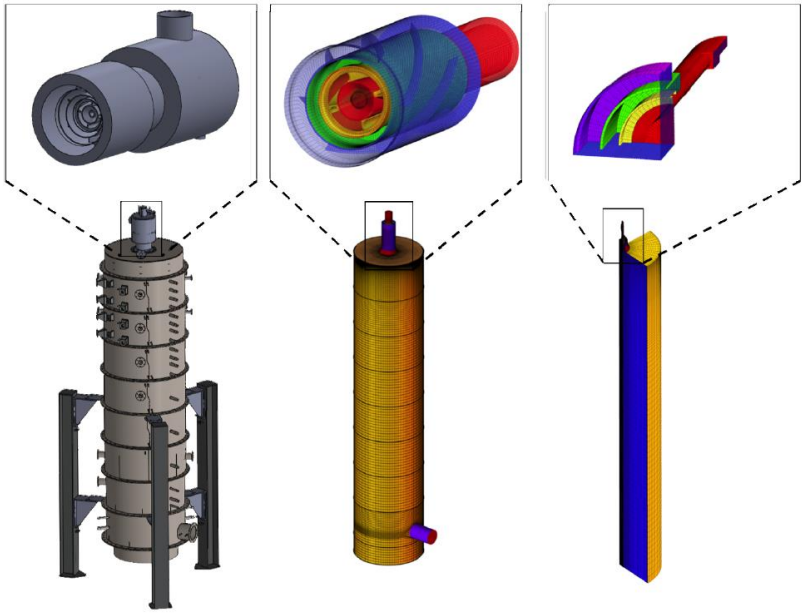

(a) (b) (c)

Figure 4.1 Burner and furnace (a) CAD drawings, (b) simplified full 3D mesh, and (c) simplified periodic mesh [143].

The coal burner installed at the 250 kW_{th} combustion facility is a low-NO_X burner provided by Doosan Babcock and Figure 4.2 shows a CAD cross sectional view of the burner. The burner achieves a low NO_X production by controlling the mixing of the pulverized coal and the oxidant gas. The NO_X is mainly generated in the hottest regime of the combustion flame when the oxygen is sufficiently supplied. Therefore, in this burner, the low NO_X production is achieved by limiting the flow rate of the primary air, which carries the pulverized coal, in order to create a central fuel-rich region and the rest of the air is passed to the furnace through the secondary and tertiary registers.

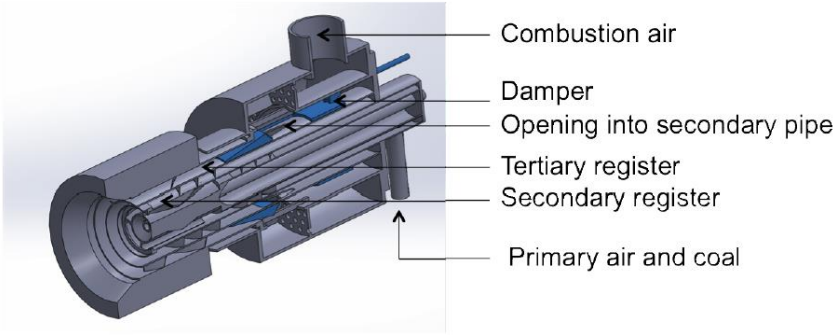

Figure 4.2 A CAD cross sectional view of the 250 kW_{th} Doosan Babcock burner [143].

Figure 4.2 also shows that the burner contains three registers, namely the primary, secondary and tertiary registers and the primary register delivers the pulverized coal with a part of the air to the furnace while the rest of the air enters the furnace via the secondary and the tertiary registers. Further, a damper is employed to control the shape of the combustion flame.

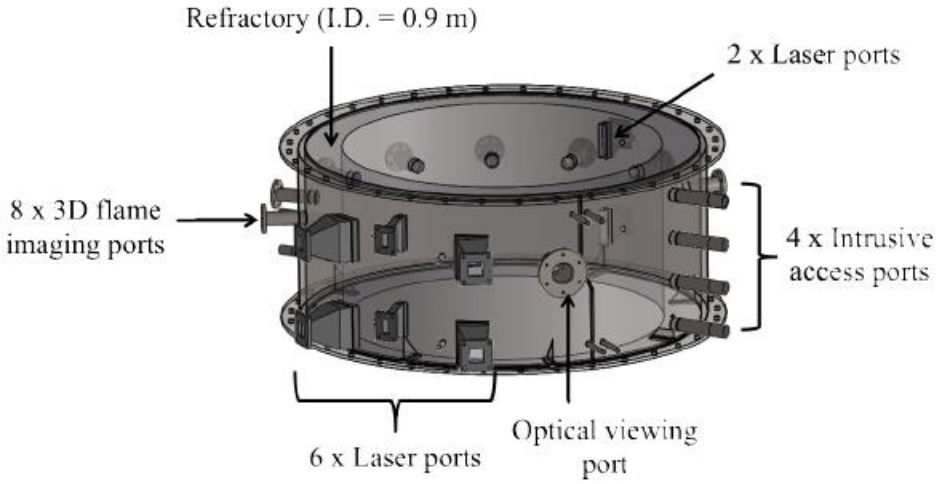

Figure 4.3 A CAD drawing of a typical section of the furnace [143].

Figure 4.3 shows a CAD drawing of one section of the furnace where a number of holes exists on the refractory wall in order to install devices for the optical and intrusive measurements in the furnace. The height of each section of the furnace is 0.5 m and the inner diameter of the furnace is about 0.9 m. The refractory of the first 2 sections has 8 3D imaging ports, 4 intrusive access ports and an optical viewing port while the other 6 sections have no flame imaging or laser ports but each has 4 intrusive ports.

In this investigation, the impacts on the flow field in the furnace due to the ports in the refractory are assumed to be negligible so that the furnace could be modelled as a cylinder and a full 3D mesh for the burner and the furnace is presented in Figure 4.1 (b). Moreover, it is assumed that the flue gas outlet in the last section of the furnace has an insignificantly influence on the CFD simulation results and thus the mesh can be further simplified to be periodic, as shown in Figure 4.1 (c). It should be noted that a thin wall boundary condition, in which the wall is modelled to be of zero thickness with an imposed heat flux condition, has been applied in order to account for the refractory and the surrounding water jacket. Typically, the total heat flux

through a wall under the thin wall boundary condition can be obtained by use of the following equation:

$$Q_{wall} = \frac{k_{wall}}{\Delta x}(T_{outer} - T_{inner}) + q_{rad} \tag{4.1}$$

where k_{wall}, Δx, T_{outer}, T_{inner} and q_{rad} are the thermal conductivity, thickness, temperature of the outer surface, temperature of the inner surface and the radiative heat flux, respectively. Specifically, the temperature of the outer surface of the of the wall is assumed to be the temperature of the cooling water while the inner surface temperature can be obtained by the turbulent law [150]. It should be noted that Eq.(4.1) can be only applied to 1D walls and annual walls whose inner radius increases only gradually along the axial direction.

Sub-models	Model Description
turbulence	Reynolds stress model [108]
devolatilisation	single-step model [39]
volatile combustion	eddy dissipation model with two-step chemistry [53]
	$C_xH_yO_zN_k + aO_2 \rightarrow bCO_2 + cH_2O + dN_2$
	$CO + 0.5O_2 \rightarrow CO_2$
char combustion	intrinsic model [66, 67]
	$C + O_2 \rightarrow CO_2$
soot formation	coal-derived soot model [76]
radiation	discrete ordinates method [82]
	absorption coefficients by WSGG [90]
	particle emissivity: 0.9 [143]
	particle scattering factor: 0.9 [143]

Table 4.1 Sub-models used in the CFD modelling of the 250 kW_{th} coal combustion facility.

The CFD simulations for the 250 kW_{th} air-coal combustion facility are performed using Ansys Fluent with a periodic mesh (285k cells, see Figure 4.1 (c)) and the sub-models employed are briefly described in Table 4.1. Since the flow from the burner is significantly swirled, the turbulence is modelled by employing the Reynolds stress model [108]. The devolatilisation process is modelled with the single-step model [39] and the volatile

combustion is accounted for by the eddy dissipation model with a two-step chemistry. The combustion of the char content is modelled by the intrinsic model [66, 67]. The radiative heat transfer is accounted for by the Discrete Ordinates (DO) model [82] and the absorption coefficients of the gas phase is calculated by a WSGG method where the model parameters are provided by Smith et al. [90]. The particle emissivity coefficient and scattering factor are set as constant values, both of which are 0.9. In addition, the effect of the particles including the soot particles, on the radiation has been considered and the soot formation is modelled using the coal-derived Moss-Brookes model [76].

It should be noted that before the CFD cases are finally set up, a grid independence study has been performed. Therefore, three sets of mesh, namely a coarse, medium and fine mesh, have been assessed in order to investigate how the CFD solutions are affected by the mesh size. The coarse, medium and the fine mesh contain 285k, 730k and 1.5 million cells, respectively. The predictions of the temperature profiles and gas compositions are used as an assessment criteria for the number of meshes required to obtain an accurate solution. We found that the three sets of mesh produce very similar results, and therefore the coarse mesh is chosen for the following investigation.

4.1.2 Model validation

An experimental investigation of the combustion facility has been performed at the 200 kW_{th} firing condition in order to provide some validation data in order to compare this data with the CFD results. Accordingly, a corresponding CFD simulation for the 200 kW_{th} operation of the combustion facility has been performed with a coal feed rate at 23.8 kg/hr. The split fractions for the air that enters the registers are 20% for the primary, 34.3% for the secondary and 45.7% for the tertiary. The temperature of the primary air is 293 K while the secondary and tertiary air is pre-heated up to a temperature of 528 K before entering the furnace. The outer temperature of the wall T_{outer} in Eq.(4.1) is taken from the measuremental data of the cooling water at each section. The section 1 of the furnace, which is at the top of the furnace, does not have cooling water circling around it, and therefore the

outer wall temperature is set to be 400 K based on the measurements taken during the experiment. Sections 7 and 8 of the furnace, which are the last two section, also do not have cooling water and since they are at the bottom of the furnace and are away from the combustion flame, they have lower outer wall temperatures compared to those that occur in section 1. In addition, the outer air temperature was recorded as being 5-10 ℃ during the experiment, and therefore the sections 7 and 8 are assumed to have an outer wall temperature of 300 K. The section 1 of the furnace has a wall thickness 0.2 m while the other sections have the same wall thickness, namely 0.1 m. The thermal conductivity of the refractory is set to be 0.27 $\mathrm{W/m \cdot K}$ which is based on the data given by the manufacturer.

A predicted temperature distribution inside the furnace is presented in Figure 4.4, where the primary, secondary and tertiary registers can be clearly viewed. The primary air, which carries the coal particles, is observed to mix with the secondary and tertiary air in the quarl region where the ignition of the coal particles occurs and heat is released, and therefore the gas temperature increases significantly. Moreover, the gas temperature is predicted to increase uniformly in the radial direction as the gas passes through the furnace.

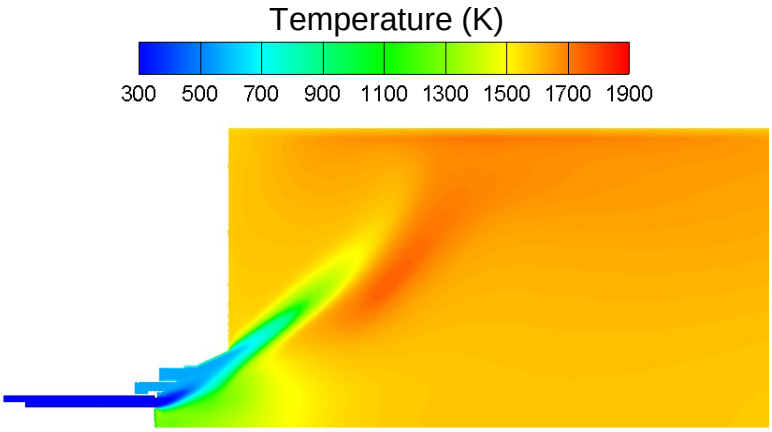

Figure 4.4 A predicted temperature distribution inside the furnace.

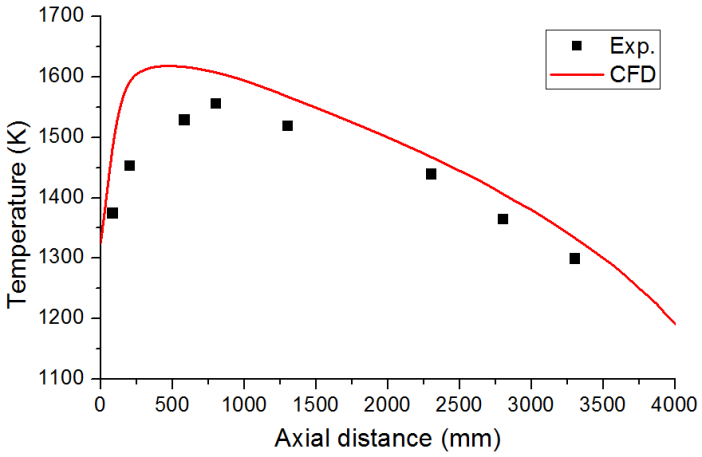

Figure 4.5 A plot of the temperatures along the centreline.

The predicted temperature profiles along the centreline of the furnace is compared to the experimental data in Figure 4.5. The biggest discrepancy between the CFD predictions and the experimental data is about 100 K near the burner where intensive swirl of the combustion gas exists. Further, as the axial distance increases, the CFD predictions and the experimental data are in good agreement.

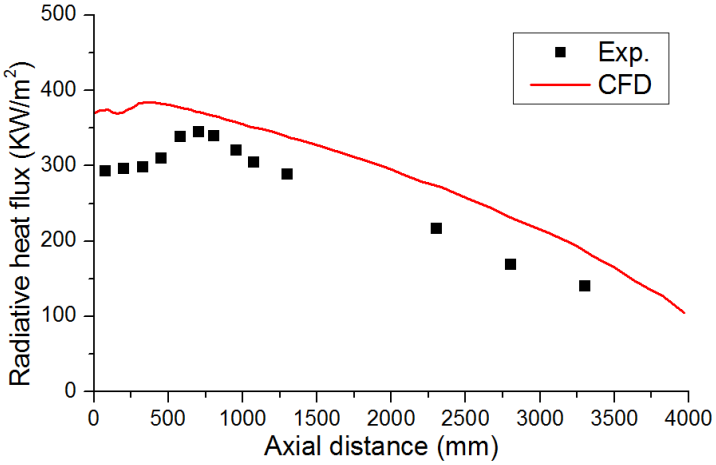

Figure 4.6 A plot of the surface incident radiation along the wall.

The surface incident radiation along the wall surface is also measured, thus the measuremental data is compared to the CFD predictions in Figure 4.6. It appears that the CFD models over predict the values of temperature and heat flux over the whole range along the axial distance and this may be a result of the assumptions used in the wall boundary conditions.

The possible reasons for the discrepancies in Figure 4.5 and Figure 4.6 are in two aspects: i) the measurement devices may not be 100% accurate as the devices that are inserted in the furnace would affect the original radiation

in the surrounding region; ii) there are some limitations in the CFD modelling as the current radiation model used is a grey model, while a non-grey model is believed to produce more accurate results, however, the computational requirements of a non-grey model are unacceptable. In addition, the turbulence model employed is a RANS model and RANS models are not as accurate as LES or DNS, however, the LES and DNS require much more computational resources. In many cases, it makes sense if the CFD simulation results have the almost same trends as the measurements even though there are some discrepancies.

4.1.3 Simulation results and reduced order models

The coal combustion facility has a maximum thermal input of 250 KW_{th} and a minimum of 150 kW_{th} (any thermal input lower than this may cause unstable flames in the furnace). Therefore, this section provides a set of simulation results which cover the full operational range of the coal combustion facility. In addition, these simulation results are used to generate a reduced order model which performs as the combustion facility in the process simulation of the whole system which includes the facility and an amine capture plant.

Before the simulations are performed, it needs to be identified how to arrange these simulation points in order to properly cover the full operational range of the coal combustion facility, otherwise the accuracy of the reduced order models may be affected. Normally, this procedure is regarded as the design of experiments (DOE) [151] for developing a reduced order model from the measurements or from more complicated models. For this air-coal combustion facility, the coal feed rate is considered as the most important parameter as it determines the thermal input to the furnace, the mass flow rate of the air and thus the whole combustion environment in the furnace. Therefore, the coal feed rate is the only variable that needs to be considered in the reduced order model and thus the coal feed rates for the 6 CFD simulations to be performed are made such that they vary uniformly between 17.5 kg/hr (150 kW_{th}) and 29.2 kg/hr (250 kW_{th}).

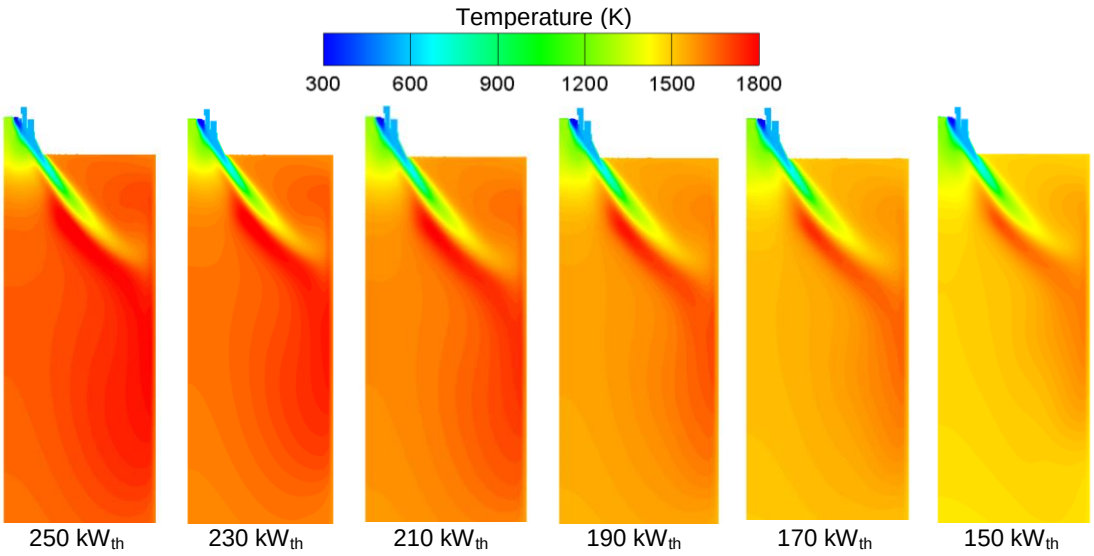

Figure 4.7 The predicted temperature profiles in the furnace with different thermal inputs.

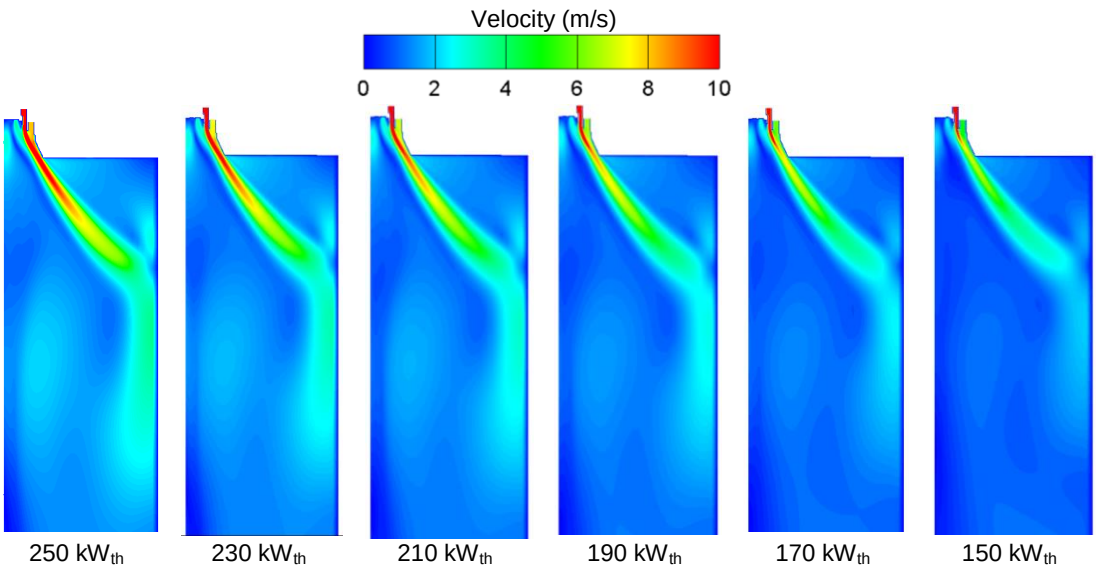

Figure 4.8 The predicted velocity profiles in the furnace with different thermal inputs.

	150 kW_{th}	170 kW_{th}	190 kW_{th}	210 kW_{th}	230 kW_{th}	250 kW_{th}
CO_2 (mass, %)	21.10	20.98	20.97	21.17	21.24	21.22
N_2 (mass, %)	71.09	71.12	71.11	71.06	71.04	71.04
O_2 (mass, %)	3.81	3.93	3.95	3.76	3.70	3.73
H_2O (mass, %)	4.00	3.97	3.97	4.01	402	4.01
Temperature (K)	1011.30	1048.10	1088.60	1128.40	1161.70	1189.80
Flow rate (kg/hr)	221.32	250.69	280.16	309.90	339.50	369.00

Table 4.2 The predicted outlet mass fractions, temperatures and the mass flow rates of the flue gas at different thermal inputs.

Figure 4.7 and Figure 4.8 show the predicted temperature and velocity profiles under different thermal inputs in the furnace and the results obtained clearly indicate that the temperature and the gas velocity decrease as the thermal input to the furnace decreases. Further, the flame shape is observed to shrink as the coal feed rate/thermal input decreases. Table 4.2 summarises the predicted mass fractions, gas temperatures and mass flow rates at the outlet of the furnace, which is then passed to the pilot scale amine capture plant. Since this chapter aims to test the applicability of the CFD and process co-simulation modelling technique on a pilot scale coal combustion facility combined with a CO_2 capture plant, the predicted gas mass fractions, temperatures and mass flow rates of the flue gas at the outlet of the furnace is used to generate a reduced order model which is able to represent the CFD furnace model in the whole system modelling. Table 4.2 reveals that the mass fractions of the components in the flue gas remains almost constant while the coal feed rate/thermal input varies and it should be noted that, the current model for the CO_2 absorption process in gCCS does not consider the effects introduced by the presence of O_2 in the flue gas and this could degrade the MEA solvent [152-154]. However, the degradation rate is much lower compared to that of the CO_2 absorption/desorption process [155] and thus the impact of O_2 is usually neglected when the modelling work only concentrates on the CO_2 absorption/desorption process [135, 156, 157]. Hence in this investigation the O_2 content in the flue gas is treated as N_2 and the mass fractions considered in the flue gas are averaged from Table 4.2 and presented in Table 4.3.

Components	Mass fractions
CO_2	0.21
N_2	0.75
H_2O	0.04

Table 4.3 The components and mass fractions assumed in the flue gas.

The predicted outlet gas temperatures and mass flow rates at different thermal inputs are plotted in Figure 4.9 and Figure 4.10, respectively. Further, a second order and a linear polynomial fitting are applied to these temperatures and mass flow rates, respectively, as functions of the thermal input to the furnace, so that the reduced order models for the gas

temperatures and mass flow rates at the outlet of the furnace are obtained as polynomial curves, see Figure 4.9 and Figure 4.10, respectively. The functions for the polynomial curves are also obtained and displayed in the Figure 4.9 and Figure 4.10, where x denotes the thermal input and y denotes the gas temperature or mass flow rate.

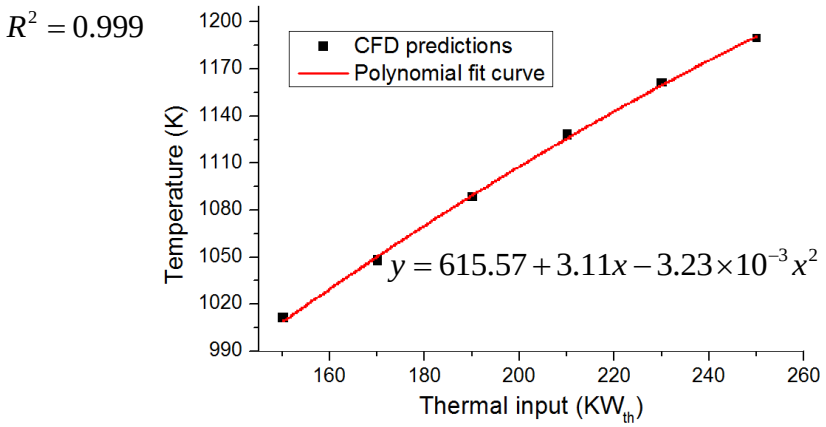

Figure 4.9 Temperature of the flue gas as a function of thermal input.

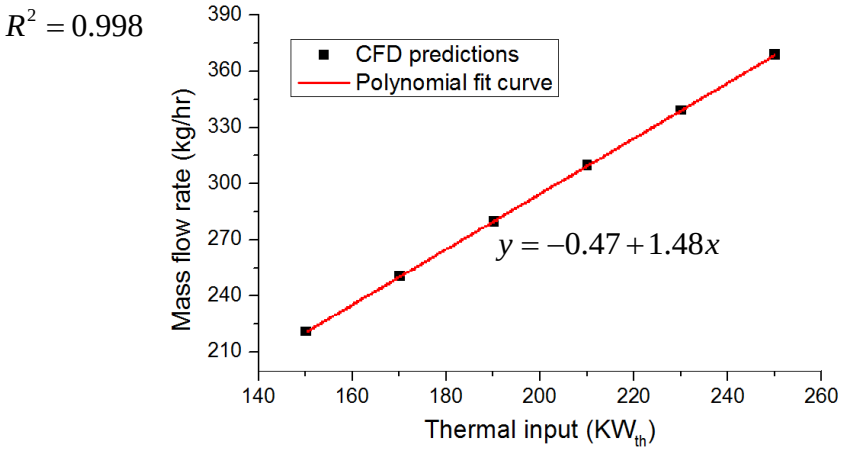

Figure 4.10 Mass flow rate of the flue gas as a function of thermal input.

4.2 Integrated CFD and process modelling of the PACT facility

4.2.1 The gCCS system modelling environment

gCCS is a newly commercialized tool by PSE for the simulation and design on the CCS systems. The model libraries in gCCS include that power plant library, CO_2 capture library, CO_2 compression and transportation libraries, etc. More importantly, the gCCS's flexibility allows the user to develop

foreign models to link to the gCCS developed process models. Thus gCCS is employed in this chapter to link the CFD based reduced order models, which account for the operation of the coal combustion facility, to the CO_2 capture plant model developed in gCCS.

The CO_2 capture model library in gCCS is developed for the solvent-based CO_2 capture process modelling and the library contains high-fidelity rate-based absorption-desorption column models and the auxiliary equipments, such as reboilers, condensers, flash drums and heat exchangers.

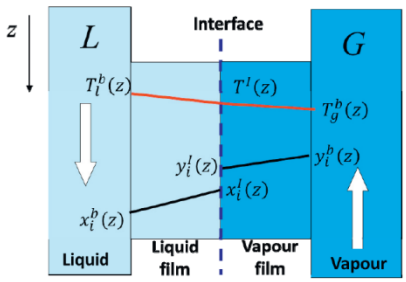

Figure 4.11 Schematic representation of the two-film theory [158].

The absorption-desorption column models are developed based on the two film theory [159], which is briefly described in Figure 4.11, where T is the temperature, z denotes the axial direction in the column, x and y are the mole fractions in the vapour and liquid phases, the superscripts b and I denote the bulk and interface, respectively, while the subscripts g and l denote the gas/vapour phase and liquid phase, respectively. The model applies a 1 D spatial discretization scheme along the axial direction of the column and the reactions are assumed to occur only in the liquid bulk and the phase and chemical equilibrium are assumed at the interface [158]. The mass transfer coefficients for both phases, pressure drop along the axial direction and the interfacial area have been considered in the model [158]. Moreover, gSAFT is a physical property package that has been integrated with gCCS and it employs a number of SAFT-based equations of state, including SAFT-VR [160] and SAFT-γ [161]. By assuming chemical equilibrium on the interface between the liquid and vapour films, the gSAFT model is able to describe the phase behaviour without explicitly treating the formation of new species [158]. However, detailed information on the mathematical equations describing the mass transfer, chemical kinetics,

phase equilibrium and thermodynamics in the model library is not available and this is due to the intellectual property issue.

4.2.2 Model validation

Before performing this investigation, an experimental plan had been arranged for the PACT pilot plant to provide validation data for this modelling work. However, the absorption column of the pilot plant has been under retrofit since the experimental plan was submitted. Therefore, it is necessary to acquire additional data from other pilot plant studies in order to assist in the validation of this modelling investigation. There are several plant studies that have been documented [162-167], however, most of these studies were either based on natural gas firing operations, where the mole fraction of the CO_2 in the flue gas is much lower compared to that from coal firing operations, or their scales are much larger than the PACT pilot plant. Therefore, the data obtained from the study [167], which was performed at the University of Texas at Austin, is suitable to be used in order to validate this investigation since the study [167] was also based on air-coal firing and the scales of the columns are comparatively similar to those used in the PACT plant.

4.2.2.1 Validation of the absorber model

The absorber column in the study [167] is a packed column which has a diameter of 0.427 m and a total packing height of 6.1 m. The column consists of two 3.05 m packing sections with a collector plate and redistributor between the beds. A random metal packing, with a specific area 145 m^2/m^3, was installed in the absorber column.

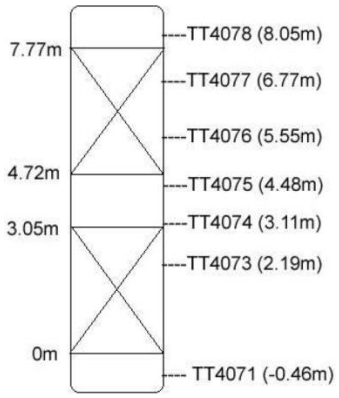

Figure 4.12 Absorber temperature measurement locations [167].

The column has seven temperature measurement ports installed along the height and Figure 4.12 shows the locations of these measurement ports in the absorber column. It should be noted that there is a measurement port below the packing bed and thus thus this measurement port has a negative value in height.

A number of tests had been performed in the study [167] and the tests 32 and 47 are taken to validate the models in this investigation. These two tests were selected because of their relatively high and low liquid to gas (L/G) mass flow rate ratios respectively. Moreover, these two tests were also used in the validations documented in [168], where the simulations were performed based on an advanced model library – gas/liquid contactor (GLC), which was used to develop the current CO_2 absorption/desorption models in gCCS, although some model equations may have been modified. The test conditions for the two cases are summarised in Table 4.4. It should be noted that the measurement of the mass flow rate of the flue gas entering to the absorber column was reported to be inaccurate [167], and therefore the mass flow rates were adjusted in [168] using an approach described in [169]. Considering this issue, this validation concentrates on whether the model can provide reasonable qualitative predictions of the pilot plant rather than the absolute values. In Table 4.4, the adjusted mass flow rates of the flue gas are in the brackets. Figure 4.13 provides a flow sheet of the absorber column generated in gCCS.

	Test 32		Test 47	
	Flue gas	Lean MEA	Flue gas	Lean MEA
Temperature (K)	319.7	313.8	332.2	313.3
Flow rate (kg/s)	(0.11)	0.72	(0.172)	0.642
L/G ratio	6.55		4.06	
Mass fractions				
CO_2	0.2520	0.0618	0.2415	0.0618
N_2	0.7332	0.0000	0.7392	0.0000
H_2O	0.0148	0.6334	0.0193	0.6334
MEA	0.0000	0.3048	0.0000	0.3048

Table 4.4 The test conditions of the absorber column in the tests 32 and 47. (The values in the brackets have been adjusted.)

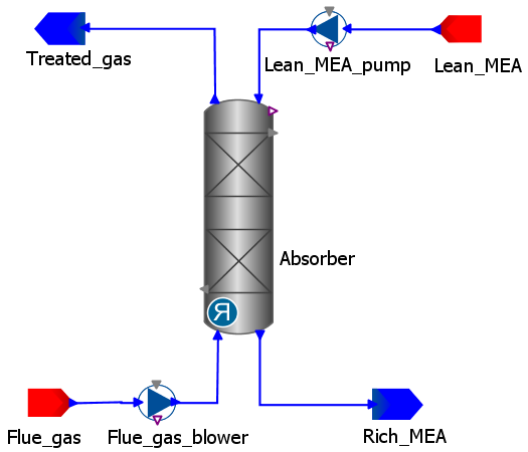

Figure 4.13 The flow sheet of the absorber column generated in gCCS.

(i) Validation results for the test 32

The predicted lean solvent loading, rich solvent loading and the CO_2 capture ratio are compared to the measurement data in Table 4.5 and these results are observed to be in good agreement with the measurement data. However, it should be noted that the measurement of the flue gas flow rate was reported to be inaccurate and the flue gas flow rate has been adjusted to 0.11 kg/s in the simulation, and thus there is a considerable discrepancy in the L/G ratio.

	Measurment	gCCS model
input		
Flue gas flow rate (kg/s)	0.13	(0.11)
L/G ratio (liquid kg/gas kg)	5.5	6.5
Lean solvent loading (mol CO_2/mol MEA)	0.279	0.279
output		
Rich solvent loading (mol CO_2/mol MEA)	0.428	0.439
CO2 capture ratio (%)	95.0	95.3

Table 4.5 The validation results for the test 32. (The values in the brackets have been adjusted.)

The predicted temperatures along the height of the column are compared to the measurements in Figure 4.14. The maximum temperature discrepancy between the gCCS predictions and measurement data in the whole range considered by the modelling is about 11 K. Due to the limited number of the measurement ports along the height, the actual trend in the temperature profile may not be fully measured, but the gCCS model appears to provide

satisfactory temperatures between the axial locations 2.5 m and 7.9 m compared to the measurement data.

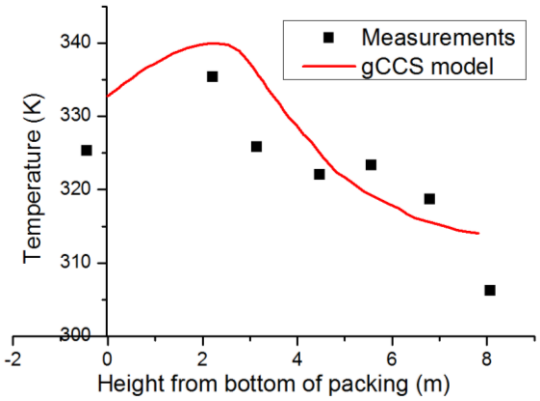

Figure 4.14 The predicted temperatures along the height of the column for the test 32.

(ii) Validation results for the test 47

The predicted lean solvent loading, rich solvent loading and the CO_2 capture ratio are compared to the measurement data in Table 4.6 and these results are found to be in good agreement with the measurement data. The predicted temperatures along the height of the column are compared to the measurement data in Figure 4.15, which indicates that the general trend predicted by gCCS matches well with measurements.

	Measurment	gCCS model
input		
Flue gas flow rate (kg/s)	0.158	(0.172)
L/G ratio (liquid kg/gas kg)	4.1	3.7
Lean solvent loading (mol CO_2/mol MEA)	0.281	0.281
output		
Rich solvent loading (mol CO_2/mol MEA)	0.539	0.520
CO2 capture ratio (%)	69.0	68.5

Table 4.6 The validation results for the test 47. (The values in the brackets have been adjusted.)

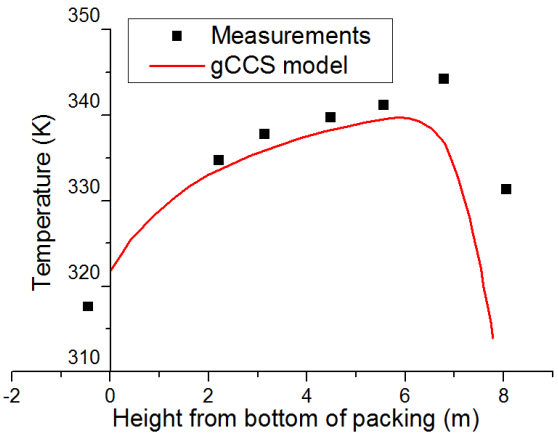

Figure 4.15 The predicted temperatures along the height of the column for the test 47.

4.2.2.2 Validation of the stripper column model

The stripper column used in the investigation [167] has the same configurations as the absorber column except that the packing employed was a structured packing with a specific area of 420 m^2/m^3. The test conditions for the stripper column are summarised in Table 4.7.

	Test 32	Test 47
Temperature (K)	358	356
Pressure (bar)	1.630	0.690
Feed flow (kg/s)	0.745	0.746
Condenser duty (W)	10000	134168
Reboiler duty (W)	152222	205000
Mass fractions		
CO_2	0.0971	0.0966
H_2O	0.6122	0.6085
MEA	0.2901	0.2943

Table 4.7 The input conditions of the stripper column in the tests 32 and 47.

It should be noted that the temperature, mass flow rate and compositions of the feed flow to the stripper column are obtained from the absorber model. A flow sheet for the stripper column is generated in gCCS and displayed in Figure 4.16. The rich MEA solvent is passed to the top of the stripper column while the lean solvent is produced from the reboiler, which is placed at the bottom of the column. A condenser is employed at the top of the column, where the MEA content is condensed from the CO_2 product and returned to the stripper column. In addition, the condenser and the reboiler duties in the

gCCS models are set to be the same as those test conditions described in Table 4.7.

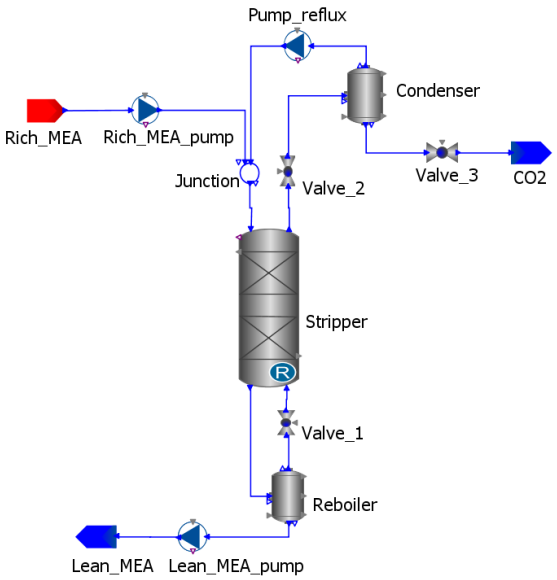

Figure 4.16 The flow sheet of the stripper column generated in gCCS.

(i) Validation results for the test 32

Temperature profiles obtained by the gCCS model for the test 32 are compared to the plant measurement data in Figure 4.17 and the temperature predictions appear to well represent the trend of the measurement data, although a significant discrepancy (about 15 K) is observed at the second measurement.

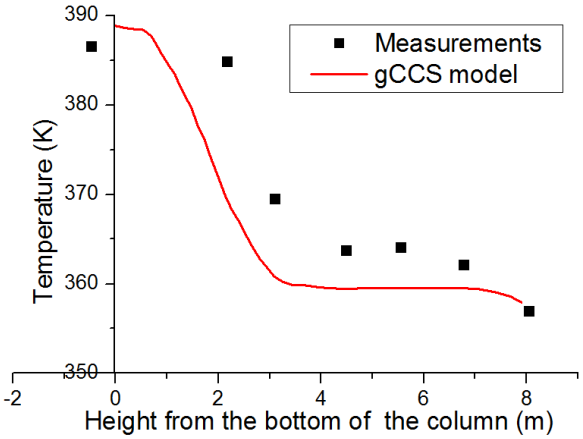

Figure 4.17 The predicted temperatures along the height of the column for the test 32.

(ii) Validation results for the test 47

Temperature profiles obtained by the gCCS model for the test 32 are compared to the plant measurement data in Figure 4.18 and it is observed

that the temperature predictions are found to be in good agreement with the measurement data. The temperatures in the test 47 appear to be generally lower than those in the test 32. The reason for this is that at the higher pressure in the test 32, a higher temperature is required to regenerate the solvent.

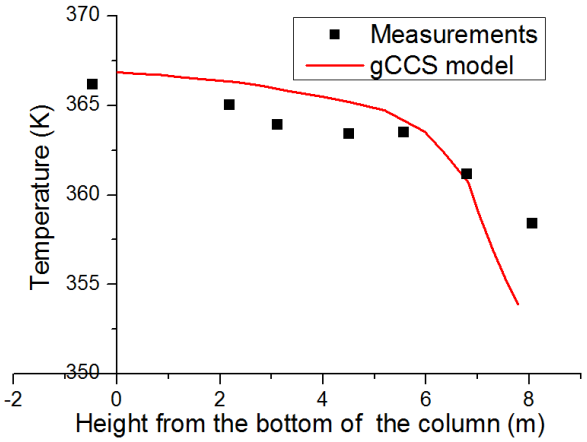

Figure 4.18 The predicted temperatures along the height of the column for the test 47.

4.2.2.3 Validation of the whole CO_2 capture process model

This section provides a brief validation for the whole CO_2 capture process model, and for this purpose, the absorber and the stripper models in the sections 4.2.2.1 and 4.2.2.2 are now integrated in order to simulate the whole CO_2 capture process. The flowsheet for the whole CO_2 capture process in gCCS is shown in Figure 4.19.

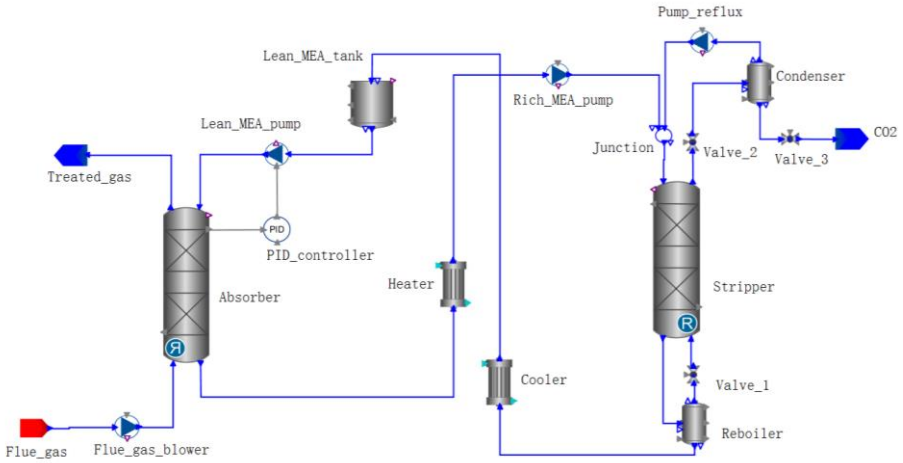

Figure 4.19 A flowsheet for the whole CO_2 capture process in gCCS.

It should be noted that the study performed at University of Texas [167] employed a heater to heat up the rich MEA solvent and a cooler to cool the

lean MEA, separately. A buffer tank was also used to store the lean MEA solvent. In this validation, a PID controller is employed to achieve the required CO_2 capture ratio, which is set to be 97% in this validation. The test case 32 is taken here to briefly validate the whole CO_2 capture process model.

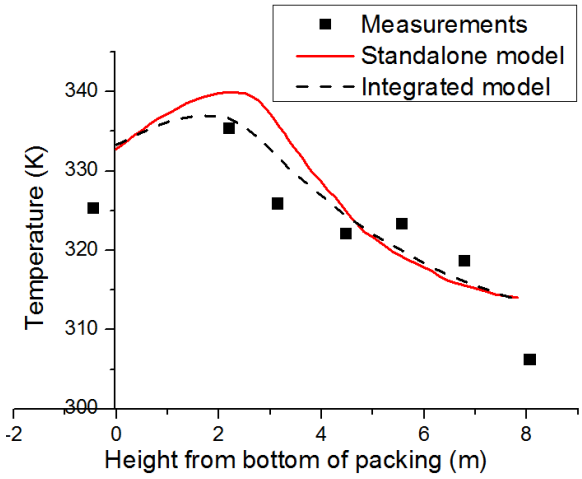

Figure 4.20 The predicted temperature profile in the absorber by the standalone and the integrated models for the test 32.

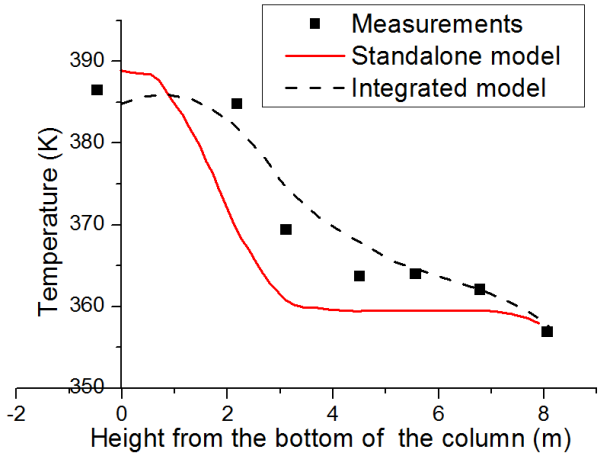

Figure 4.21 The predicted temperature profile in the stripper by the standalone and the integrated models for the test 32.

Figure 4.20 and Figure 4.21 present the predicted results for the absorber and the stripper from the integrated process in Figure 4.19. It should be noted that the input parameters for the validation are taken from those in the test 32. Further, Figure 4.20 and Figure 4.21 compare the predicted results with the measurements and it can be observed that the integrated model provides more accurate temperature predictions compared to the standalone models. This is because the standalone models do not consider the recycle

streams that link the absorber and the stripper, thus the interactions between the two columns cannot be reflected in the standalone results.

4.2.3 The integration of the reduced order models into the process modelling and model settings

In this section, a flowsheet for the process simulation of the PACT amine plant is generated using gCCS, which is shown in Figure 4.22. A number of components are employed in the plant and their names have been displayed. The direct contact cooler (DCC) cools the flue gas from the combustion facility with cool water. The typical gas temperature from the combustion facility is about 1100 K and has to be cooled down to about 315 K in the DCC before entering the absorber. It needs to be noted that in this process simulation model, the temperature, mass flow rate and mass fractions of the flue gas are calculated with the CFD reduced order models described in 4.1.3. The reduced order models for the temperature and the mass flow rate of the flue gas are obtained as functions of the thermal input to the combustion facility (see Figure 4.9 and Figure 4.10). According to the CFD predictions of the mass fractions of the flue gas, the mass fractions change little as the thermal input varies, thus the mass fractions are averaged and summarised in Table 4.3.

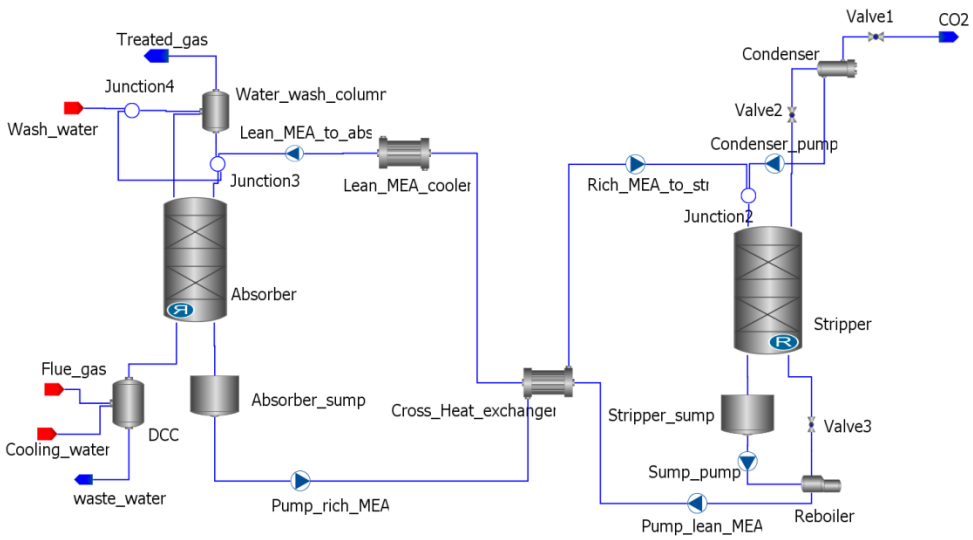

Figure 4.22 A flowsheet for the PACT amine plant generated in gCCS.

4.2.4 Simulation results of the PACT facility

With the developed integrated CFD and process model for the PACT pilot plant, a set of simulations are performed and the results are analysed in this

section. In order to fully cover the operational scenarios of the whole system, the thermal input to the coal combustion facility is allowed to vary from 150 kW_{th} (base load) to 250 kW_{th} (maximum load), therefore, the considered thermal inputs and the corresponding mass flow rate and the temperature of the flue gas are calculated from the CFD reduced order models and are summarised in Table 4.8. The MEA mass fraction of the lean solvent is assumed to vary from 30% to 40% and the considered fractions are 30%, 35% and 40%.

	Mass flow rate (kg/hr)	Temperature (K)
150 kW_{th}	221.5	1009.4
175 kW_{th}	258.5	1060.9
200 kW_{th}	295.4	1108.4
225 kW_{th}	332.4	1151.9
250 kW_{th}	369.3	1191.3

Table 4.8 The considered thermal inputs and the corresponding mass flow rate and temperature of the flue gas.

In these simulations, the mass flow rate of the lean MEA solvent entering the absorber is controlled in order to capture 90% of the CO_2 from the flue gas and the main results for different MEA mass fractions of the lean solvent are summarised in Table 4.9, Table 4.10 and Table 4.11. As the thermal input to the combustion facility increases, the mass flow rate of the flue gas increases, thus higher L/G ratios are required to achieve the same CO_2 capture ratio; the predictions on the CO_2 loading in the lean solvent vary little and have an average at about 0.195 while the CO_2 loading in the rich solvent decreases gently; the specific reboiler duty required by the condenser increases as more rich solvent is passed to the stripper column while the reboiler temperature is set to be the same.

As the mass fraction of MEA in the lean solvent rise from 30% to 40%, the L/G ratios are predicted to increase as a result of the increase in the CO_2 loading in the lean solvent; the CO_2 loading in the rich solvent shows a slight downward trend and the specific reboiler duty required by the condenser is reduced. However, high MEA mass fraction in the system may corrode the pipe lines.

Moreover, in each table, it can be seen that the same CO_2 capture ratio and almost the same CO_2 loading in the rich solvent can be maintained when the L/G ratio varies little, which means the operations of a CO_2 capture plant can be similar under a certain CO_2 capture ratio once the L/G ratio is set the same and this point was also suggested by Lawal et al.[132]. It needs to be noted that, the PACT CO_2 capture plant does not have a control device to adjust the L/G ratio but totally depends on manual interventions, however, this would be empirical, inaccurate and inefficient. Therefore, the implementation of system process simulation could assist the engineers to gain quantitative knowledge on the plant operation.

MEA mass fraction of the lean solvent: 30%				
	L/G ratio (kg/kg)	CO_2 lean loading (mol CO_2/mol MEA)	CO_2 rich loading	Specific reboiler duty (MJ/kg CO_2)
150 kW_{th}	3.247		0.462	6.178
175 kW_{th}	3.268		0.459	6.260
200 kW_{th}	3.288	0.195	0.457	6.336
225 kW_{th}	3.306		0.456	6.409
250 kW_{th}	3.323		0.454	6.477

Table 4.9 The simulation results of the PACT pilot plant with a MEA mass fraction of 30% and a CO_2 capture ratio of 90%.

MEA mass fraction of the lean solvent: 35%				
	L/G ratio (kg/kg)	CO_2 lean loading	CO_2 rich loading	Specific reboiler duty (MJ/kg CO_2)
150 kW_{th}	4.634		0.437	5.070
175 kW_{th}	4.688		0.435	5.123
200 kW_{th}	4.737	0.277	0.433	5.176
225 kW_{th}	4.782		0.432	5.223
250 kW_{th}	4.825		0.430	5.266

Table 4.10 The simulation results of the PACT pilot plant with a MEA mass fraction of 35% and a CO_2 capture ratio of 90%.

MEA mass fraction of the lean solvent: 40%				
	L/G ratio (kg/kg)	CO_2 lean loading	CO_2 rich loading	Specific reboiler duty (MJ/kg CO_2)
150 kW_{th}	6.053		0.433	4.911
175 kW_{th}	6.158		0.432	4.931
200 kW_{th}	6.208	0.326	0.431	4.963
225 kW_{th}	6.257		0.430	4.989
250 kW_{th}	6.328		0.429	5.023

Table 4.11 The simulation results of the PACT pilot plant with a MEA mass fraction of 40% a CO_2 capture ratio of 90%.

4.3 Summary

This chapter provides a preliminary knowledge on the integrated CFD and process co-simulation approach and it is tested on the PACT pilot plant, which involves a 250 kW_{th} coal combustion facility and a CO_2 capture plant. Specifically, the coal combustion facility is modelled using CFD techniques and validation has been made. Then the CFD models are used to simulate the operation of the combustion facility under different thermal input conditions. The flue gas from the combustion facility is then passed to the CO_2 capture plant, therefore, the accurate prediction of the properties (mass flow rate, compositions and temperature) of the flue gas is necessary and this is achieved by the reduced order models which are generated with the CFD simulations. Since only the thermal input (i.e. coal feed rate) is considered as the design variable of the reduced order models, a polynomial fitting is able to produce accurate reduced order models to represent the CFD techniques to predict the properties of the flue gas. It needs to be noted that, if more than one design variable needs to be considered, the simple approaches, such as polynomial fitting or interpolation, may not be able to generate sufficiently accurate reduced order models due to the highly non-linearity of the problem.

The operation of the PACT CO_2 capture plant is modelled using the process simulation technique. Since the experimental data for the PACT CO_2 capture plant is not available, some other data from a similar scale plant is employed

to validate the absorber model and the stripper model separately. The simulations are performed at different thermal input and MEA concentrations.

It should be noted that the integration of the CFD and the process simulation techniques can be achieved in different approaches, e.g. the CFD modelling techniques can be used to simulate the chemical absorption process inside the column so that the temperature, pressure and compositions profiles along the height of the column can be used in the process simulation models in the form of reduced order models. However, the CFD simulation of the absorber column is technically challenging since the mesh of the three dimensional random packing, the multiphase flow and the chemical reaction kinetics are difficult to be properly considered. Thus, these integration manners are not investigated in this thesis, although they are meaningful.

Chapter 5. Modelling and Simulation of a Large-scale Power Plant

In this chapter, the research objective is extended to an investigation of a large-scale power plant, namely the Didcot-A coal-firing power plant [147]. A CFD model for the utility boiler and the process models for the whole plant are introduced. The CFD simulations for the utility boiler of this power plant have been performed under both air-coal and oxy-coal firing conditions in order to investigate the differences between the two firing modes in terms of heat transfer characteristics. The process models for the power plant are represented by a set of fundamental equations which account for the mass balance, energy balance and physical properties. A general process simulator, gPROMS 3.6.0 [170], has been employed to integrate the process model components to simulate the Didcot-A power generation system under both air-coal and oxy-coal firing conditions. Essential model components for the whole plant system are described and their limitations for oxy-coal simulations are analysed. Then the air-coal results are compared to the available measurement data and RWE's in-house results. Also the simulation results under oxy-coal firing conditions are presented.

5.1 CFD modelling of the full-scale coal fired boiler

5.1.1 Model settings

The computational mesh covering the fluid region is generated using Gambit, which is a pre-processing software for CFD simulators. The mesh consists of about 4.1 million cells most of which are structured with a small number of polyhedral cells in the vicinity of the superheaters. The CFD boiler model covers the modelling of the boiler from the burner inlets up to the exit of the reheater FRH, see Figure 5.1, as used by the Didcot-A power plant. The dimensions and details of the boiler have been given in Chapter 3. Since the boiler structure is symmetrical, only half of the boiler is modelled. In addition, only 36 of the 48 burners were in operation, and therefore the other 12 burners are not considered in the CFD modelling.

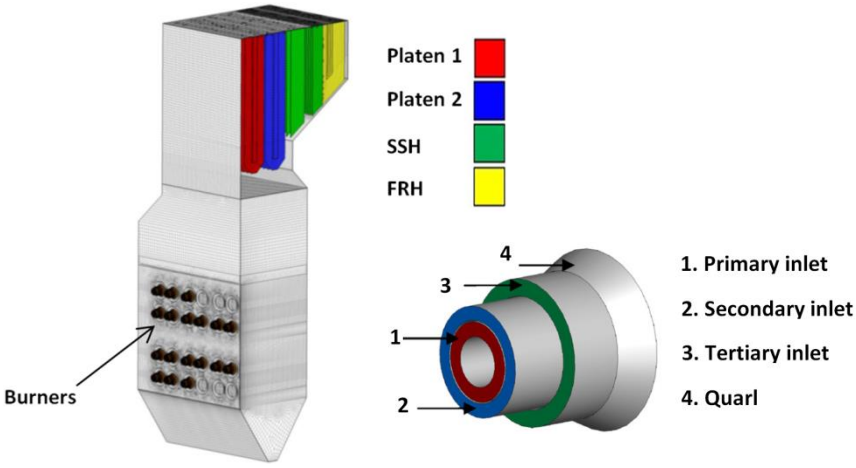

Figure 5.1 CFD mesh of the boiler (left) and its burner (right).

The coloured components in Figure 5.1 are the superheaters, namely platen 1, platen 2, the secondary superheater (SSH) and the final reheater (FRH). The walls of the superheaters are assumed to be very thin and an overall thermal conductivity is employed to account for the thickness of the walls.

The commercial CFD software ANSYS FLUENT 14.0 is employed to perform the CFD simulations and the sub-models are summarised Table 5.1. The fluid flow and combustion process is modelled using the Euler-Lagrange approach [171]. The governing equations for the conservations of mass, momentum, energy and species are solved [171]. The turbulence is modelled by the realizable $k-\varepsilon$ method, which has been successfully applied previously in many air-coal and oxy-coal combustion simulations [57, 142, 172, 173].

The approach used for modelling the combustion of the coal under air and oxy-fuel conditions has been documented in previous publications [53, 174]. In brief, the devolatilisation process is approximated by the single kinetic rate model [175] which assumes that the devolatilisation rate is determined by the temperature and the structure of the particle and the model parameters are taken from a previous publication [104] in which the combustion process of Pittsburgh 8 coal was investigated. The volatile combustion has been calculated using the Eddy Dissipation model with a two-step chemistry as outlined in Table 5.1. The char reaction is modelled with the intrinsic model for a global reaction order of unity and the reaction rate includes the effect of both the bulk diffusion and chemical reaction and the same model constants are employed as in the previous publication [104]. However, gasification

reactions were not included in this study, but it is important to note that it may have some effect on the overall char reactivity under oxy-coal combustion environment [176]. In addition, the effect of particles including soot particles on the radiation has been considered and the soot formation is modelled using the coal-derived Moss-Brookes model [175].

Sub-models	Model Description
turbulence	realizable $k-\varepsilon$
devolatilisation	single-step model [39]
volatile combustion	eddy dissipation model with two-step chemistry [53]
	$C_xH_yO_zN_k + aO_2 \rightarrow bCO_2 + cH_2O + dN_2$
	$CO + 0.5O_2 \rightarrow CO_2$
char combustion	intrinsic model [66, 67]
	$C + O_2 \rightarrow CO_2$
soot formation	coal-derived soot model [76]
radiation	discrete ordinates method [82]
	Absorption coefficients by WSGG [90]
	particle emissivity: 0.9 [31]
	particle scattering factor: 0.6 [31]

Table 5.1 Sub-models used in the CFD modelling of the boiler.

The discrete ordinates model (DOM) [82], has been chosen to account for the radiation. It is noted that the domain based weighted sum of grey gases model (WSGGM) [90] has been successfully applied in numerous CFD studies to calculate the gas absorption coefficient in air coal combustion system [55, 103, 174, 177]. However, the correlation employed may not be reliable for oxy-coal condition where high concentrations of strongly absorbing CO_2 and H_2O exist. Therefore, an extensive amount of work has been contributed to constructing new WSGGM correlations for oxy-fuel combustion [91, 92, 178, 179]. Based on the recommendation of [180], which evaluated a number of correlations in the literature, the values of Johansson [92] were chosen and implemented in this research via user defined functions (UDF) to calculate the gas absorption coefficients. The full spectrum correlated k-distributions (FSCK) model [95] that has recently developed by the authors' research group show significant potential to give more accurate predictions for oxy-fuel combustion compared to the original

WSGGM. However, at this stage the computational resources required by the FSCK model limit its application to the simulations of full scale industrial boilers.

For each CFD case performed in this chapter, 24 2.8 GHz Intel processors and about 36 GB of RAM from a high performance computer (HPC) were allocated, but it still required 16-24 h to obtain converged results.

It should be noted that there are different choices in the turbulent model and the scattering factor from those in Chapter 4 (see Table 4.1).

i) The CFD case in Chapter 4 employed the Reynolds Stress turbulent model while the CFD case in this Chapter employed the realizable $k-\varepsilon$ turbulent model. For the CFD case in Chapter 4, our research group had investigated the impacts of different turbulent models [143], however, there was little difference in the temperature predictions obtained by these two turbulent models. Hence, in the CFD case of Chapter 4, the choice of the turbulent model does not affect the heat transfer. Theoretically, the Reynolds Stress model could be better for swirling flows and the swirling of the flow in the Chapter 4's case is stronger than that in this Chapter, due to the size and configuration of the burner. For this reason, the Reynolds Stress model was employed in Chapter 4. As for the use of the realizable $k-\varepsilon$ turbulent model in this Chapter 5, this model has been successfully used in the CFD simulation of a large scale boiler in our previous publications [31, 56], where results having good agreement with measurements were produced.

ii) Different scattering factors are used, because the coal types used in the CFD simulations in Chapters 4 and 5 are different, and both of them are selected based on our previous publications [31, 56]. In addition, different scattering factors in Table 5.1 had been investigated before and it was found that the heat transfer values change little as the scattering factor varies from 0.1 to 0.9.

5.1.2 Coal data and boundary conditions

The fuel used in the power plant was a bituminous US coal, named Pittsburgh 8, and a coal analysis is provided in Table 5.2. In order to improve the coal combustion efficiency, the coal needs to be pulverized before transporting to the furnace. The pulverized coal particle size

distribution was obtained from a similar coal that was milled at Didcot-A [141] and the distribution data indicates that most particle diameters lie between 1 -300 μm with a mean at about 70 μm. In the CFD modelling, the coal particles are assumed to be spherical and their motion trajectories are tracked using the Eulerian-Lagrangian method.

Coal type: Pittsburgh 8			
Ultimate analysis (wt%)		Proximate analysis (wt%)	
Carbon	83.4	Fixed carbon	50.3
Hydrogen	5.5	Volatile matter	31.0
Nitrogen	1.6	Ash	10.3
Sulphur	2.6	Moisture	8.4
Oxygen	6.9	GCV (MJ/kg)	27.3

Table 5.2 Pittsburgh 8 coal analysis.

The operating parameters for the air and oxy-coal cases are shown in Table 5.3. Particularly, the air-coal case is set as a base case and these results will be compared to those of the oxy-coal cases and the operating parameters for the air-coal case are taken from the full load settings of the boiler described in [16]. For simplicity, each oxy-coal case in Table 5.3 is named by the molar concentration of O_2 carried by the oxidant gas that enters the boiler, for example, Oxy25 means the overall molar/volumetric concentration of O_2 entering the boiler via each burner is 25%.

	Air-coal	Oxy21	Oxy25	Oxy30	Oxy35
Coal feed rate (kg/s)	46.7	46.7	46.7	46.7	46.7
Thermal input (MWth)	1724.9	1724.9	1724.9	1724.9	1724.9
Oxidant gas feed rate (kg/s)	540.3	619.3	500.1	402.3	335.9
Recycle ratio (%)	0.0	76.2	71.0	64.8	58.8
Excess O_2 (vol%, dry)	5.0	5.0	5.0	5.0	5.0
Air leakage (kg/s)	16.0	16.0	16.0	16.0	16.0

Table 5.3 Operating parameters for the air and oxy-coal cases.

For consistency, the coal feed rates of all the oxy-coal cases are set to be the same as the air-coal case, which is 46.7 kg/s, and therefore, the thermal inputs to the boiler are the same (1724.9 MW_{th}). Generally, in order to fully burn the coal particles in the boiler, the O_2 level at the boiler exit is measured

to determine the feed rate of the oxidant gas and for this purpose the O_2 level at the exit is usually controlled to be 3-6% [181] in volume, based on a dry basis. Therefore, the excess O_2 concentration at the exit is set to be 5% in this investigation. Moreover, with both the excess O_2 concentration and the O_2 concentration of the oxidant gas provided, the mass flow rate of the oxidant gas and the recycle ratio of the flue gas can be obtained from a mass balance calculation. The air leakage into the boiler was assumed to be 16 kg/s and this was assumed to come through the ash hopper [57]. The flue gas recycle for the oxy-coal cases is on a wet basis based on the suggestion from a previous research [182]. Typically, the oxy-coal combustion requires the purity of the oxygen stream from an ASU to be no less than 95% by volume [183]. Therefore, the oxygen purity has been set as 95% (with 5% inert gases) and maintained the same for all the oxy-coal cases.

The heat exchange components of the boiler: water walls, platen 1, platen 2, SSH and FRH, which have been shown in Figure 5.1, are treated as thin walls and an overall wall resistivity is applied to represent the thickness of the metal walls and the slagging layer. The overall wall resistivity is chosen to be 330 W/(K $\cdot$ m^2), which has been used in our previous studies [56, 57]. Hence, the temperatures of the walls are considered to be the average steam temperatures inside the tubes, which is described in Table 5.4. These average steam temperatures are taken from the RWE's in-house data described in [16].

	Temperature (K)
Water walls	623
Platen 1	700
Platen 2	720
SSH	800
FRH	800

Table 5.4 Average steam temperatures in the tube banks.

	Air-coal	Oxy21	Oxy25	Oxy30	Oxy35
Mass flow rate (kg/s)					
Primary	2.9	3.4	2.8	2.2	1.9
Secondary	2.2	2.6	2.1	1.7	1.4
Tertiary	9.5	11.2	9.0	7.3	6.1
Temperature (K)					
Primary	363	363	363	363	363
Secondary	530	530	530	530	530
Tertiary	530	530	530	530	530
Oxygen concentration (mass %)					
Primary	23.2	19.1	19.1	19.1	19.1
Secondary	23.2	19.1	23.8	29.7	35.7
Tertiary	23.2	19.1	23.8	29.7	35.7

Table 5.5 Boundary conditions of the oxidant gas at each burner inlet.

The mass flow rate, temperature and oxygen concentration of the oxidant gas at each burner inlet for the air-coal and oxy-coal cases is provided in Table 5.5. The pulverized coal is injected into the boiler with carrying air (or oxidant gas) via the primary inlets and supplementary air is injected via the secondary and tertiary inlets. The mass flow split fractions for each burner are: 20% for the primary, 15% for the secondary and 65% for the tertiary. In addition, the primary air is preheated to a temperature of 363 K and the secondary and tertiary air is preheated to a temperature of 530 K. In the oxy-coal conditions, it should be noted that for the safety of the coal ignition, the oxygen concentrations in the primary inlets are controlled to be 23.2% by mass, which is the same as the oxygen mass fraction in air. Therefore, the oxygen concentrations need to be enhanced in the secondary and the tertiary inlets so that the overall oxygen concentrations of the oxidant gas from the burners can be increased to the required levels. Moreover, in the oxy-coal cases, the recycled flue gas is assumed to be taken after a particle removal device.

5.1.3 Air-coal results and validation

Before the CFD cases were finalized, a mesh independence check had been performed based on 3 sets of meshes, including: 3.2 million cells (coarse), 4.1 million cells (medium) and 4.8 million cells (fine). Predictions of the total heat transfer and the exit temperature were used as assessment criteria,

and since the medium and fine meshes produce similar results, the medium sized mesh was chosen for this investigation.

	Experiment	MOPEDS	CFD
Heat transfer (MW)			
Water walls	-	456	457
Platen 1	-	106	99
Platen 2	-	110	136
SSH	-	110	101
FRH	-	79	52
Total	-	861	846
Temperature (K)			
Furnace exit	1591	1656	1670
Platen 1 exit	-	1135	1208
Platen 2 exit	-	1282	1299
SSH exit	-	1173	1140
FRH exit	-	1054	1094

Table 5.6 Heat transfer from the in-house code and the prediction from CFD for the air-coal case in the full-scale utility boiler.

The air-coal CFD simulations are compared to the available experimental data (exit temperature) and simulation results from the RWE's in-house code MOPEDS for the Didcot-A power plant modelling, which is summarised in Table 5.6. Particularly, the heat transfer to the water walls and the superheaters and the predicted mass averaged temperatures after the superheaters are compared to the MOPEDS predictions and the available experimental data.

It can be seen from the table that the total heat transfer (861 MW) predicted by CFD is in good agreement with MOPEDS (841 MW). The CFD prediction of the furnace exit temperature of 1670 K is within 5% of the experimental measurement of 1591 K, and in close agreement with MOPEDS (1656 K). It should be noted that the MOPEDS in-house code was only built on a set of zero or one-dimensional equations, which may be the reason for the discrepancies compared to the three-dimensional CFD predictions.

5.1.4 Air-coal and oxy-coal results analysis

The CFD simulation results of the air-coal and the oxy-coal cases are discussed in this section. The gas temperature predictions for the air-coal and oxy-coal under air-coal and oxy-coal conditions are presented in Figure 5.2, where the mass averaged temperature of the plane at the furnace exit

(furnace throat) is marked in order to clearly show the temperature differences between the CFD cases. It is clear that the overall temperature inside the boiler increases as the oxygen concentration increases, and this is because it is believed that a higher oxygen concentration may lead to a higher adiabatic flame temperature.

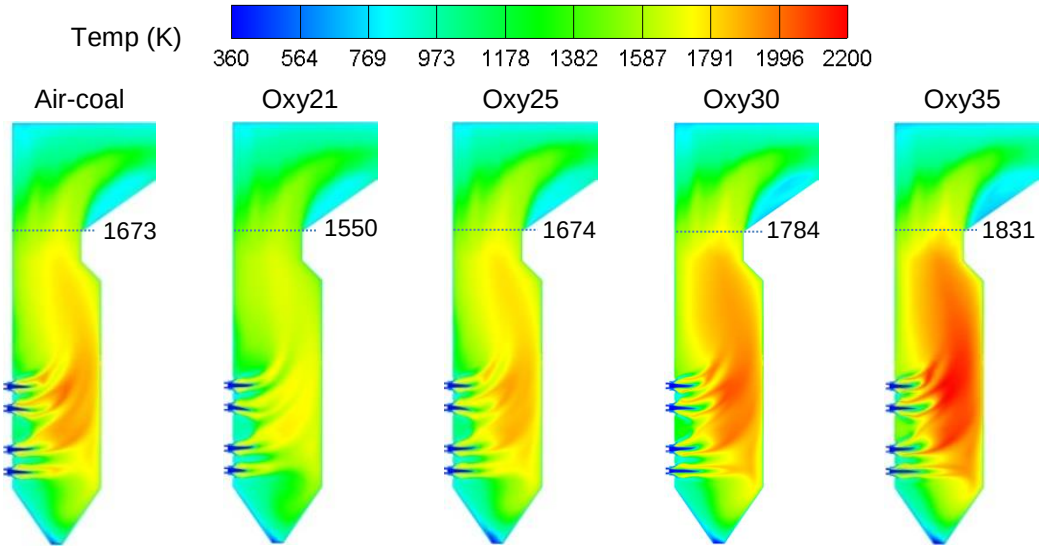

Figure 5.2 Predicted temperature contours inside the boiler under air-coal and oxy-coal conditions.

From Figure 5.2, in the Oxy21 case, the flame temperature is significantly lower than the air-coal case since the nitrogen has been replaced by the recycled flue gas (mainly CO_2) which has a higher heat capacity and thus the flame temperature may be lowered. An interesting phenomenon indicated by these temperature contours is that the temperature profile of the air-coal may be matched at some point between the Oxy25 and the Oxy30 cases.

Figure 5.3 shows the predicted velocity contours inside the boiler under air-coal and oxy-coal conditions. Since CO_2 has a much higher density than N_2, the replacement of N_2 by CO_2 in the Oxy21 case reduces the gas velocities inside the boiler. For instance, at a typical coal combustion temperature of 1800 K and in a normal atmosphere, the density of the pure CO_2 is about 300 kg/m^3 while the density of the pure N_2 is only about 190 kg/m^3. The gas velocities of the other oxy-coal cases (Oxy25, Oxy30 and Oxy35) are also lower than the air-coal case and this is because these oxy-coal cases have even less flue gas recycled. This change in the flow field may affect the

flame shapes in the combustion furnace, and consequently the heat transfer characteristics of the boiler may be disturbed.

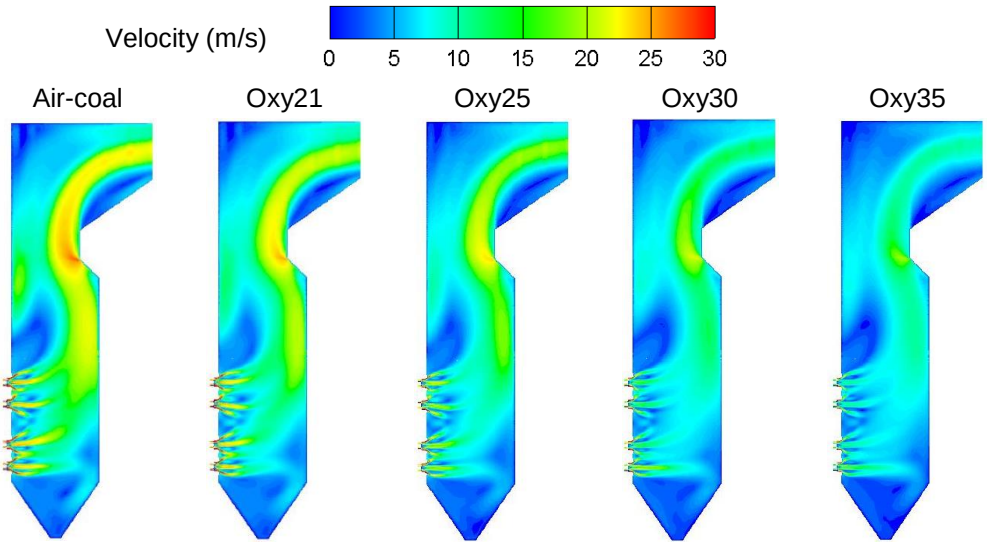

Figure 5.3 Predicted velocity contours inside the boiler under air-coal and oxy-coal conditions.

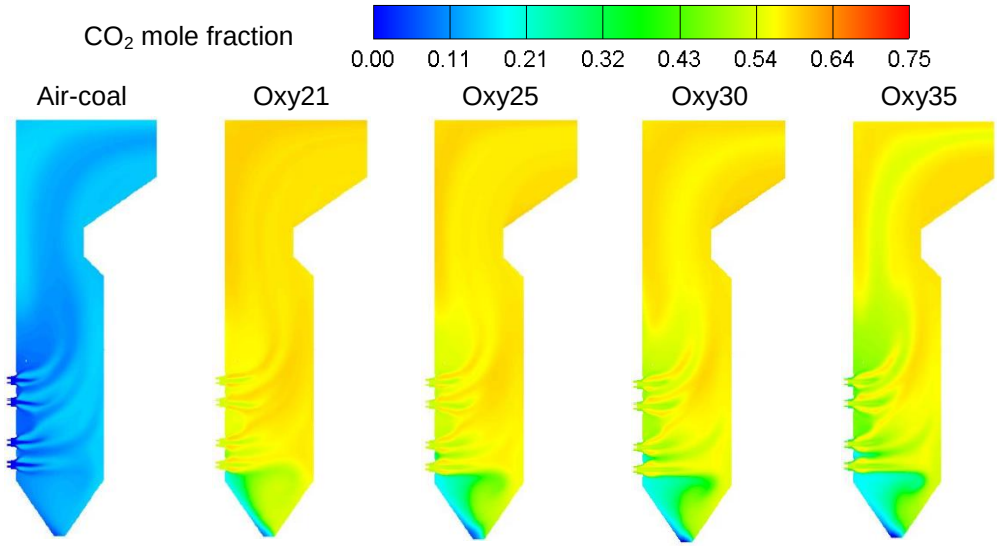

Figure 5.4 Predicted CO_2 mole fraction profiles inside the boiler under air-coal and oxy-coal conditions.

The predicted CO_2 contours inside the boiler for the air-coal and oxy-cases are presented in Figure 5.4. The CO_2 concentration of the air-coal case is much lower, compared to the oxy-coal cases, due to the existence of large amount of N_2 in the combustion gas. Also it can be observed that the CO_2 concentration increases as the oxygen enrichment increases and this is due to the fact that the amount of oxidant gas reduces as the oxygen

concentration increases. However, the coal feed rate is kept constant and this means the CO_2 generated from combustion is the same in each case.

The predicted oxygen mole fraction profiles for each case are show in Figure 5.5. The lowest oxygen mole fraction can be found in the air-coal and the Oxy21 cases. The differences in these profiles are the results of the different inlet oxygen concentrations described in Table 5.5.

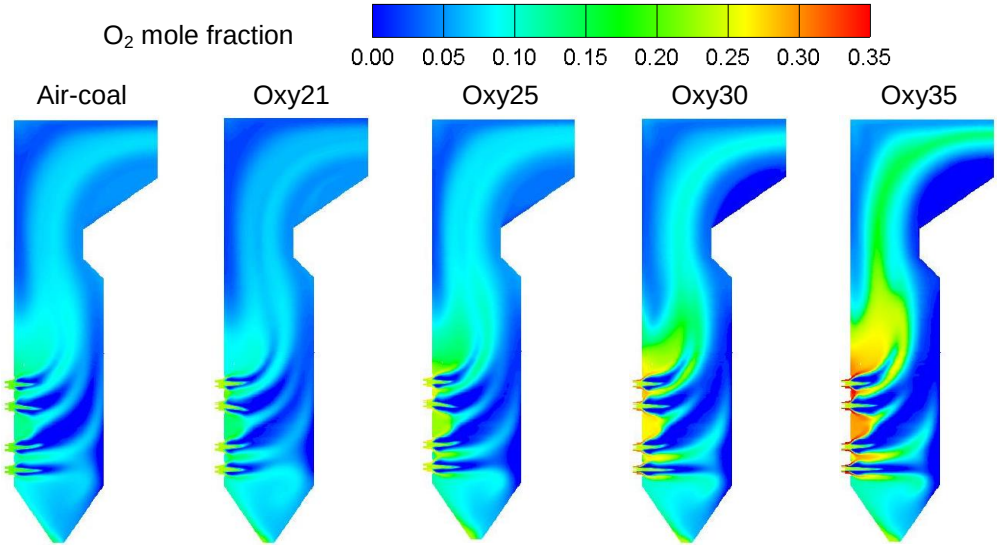

Figure 5.5 Predicted O_2 mole fraction profiles inside the boiler under air-coal and oxy-coal conditions.

A comparison in the predicted heat transfer between the air-coal and the oxy-coal cases is shown in Figure 5.6. It can be observed that the total heat transfer increases as the oxygen concentration increases from 21% to 35% and this is expected as a result of the increase in the flame temperature (see Figure 5.2). However, the change in the oxygen concentration on one hand affects the thermal properties of the combustion gas, such as the specific heat and radiation capability, and on the other hand impacts on the flow field in the furnace, such as the velocity profiles (see Figure 5.3), since the gas mass flow rate needs to vary accordingly. Also it should to be noted that the coal feed rate (thermal input) for each CFD case is kept the same. Therefore, a combination of the above aspects leads to different trends at different heat transfer components: (i) the heat transfer to the water walls, platen 1, platen 2 generally increases as the oxygen concentration increases; and (ii) the heat transfer to the SSH and FRH presents an increasing trend followed by a decreasing trend as oxygen concentration increases, this is mainly due to the change in the flow field.

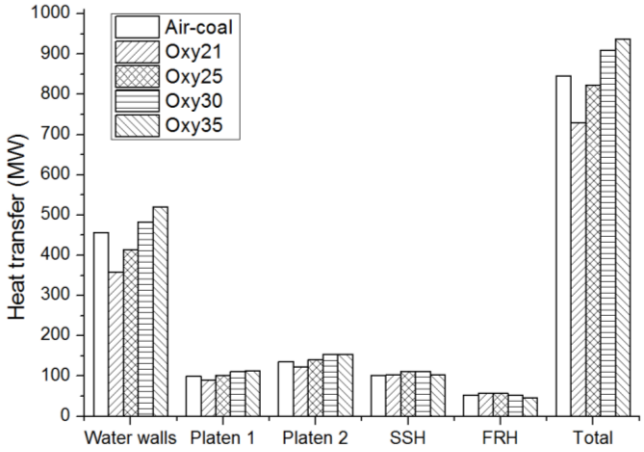

Figure 5.6 Predicted heat transfer to different components under air-coal and oxy-coal conditions.

5.1.5 Summary

The boiler is an important component in the power plant system, since it converts the chemical energy carried by the coal to the internal energy of the steam, which then drives the steam turbines and the power generators to produce electricity. Therefore, accurate modelling of the boiler is vital in the whole plant investigation under different operating conditions, such as air-coal and oxy-coal firing. In this section, the large-scale boiler (originally designed for air-coal firing) of the Didcot-A power plant is simulated using CFD techniques in order to investigate the differences between the air-coal and oxy-coal conditions.

The boiler was initially designed for air-coal firing and large deviation in the heat transfer is not benificial when using oxy-coal firing, otherwise the overall performance of the power plant may be disturbed. Under the same coal feed rate of 46.7 kg/s, the air-coal and oxy-coal CFD simulations suggest that the temperature and the heat transfer characteristics of the air-coal firing can be matched between 25% and 30% of the oxygen concentration when using oxy-coal firing and this is in line with previous investigations [56, 184].

5.2 The power plant simulations

A power plant contains a number of components other than the boiler and it is impractical to model all the components using CFD techniques, otherwise unacceptable computational resources are required. Therefore, in this section, a whole system process simulation model for the Didcot power plant

is described. The full plant model contains a set of sub-models and the important sub-models for the combustion furnace, natural circulation (including the steam drum and water walls), heat exchangers and steam turbines and in this chapter, the original power plant model is virtually extended in order to virtually account for the oxy-combustion operations of the power plant by adding an air separation unit (ASU) and a CO_2 purification unit (CPU) model in order to investigate the power plant under both air-coal and oxy-coal firing conditions. The air-coal results are compared to the MOPEDS data and then compared to the oxy-coal results.

5.2.1 Full plant description

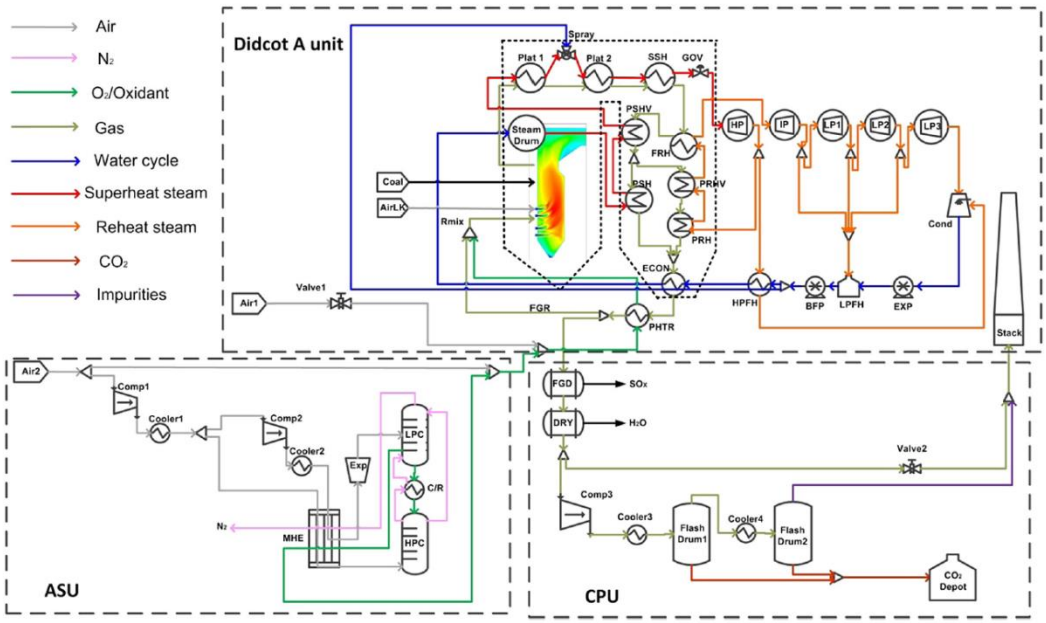

Figure 5.7 A flowsheet of the virtually extended Didcot-A power plant, including the original Didcot-A power generating unit, an air separation unit and a CO2 compression unit.

A detailed working processes of the Didcot-A power plant is provided in this section and Figure 5.7 shows a simplified layout of the extended Didcot-A power plant model, which includes the original Didcot-A plant, an ASU and a CPU and the material streams are defined as “Air”, “N_2”, “O_2/Oxidant”, “Gas”, “Water cycle”, “Superheat steam”, “Reheat steam”, “CO_2” and “impurities” according to the main materials contained in the stream. The main reason for defining specific material types is to clearly identify the different pipe lines and their usages. Several mixers and splitters are also used in the process. The main components in the flowsheet of Figure 5.7 are presented and briefly described in Table 5.7. In addition, a set of PI/PID controllers are

employed in order to assist the power plant to achieve the required operation status and these controllers are listed in Table 5.8.

Names of the components	Simple instructions
Air1, Air2, AirLK	Air1: air source for the furnace; Air2: air source for the air separation unit; AirLK: air source for the air leakage.
Comp	Compressor
Cooler	Used to cool down the inlet stream
Cond	Steam condenser
CO2 Depot	A temporary deposit tank for the captured CO2
C/R	Condenser and Reboiler
DRY	Flue gas drying
EXP, BFP	Pumps, pressurize the feeding water
Exp	Expander, expand the high pressure air
ECON	Economiser, preheat the feed water
Furnace	Furnace
FGD	Flue gas desulphurisation
FGR	Flue gas recycle loop
Flash Drum	Used to separate the impurities from the CO2 stream
GOV	Governor valve, control the steam mass flow rate into the high pressure steam turbine
HPC, LPC	HPC: high pressure column LPC: low pressure column
PHTR	Preheater, heating the inlet air or oxygen
Plat1, Plat2, SSH, FRH	Radiative superheaters Platen1, Platen2, SSH, FRH
PSHV, PSH, PRHV, PRH	Convective heat exchangers
HP, IP, LP1, LP2, LP3	Steam turbines, HP: high pressure, IP: intermediate pressure, LP: low pressure
MHE	Main heat exchanger for the air separation unit
Rmix	Recycle mix, mix the recycled flue gas with oxygen
Spray	Water spray, control the temperature of the steam goes into the Plat2
Steam Drum	Steam Drum, generating the high pressure steam
Stack	Exhaust the flue gas from air-coal firing or the impurities in the CO2 stream
Valve1, Valve2	Valve1: opens only when the boiler functions under the air-coal condition; Valve2: opens only when the CO2 stream is not pure enough for compression and purification

Table 5.7 Essential components and simple instructions for the full plant model.

PI/PID controllers used	Usage of the PI/PID controllers
Coal feed rate PI controller	The coal feed rate is adjusted so as to achieve the required pressure in the steam drum for the target power output.
Feed water rate PI controller	The mass flow rate of the feed water into the steam drum is controlled so as to maintain the required water level in the steam drum.
Governor valve PI controller	The open fraction of the valve is controlled so that the mass flow rate of the steam into the steam turbines, and thus the required power output, can be achieved.
Air1, Air2 mass flow rate PI controller	The oxygen concentration at the exit is measured. When the power plant functions under air-coal firing status, the mass flow rate from the Air1 that goes into the furnace is controlled. When the power plant functions under oxy-coal conditions, the source of Air1 is closed and the mass flow rate from the Air2 that goes into the ASU is controlled.
ASU bypass PID controller	The oxygen concentration in the oxygen product is measured, and from this measurement the fraction of inlet oxidant bypassing the ASU is adjusted.
HPC reboiler level PID controller	The liquid level in the reboiler of the high pressure column is measured. From this the mass flow rate of the liquid going out of the reboiler is controlled.
FGR PID controller	The oxygen concentration of the oxidant going into the furnace is measured. From this, the amount of the recycled flue gas is controlled and mixed with the inlet oxygen.
Water sprayer PID controller	The water sprayed into the steam between the Plat1 and the Plat2 is adjusted in order to control the temperature of the steam that goes into the Plat2.

Table 5.8 PI/PID controllers used in the full plant model.

In oxy-firing, an ASU is employed to generate oxygen, which is a typical double column design [185] and the oxygen purity can be adjusted between 95% and 98.5%. Typical oxy-coal combustion requires the purity of the oxygen stream to be no less than 95% by volume [186]. The oxygen purity has been set as 95% and maintained the same in the boiler CFD simulations. This oxygen stream is then mixed with a fraction of the recycled flue gas at a desired oxygen concentration before being transported to the furnace for the coal combustion. Here there is intensive heat transfer between the hot combustion products and water walls and the platen heat exchangers through radiation and convection. The hot flue gas then travels through the radiative superheaters, exchanging heat to the steam cycle. Due to the arrangement of the tube superheaters, a fraction of the flue gas may bypass the platen superheaters. After the first convective heat exchanger (PSHV),

the primary vertical superheater, the gas flow is split in the backpass between the superheat exchangers (Platen 1, Platen 2 and SSH) and the reheat exchangers (FRH), and then mixed before the economiser (ECON).The feedwater flow supplied by the economiser to the drum is required in order to match the steam generation. Water is circulated around the waterwalls, where it is heated and partially evaporated. The waterwall loop is a natural circulation system driven by the deferential density of the water. As a sub-critical system, the steam drum operates at a pressure of 178 bars for the full load (500MW_e) and 165 bars for part load (350MWe), and the steam generated from the drum is saturated. The required steam generation and the plant power output depends on the thermal input that is regulated by a PI controller.

The post processing of the flue gas involves an FGD unit, which removes SO_x, and a dryer, which removes moisture. Further, the purity of the CO2 stream for storage is required above 95% and therefore a CPU is required to purify the CO_2 stream. It should be noted that in this research we have not yet considered the possible issues of corrosion from the sulphur in the fuel. For a coal containing high level of sulphur, it would expect that the SO_2 concentration in the flue gas may be high enough to warrant SO_2 removal within the recycle loop to reduce the elevated risk of corrosion.

5.2.2 Model components for the power plant

It should be noted that the model components for the original Didcot-A air-coal firing power plant, which are described from Sections 5.2.2.3 to 5.2.2.7, were developed by RWE npower using a gPROMS platform based on the models reported by Bhambare [187], Hasan [188], Adam [189], Åström [190] and Sidders [191].

5.2.2.1 The distillation column model for the air separation unit

The requirements for an ASU for oxy-coal combustion in a commercial power plant are: (i) large size (normally above 280 ton/h for industrial-scale usage); (ii) relative low oxygen purity (in order to reduce the cost). Low oxygen purity means a volume concentration in the range of 95-98% compared to 99.5-99.6% produced from high purity units [192]. Currently, cryogenic distillation is the only commercially available technique to produce

O_2 economically for large scale applications, while other air separation technologies, such as pressure swing adsorption (PSA) [193], or polymeric membranes [194] are not yet mature or economical for large scale use. Therefore, the cryogenic distillation technology is employed in the present research, and the ASU is a classic double-column type [185] and a simplified flow sheet can be found in Figure 5.7. At first, the feed air is compressed from 1 bar to 6.4 bar by a 3-stage compressor (Comp1) with internal coolers. Then, the air is divided into two streams, namely high pressure air (HPA) and low pressure air (LPA, occupies about 19% of the total amount of the feed air). The HPA directly goes to the main heat exchanger (MHT) to recover the cold energy from the cryogenic products, while LPA is further compressed to 35 bar by a 2-stage compressor (Comp2) before entering the MHT. Afterwards, the LPA goes through an expander where its pressure drops to 1.1 bar and becomes partially liquefied before being injected into the upper part of the low pressure column (LPC). Meanwhile, the HPA is injected into the bottom of the high pressure column (HPC) where the HPA is preliminarily separated into pure nitrogen at the top and enriched oxygen (about 40% of purity) at the bottom. Then the enriched liquid oxygen enters to the middle part of the LPC for further purification. Finally, a relatively pure oxygen stream is pumped to the oxygen storage tank for the steam plant.

Some assumptions are made in the ASU model, namely (i) the air is clean and dry; (ii) the air only contains nitrogen, oxygen and argon while other trace compositions are neglected; (iii) the air compression and expansion processes are adiabatic.

The modelling of the cryogenic distillation process involves a set of equations accounting for the total mass balance (Eq.(5.1)), component mass balance (Eq.(5.2)), energy balance (Eq.(5.3)) and phase equilibrium (Eq.(5.4)) on each thermal stage (shown in Figure 5.8). It should be noted that the Peng-Robinson equation of state [195], which is already included in the Multiflash package for gPROMS, is employed to calculate the fugacity coefficients and the thermal properties on each stage and the binary interaction parameters are as given by Dodge and Dunbar [196, 197]. For simplicity, the following assumptions have been applied in the distillation model:

(i) The mixing between each component is ideal and perfect in both liquid and vapour phases.

(ii) The liquid and vapour phases reach equilibrium quickly on all thermal stages.

(iii) The heat loss via the column walls is neglected since it is quite small compared to the heat exchange in the condenser/reboiler.

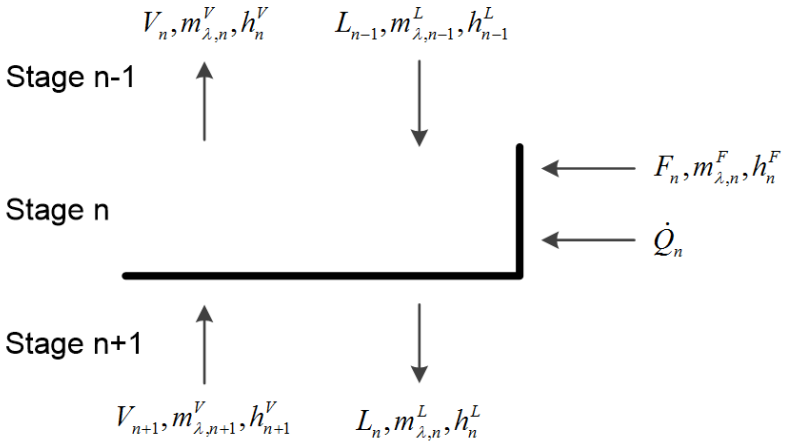

Figure 5.8 A simplified thermal stage of a distillation column.

By applying a balance analysis to a thermal stage of the distillation column shown in Figure 5.8, the equations (5.1), (5.2) and (5.3) can be obtained:

$$\frac{dM_n^L}{dt} = L_{n-1} + V_{n+1} - L_n - V_n + F_n \tag{5.1}$$

$$\frac{dm^L_{\lambda,n}}{dt} = \frac{1}{M_n^L}(L_{n-1}m^L_{\lambda,n-1} + V_{n+1}m^V_{\lambda,n+1} - L_n m^L_{\lambda,n} - V_n m^V_{\lambda,n} + F_n m^F_{\lambda,n} - m^L_{\lambda,n}\frac{dM_n^L}{dt}) \tag{5.2}$$

where L represents liquid flow rate, V stands for vapour flow rate, M^L is the transient mass of the liquid phase and F is the flow rate of the feed stream. $m^L_{\lambda,n}$ is the mass fraction of component λ in the liquid phase of stage n and $m^V_{\lambda,n}$ is the mass fraction of vapour of component λ. The number of the components is noted by N_λ and there are $N_\lambda - 1$ mass balance equations since the constraint $\sum_1^{N_\lambda} m^L_{\lambda,n} = 1$ must be satisfied.

The equation for energy balance can be written as:

$$\frac{du_n}{dt} = \frac{1}{M_n^L}(L_{n-1}h^L_{n-1} + V_{n+1}h^V_{n+1} - L_n h^L_n - V_n h^V_n + F_n h^F_n + \dot{Q}_n - u^L_n\frac{dM_n^L}{dt}) \tag{5.3}$$

where u is the mass specific internal energy of the mixture, h^L and h^V are the mass specific enthalpy of the liquid and vapour phase and $\dot{Q}_n$ is the heat flow into or out of the stage.

In addition, in order to close the whole system, the interaction between the vapour phase and the liquid phase must be addressed and therefore, the equation for the phase equilibrium in each stage is given as:

$$x^V_{\lambda,n}\phi^V_{\lambda,n} = x^L_{\lambda,n}\phi^L_{\lambda,n} \tag{5.4}$$

where $x^V_{\lambda,n}$ is the mole fraction of component λ in the vapour phase, $\phi^V_{\lambda,n}$ is the fugacity coefficient of component λ in the vapour phase while $x^L_{\lambda,n}$ and $\phi^L_{\lambda,n}$ account for the liquid phase.

The distillation column utilised in the present research is a thermal-coupled column which includes a high pressure column (HPC as the lower part) and a low pressure column (LPC as the upper part).

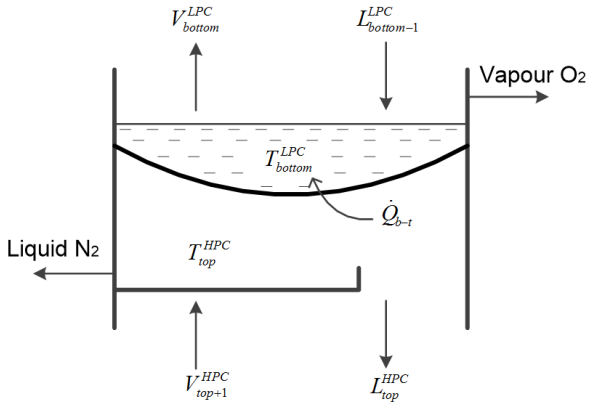

Figure 5.9 A simplified structure of the condenser/reboiler between the high pressure and the low pressure columns.

The HPC and the LPC are thermally integrated by a reboiler/condenser and its simplified structure is demonstrated in Figure 5.9, where the temperature difference between the HPC top and the LPC bottom is used in such a way that the heat released by the condensed nitrogen at the HPC top vaporises the liquid oxygen at the LPC bottom.

Some simple models representing such an integrated condenser-reboiler for cryogenic air separation plants have been documented by previous researchers [198, 199]. In general, the heat storage capacity of the heat

exchanger wall can be neglected, since it is small compared with the transferred heat flow($\dot{Q}_{b-t}$). The heat flow fed to the bottom of the LPC can then be obtained from the expression:

$$\dot{Q}_{b-t} = k \cdot A\left(T_{top}^{HPC} - T_{bottom}^{LPC}\right) \tag{5.5}$$

where T_{top}^{HPC} is the temperature at the HPC top, T_{bottom}^{LPC} is the temperature at the LPC bottom and $k \cdot A$ is the overall heat transfer coefficient.

5.2.2.2 The CO_2 compression unit model

Since the air leakage via the combustion furnace is unavoidable, and it is included in the model, the typical CO_2 molar fraction in the flue gas is in the typical range 70%-80% which is not yet sufficiently pure (at least 95% [186]) for liquefaction and storage. Therefore, a purification process is required to remove the impurities. This purification process is usually combined with the compression process so that a CO_2 compression unit is employed and a simplified flow sheet is presented in Figure 5.7. Before entering the CO_2 compression chain, the flue gas has passed through the flue gas desulfurization (FGD) and the flue gas condensation (FGC) so that the SO_2 and moisture have been removed. Then the flue gas is compressed to 30 bar by a multistage compressor with internal coolers. Following this, the flue gas is cooled down to a temperature 248.15 K by cooler 3 and become partially liquefied before going to the flash drum 1 where the vapour phase is separated and the liquid phase mainly contains CO_2. The vapour impurities from the flash drum 1 is then cooled down to 218.15 K in the cooler 4 and further separated in the flash drum 2. After these processes, the liquid, which mainly contains CO_2, is ready for storage.

In the CO_2 compression unit, the flash drum is the most important device since it plays a key role in the purification process. The flash drum can be regarded as a single stage of the distillation column, therefore the equations for the mass balance, energy balance and phase equilibrium are quite similar to those applied in the distillation column and therefore a repeat in describing the governing equations is not necessary.

Another important device, apart from the flash drum, is the gas compressor, which is also used in the air separation unit. The compression process is

assumed to be adiabatic and the work required to compress the gas is given by the following compression equation:

$$W = \int_{V_1}^{V_2} P dV \tag{5.6}$$

where V_1 is the volume flow rate before compression, V_2 is the volume flow rate after compression and P is the transient pressure of the gas.

With the adiabatic assumption, the polytonal correlation (Eq.(5.7)) can be applied to Eq.(5.6) and therefore the work required for a single compression stage can be represented by the following equations:

$$PV^{\gamma} = Constant \tag{5.7}$$

$$W = -\frac{1}{\gamma - 1} P_1 V_1 \left(\left(\frac{V_2}{V_1} \right)^{1-\gamma} - 1 \right) \tag{5.8}$$

where γ is the adiabatic index and is determined by $\gamma = (f+2)/f$, in which f is the number of degrees of freedom (3 for monatomic gas, 5 for diatomic gas and collinear molecules e.g. N_2, O_2 and CO_2).

5.2.2.3 The furnace model

The overall heat balance in the furnace is considered in Eq.(5.9):

$$(\dot{M}h)_{g,in} + (\dot{M}h)_{coal,in} + (\dot{M}Q_{NVC})_{coal,in} = (\dot{M}h)_{g,out} + (\dot{M}h)_{ash,out} + \dot{Q}_{evap} + \dot{Q}_{tfr} \tag{5.9}$$

where $(\dot{M}h)_{g,in}$ and $(\dot{M}h)_{coal,in}$ are the enthalpy flow rates of the oxidant gas and coal that enter the furnace, respectively. $(\dot{M}Q_{NVC})_{coal,in}$ is the overall combustion heat which is represented by the calorific value (Q_{NVC}) of the coal. $(\dot{M}h)_{g,out}$ and $(\dot{M}h)_{ash,out}$ are the enthalpy flow rates of the flue gas and the ash that leave the furnace, respectively. $\dot{Q}_{evap}$ is the heat transfer to the water wall that drives the steam generation and $\dot{Q}_{tfr}$ is the heat transfer to the superheaters that further heats the steam, which is generated from the water wall.

The mass specific enthalpies of the coal and the ash in Eq.(5.9) are calculated in Eq.(5.10) and Eq.(5.11), respectively.

$$h_{coal,in} = c_{p,coal}(T_{coal,in} - T_{ref}) \tag{5.10}$$

$$h_{ash,in} = c_{p,ash}(T_{out} - T_{ref}) \tag{5.11}$$

where $c_{p,coal}$ and $c_{p,ash}$ are the heat capacities of the coal and the ash, respectively and T_{ref} is a specified reference temperature.

Since the furnace combustion model is based on a fuel burn rate, and full combustion is assumed, the need for modelling the carbon content in the ash is avoided. The nitrogen and the sulphur content are assumed to convert to ash and sulphur dioxide, respectively. The adiabatic flame temperature (T_{ad}) in the furnace is determined by the heat released from the combustion. In addition, the heat transfer to the furnace walls and the superheaters via radiation is modelled in Eq.(5.13) and Eq.(5.14). Specifically, in order to account for the furnace heat transfer, an effective temperature (T_{eff}) is modelled as a weighted average of the adiabatic flame temperature and the gas temperature at the outlet (T_{out}) in Eq.(5.12), where two radiation heat transfer coefficients (β and $1-\beta$) representative of the geometry characteristic of the furnace are employed. In addition, the mass balance equation (Eq.(5.15)) is also solved.

$$T_{eff} = \beta T_{ad} + (1-\beta)T_{out} \tag{5.12}$$

$$\dot{Q}_{evap} = \kappa_{evap} \frac{V\sigma T_{eff}^4}{\rho} \tag{5.13}$$

$$\dot{Q}_{tfr} = \kappa_{tfr} \frac{V\sigma T_{eff}^4}{\rho} \tag{5.14}$$

$$\dot{M}_{out} = \dot{M}_{in} - V\frac{d\rho}{dt} \tag{5.15}$$

5.2.2.4 The natural circulation model

The natural circulation system of a boiler includes the steam drum and the water walls surrounding the boiler. The density differences in the water wall drives the natural circulation of the steam/water. The heat released from the coal combustion is transferred to the water walls, e.g. the downcomer and the riser surrounding the boiler. The mass flow rate $\dot{m}_{XR}$ of the water, leaving

the riser and going into the drum, is modelled as a function of the pressure drop in the riser as follows [16]:

$$\dot{m}_{XR} = K_{XR}\sqrt{(P_1 - P - g\rho_{XR}z)\rho_{XR}} \tag{5.16}$$

where K_{XR} is an empirical constant that relates the pressure drop in the riser to the water flow rate. P_1 and P are the pressure at the bottom and top of the riser, respectively, g is the gravity, ρ_{XR} is the density of the water and z is the height of the water wall.

The dynamic mass balance for the flow in the risers is described by:

$$\dot{m}_{WDC} - \dot{m}_{XR} = V_R \frac{d\rho_{XR}}{dt} \tag{5.17}$$

where $\dot{m}_{WDC}$ is the mass flow rate at the exit of the downcomer and V_R is the volume of the riser tubes.

The dynamic mass balance for the steam in the steam drum is given by:

$$\dot{m}_{XR}X_R - \dot{m}_S = (V_T - V_W)\frac{d\rho_S}{dt} \tag{5.18}$$

where $\dot{m}_S$ is the mass flow rate of the steam leaving the steam drum, V_T is the total volume of the steam drum, V_W is the volume occupied by the water in the steam drum and X_R is the mass fraction of the steam in the mixture at the riser exit.

The dynamic mass balance for the water in the steam drum is given by:

$$\frac{dM_W}{dt} = \dot{m}_f + \dot{m}_{XR}(1 - X_R) - \dot{m}_{WDC} \tag{5.19}$$

where M_W is the total mass of the water in the steam drum and $\dot{m}_f$ is the mass flow rate of the feeding water into the steam drum.

The dynamic enthalpy balance for the fluid in the riser is given by:

$$\dot{m}_{XR}(h_{WDC} - h_{XR}) + \dot{Q}_{XR} = V_R \frac{dh_{XR}}{dt} \tag{5.20}$$

where h_{WDC} and h_{XR} are the mass specific enthalpies of the mixture at the exit of the downcomer and the exit of the riser, respectively, $\dot{Q}_{XR}$ is the heat transfer rate to the water/steam inside the water wall. The total heat

transferred to the fluid in the risers is found from the tube wall heat balance in Eq.(5.21), assuming a mixed convection/radiation coefficient (κ_{XR}) between the water wall and the steam/water mixture inside the water wall.

$$(MC_P)_m \frac{dT_m}{dt} = \dot{Q}_{evap} - \dot{Q}_{XR}, \quad \dot{Q}_{XR} = \kappa_{XR}(T_m - T)^3 \tag{5.21}$$

where T_m is the average temperature of the water wall, T is the temperature of the steam/water mixture inside the water wall and $\dot{Q}_{evap}$ is the heat transfer from the combustion gas to the water wall that can be calculated from Eq.(5.13).

5.2.2.5 The radiative heat exchanger model

The radiative heat exchangers refer to the superheaters (platen 1, platen 2, SSH and FRH) in the furnace. In the radiative heat exchanger model, the steam directly receives heat from the enclosure metal walls, which contact with the combustion gas. Therefore, the heat transfer between the combustion gas and the tube walls must be addressed and the equation for this is given by Eq.(5.22) and this equation aims to describe the enthalpy change of the combustion gas.

$$(\rho V)_g \frac{dh_{g,out}}{dt} = -\left((\dot{M}h)_{g,out} - (\dot{M}h)_{g,in}\right) + \tilde{U}_g(T_w - T_{g,av}) - \dot{Q}_w \tag{5.22}$$

where $\dot{Q}_w$ is the radiative heat transferred to the metal wall from the surrounding combustion gas and is given by:

$$\dot{Q}_w = \kappa_w \frac{V\sigma T_{g,av}^4}{\rho} \tag{5.23}$$

The heat exchange between the steam and the surrounding metal wall is given by Eq.(5.24) and this equation aims to describe the temperature change of the metal wall of the heat exchangers.

$$(MC_P)_w \frac{dT_w}{dt} = \tilde{U}_s(T_{s,av} - T_w) + \tilde{U}_g(T_{g,av} - T_w) + \dot{Q}_t \tag{5.24}$$

where $\dot{Q}_t$ is the radiation from the furnace to the tube walls and is given by:

$$\dot{Q}_t = \lambda_i \dot{Q}_{tfr} \tag{5.25}$$

where $\dot{Q}_{tfr}$ is the total radiation from the furnace and has been defined in Eq.(5.14), λ_i is the split fraction of the total radiation for each superheater (i = platen 1, platen 2, SSH and FRH) and λ_i is defined by:

$$\sum \lambda_i = 1 \tag{5.26}$$

Finally, in order to describe the enthalpy change of the steam side, the heat transfer from the tube walls to the inside steam/water is given by:

$$(\rho V)_s \frac{dh_{s,out}}{dt} = -\left((\dot{M}h)_{s,out} - (\dot{M}h)_{s,in}\right) + \tilde{U}_s (T_w - T_{s,av}) \tag{5.27}$$

In the above equations, the coefficients $\tilde{U}_g$ and $\tilde{U}_s$ are the overall admittance factors steam-metal and gas-metal heat transfer respectively.

When the water/steam passes through the superheaters, the pressure drop due to friction is given by:

$$\Delta P = \frac{\ell}{\rho} \dot{M}^2 \tag{5.28}$$

where ℓ is the fictional loss constant based on measurements. The density ρ is assumed to be constant in all heat exchangers except in the water walls (surrounding the boiler) where the density variance inside the water walls drives the circulating flow. As for the pressure drop on the gas side, a similar formula to Eq.(5.28) is employed. Moreover, the pressure of the combustion gas is approximately 1 atm all the times and hence the thermal properties of the combustion gas are not significantly affected by the pressure variations but depend on the gas composition and temperature.

5.2.2.6 The convective heat exchanger model

It should be noted that once the flue gas passes out from the FRH, which is considered as the last radiative heat exchanger in the boiler, the gas temperature reduces significantly (to a typical value of about 1200 K) and radiation is no longer considered as the dominant form of heat transfer in the downstream heat exchangers (PSHV, PSH, PRHV, PRH and ECON).

The equations accounting for the convective heat exchangers are almost the same as those used in the radiative heat exchangers but it needs to be pointed out that the radiative terms, such as $\dot{Q}_w$ and $\dot{Q}_{tfr}$, are not modelled. Therefore, a repeat in introducing the heat transfer equations for the convective heat exchangers is not required.

5.2.2.7 The steam turbine model

3 steam turbines are used in the power plant, including a single-stage high pressure turbine, a single-stage intermediate pressure turbine and a 3-stage low pressure turbine. Each turbine stage is modelled as a single cylinder model. In order to account for different loading levels, Eq.(5.29) relates the expansion ratio with the mass flow rate of the high pressure steam and Eq.(5.30) describes the enthalpy loss due to the polytrophic expansion in the turbine.

$$\dot{M}_{in}^2 = b_1^2 \frac{P_{in}^2}{T_{in}} (1 - r^{\frac{\gamma+1}{\gamma}}) \tag{5.29}$$

$$h_{in} - h_{out} = b_2 T_{in} (1 - r^{\frac{\gamma-1}{\gamma}}) \tag{5.30}$$

The electrical power output by the turbine stage is calculated by Eq.(5.31). The model coefficients, namely b_1, b_2 and b_3, are the dimensional scaling coefficients.

$$\dot{Q}_{gen} = b_3 \dot{M}_i (h_i - h_o) \tag{5.31}$$

5.2.3 Air-coal firing results and validation

The full load air-coal firing results, obtained from the full plant model, are compared to the MOPEDS data which has been summarised in Chapter 3. The predicted temperatures of the steam and gas at the inlets and outlets are compared to the MOPEDS results in Table 5.9 and Table 5.10. A good agreement between the results obtained from the full plant model and MOPEDS can be observed from the comparison and the maximum difference is -6.3% in the gas temperature at the platen 2 inlet.

Temperatures (K)						
	Inlet			Outlet		
	This model	MOPEDS	Error, %	This model	MOPEDS	Error, %
Platen 1	653	654	-0.1	728	718	1.4
Platen 2	673	682	-1.3	764	752	1.6
SSH	764	752	1.6	841	841	0
FRH	766	736	4.1	832	841	-1.1
PSHV	643	648	-0.1	651	654	0
PSH	633	628	0.1	655	648	1.1
Econ	528	523	0.1	581	573	1.4
PRHV	717	694	3.0	766	736	4.1
PRH	630	638	-1.3	711	694	2.5

Table 5.9 A comparison in the temperature predictions on the steam side from MOPEDS and the full plant model for the heat exchangers.

Temperatures (K)						
	Inlet			Outlet		
	This model	MOPEDS	Error, %	This model	MOPEDS	Error, %
Platen 1	1650	1656	0	1182	1135	4.1
Platen 2	1350	1441	-6.3	1212	1282	-5.5
SSH	1283	1338	-4.1	1122	1173	-4.3
FRH	1122	1173	-4.3	1103	1054	4.6
PSHV	1103	1054	4.6	1066	1027	3.8
PSH	1066	1027	3.8	789	756	4.4
Econ	789	756	4.4	629	621	1.3
PRHV	1062	1027	3.4	962	923	4.2
PRH	961	923	4.1	801	769	4.2

Table 5.10 A comparison in the temperature predictions on the gas side from MOPEDS and the full plant model for the heat exchangers.

Figure 5.10 presents a comparison for the steam generation, drum pressure and steam temperature in the steam drum. Again, the results predicted by the two models are in good agreement with a maximum difference of about 1% in the steam generation.

	This model	MOPEDS
Steam generation (kg/s)	386	390
Drum pressure (bar)	178	178
Steam temperature (K)	629	628

Table 5.11 A comparison in the predictions of MOPEDS and the full plant model for the steam drum.

In Table 5.12, the predicted mass flow rate, pressure, temperature and power output in each turbine stage are compared to the MOPEDS results. It should be noted that the full plant model predicts a total power output of 500 MW, while MOPEDS gives 520 MW. This is because the MOPEDS model was developed when the power plant was relatively new but in fact the overall performance degrades with time. The degeneration in the performance was considered when building the power plant model in gPROMS. As for all the other predictions, these are, in general, in good agreement except that there is a maximum difference (12%) is found in the steam pressure at the LP2 outlet.

	Steam flow (kg/s)		Pressure (bar)		Temperature (K)		Power output (MW)
	inlet	outlet	inlet	outlet	inlet	outlet	
HP	425.8	327.9	160.1	39.6	834.2	623.3	157.0
	(422.1)	(330.1)	(161.0)	(42.1)	(839.0)	(638.0)	(149.0)
IP	327.9	327.9	38.7	6.2	819.3	579.4	160.0
	(330.1)	(328.6)	(40.4)	(6.5)	(814.0)	(585.0)	(169.0)
LP1	327.9	297.5	6.2	3.1	579.4	515.3	40.2
	(337.2)	(310.2)	(6.5)	(3.3)	(583.0)	(522.0)	(40.7)
LP2	297.5	295.1	3.1	0.7	515.3	391.1	72.2
	(310.2)	(291.3)	(3.3)	(0.8)	(522.0)	(399.0)	(72.5)
LP3	295.1	295.1	0.7	0.1	391.1	306.0	70.1
	(291.3)	(291.3)	(0.8)	(0.1)	(399.0)	(306.0)	(89.4)

Table 5.12 A comparison in the temperature and pressure predictions of MOPEDS and the full plant model for steam turbines (values in brackets are the MOPEDS results).

5.2.4 Air-coal and oxy-coal firing results analysis

Operating a traditional air-coal firing power plant under oxy-coal conditions may introduce several challenges. Firstly, the gas compositions in the boiler are changed drastically and this impacts on the absorption capability of the combustion gas, thus the temperature distribution in the boiler may be disturbed. Secondly, the change in the gas mass flow rate and the density will affect the velocity profile so that the flow field may be changed from the original air-coal firing condition. Thirdly, a combination of the above two factors will lead to a disturbance to the heat transfer to the water/steam and finally, the steam generation and the overall steam cycle may be affected.

In order to investigate how the oxy-coal operation of a conventional air-coal power plant would affect the overall performance, this section performs a set of oxy-coal simulations at the full load condition (500 MW power output) with the oxygen concentration varying from 21% to 35% and the oxy-coal results are compared to the air-coal results. The operating conditions for the air-coal and oxy-coal process simulations have been included in Table 5.13, where the recycle ratios of the flue gas, the excess oxygen concentrations at the boiler exit outlet, the oxidant gas flow rates entering the boiler and the total power outputs for the cases are shown. Afterwards, the predicted results for the heat transfer, steam generation and steam temperatures are compared.

	Air-coal	Oxy21	Oxy25	Oxy30	Oxy35
Recycle ratio (%)	0	75	70	63	57
Excess O_2 (vol%, dry)	5	5	5	5	5
Oxidant gas flow (kg/s)	557	571	476	391	333
Power output (MW)	500	500	500	500	500

Table 5.13 The operating conditions for the air-coal and oxy-coal cases.

5.2.4.1 A comparison on the predicted evaporative heat transfer and steam generation for the air-coal and oxy-coal cases

A key parameter that describes the output capacity of a coal-fired power plant is the generated steam mass flow rate, which is dictated by the heat transferred to the water walls, namely the evaporative heat. Under oxy-coal conditions, the original evaporative heat transfer at the air-coal firing status is changed.

The predicted evaporative heat transfer and steam generation rates from the steam drum for the air-coal and oxy-coal cases are presented in Figure 5.10 and Figure 5.11, respectively. In Figure 5.10, the evaporative heat is observed to increase as the oxygen concentration goes up, because the flame temperature in the combustion furnace increases when the oxygen concentration of the gas entering the boiler increases, thus the radiation to the surrounding water walls becomes more intensive.

The steam generation, see Figure 5.11, from the steam drum is the physical phenomenon of the evaporative heat transfer and therefore the steam generation from the drum also increases as the oxygen concentration

increases. The steam generation can be approximately matched to the air-coal firing within the oxygen concentration range of 25%-30% for the full operational range of the plant. It should be noted that the steam generated from the steam drum is not the total steam that enters the steam turbines. Apart from the steam that comes from the steam drum, a small amount of additional steam is introduced by the external water sprayed into the superheat steam at the inlet of superheater platen 2, in order to maintain an endurable wall temperature for the superheaters. If more water spray is required then less steam would be required from the steam drum. The total steam generated that enters the steam turbine is presented in Figure 5.12, and this indicates that the total steam generation can be matched with the air-coal case within the oxygen concentration range between 25% and 30%.

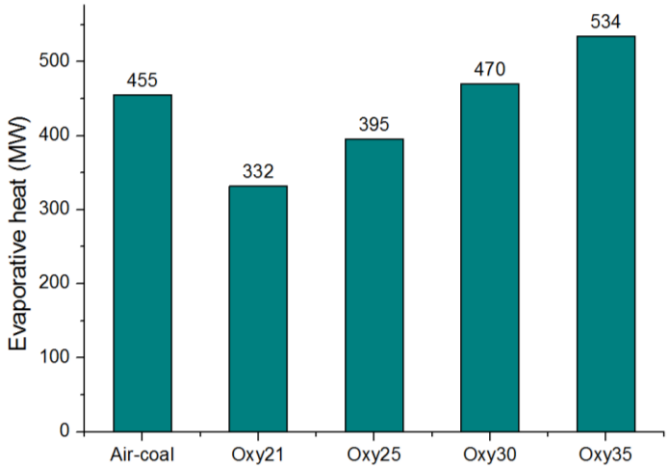

Figure 5.10 Predicted evaporative heat transfer for the air-coal and oxy-coal cases.

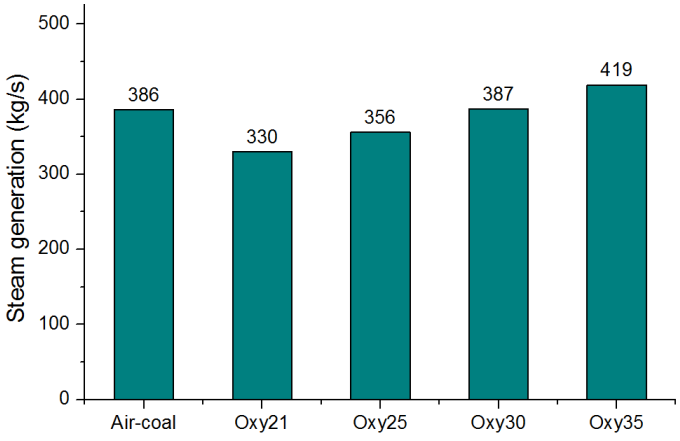

Figure 5.11 Predicted steam generation for the air-coal and oxy-coal cases.

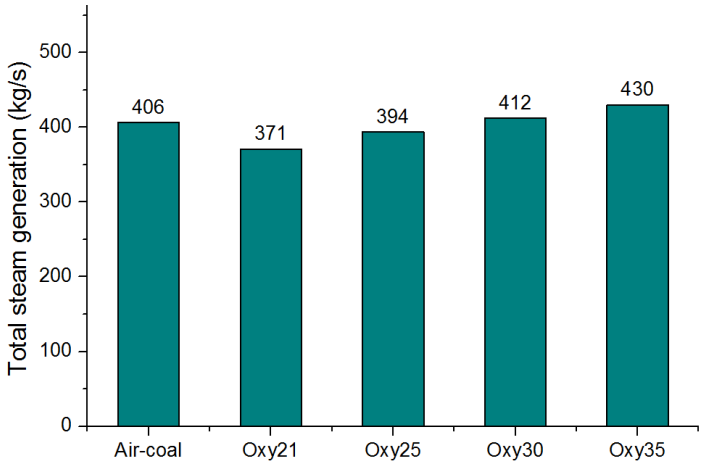

Figure 5.12 Predicted total steam generation for the air-coal and oxy-coal cases

5.2.4.2 A comparison on the predicted heat transfer inside and outside of the boiler for the air-coal and oxy-coal cases

In the furnace, where the combustion of coal takes place, the heat transfer to the water wall, platen superheaters and the reheater (platen 1, platen 2, SSH and FRH) is dominated by radiation. As the flue gas comes out from the furnace, the gas temperature is about 1100 K (for full load operation) or even lower, and the steam/water temperatures in the downstream heat exchangers (PSHV, PRHV, PRH, PSH and ECON are shown in Figure 5.7) vary from 600 to 800 K. Thus radiation is not considered as the dominant form of heat transfer and it by convection. Figure 5.13 presents the radiative heat transfer, while Figure 5.14 shows the convective heat transfer to the steam generation cycle. Clearly, the radiative heat dominates the process and it increases as the oxygen concentration increases while the opposite trend can be observed for the convective part of the heat transfer. As the oxygen concentration increases, the gas temperature increases so that the radiation is also strengthened. On the other hand, (i) as the oxygen concentration increases, the recycle ratio of the flue gas decreases, leading to a lower mass flow rate of the flue gas going through the convective heat exchangers; and (ii) as the oxygen concentration increases, the gas temperature leaving the final reheater (FRH), decreases since the total heat input to the furnace does not vary significantly in the simulated cases. These two factors cause a decrease in the internal heat carried by the flue gas that goes through the convective heat exchangers.

Further, it is clearly indicated by Figure 5.13 and Figure 5.14 that both the radiative and the convective heat transfer under oxy-coal conditions can be matched to those of the air-coal case within the oxygen concentration between 25% and 30%.

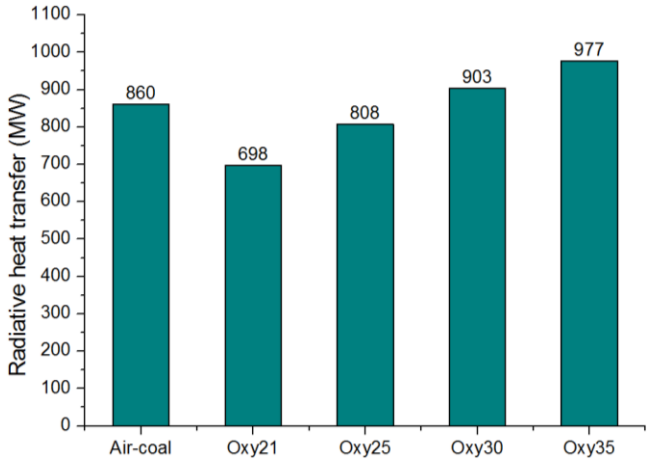

Figure 5.13 Predicted radiative heat transfer for the air-coal and oxy-coal cases.

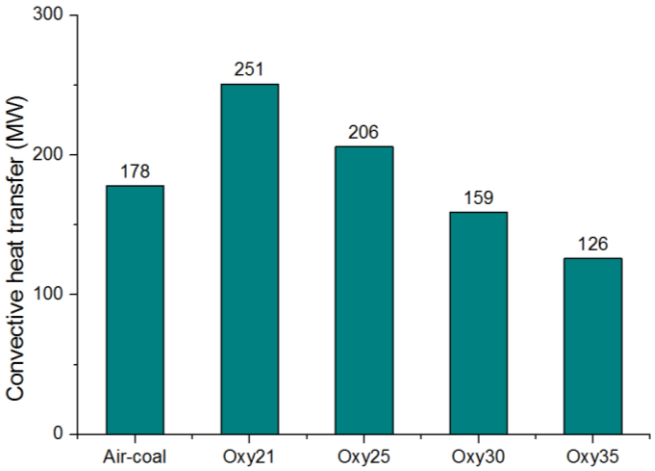

Figure 5.14 Predicted convective heat transfer for the air-coal and oxy-coal cases.

5.2.4.3 A comparison on the predicted steam temperatures for the air-coal and oxy-coal cases

Once steam comes out of the steam drum, the steam then sequentially passes through the PSH, PSHV, platen 1, water sprayer, platen 2 and SSH before entering the high pressure steam turbine. It is of interest to look into the steam temperature change along these heat exchange components on the steam side, therefore the predicted steam temperatures at the inlet/outlet of these elements are shown in Figure 5.15 in a sequential order that steam

goes through, and they are linked with straight lines in order to show the general trend of the temperature variations. At the inlet of PSH, which is connected to the outlet of the steam drum, the steam temperatures are predicted to be converged, because under the full load operating condition the pressure in the steam drum is kept constant at 178 bar and thus the saturation temperature of the steam is about 629 K. In general, the steam temperatures increase as the steam passes through PSH to SSH. Significant drops are observed in the water sprayer where some water is sprayed to the steam so that the downstream steam temperature would not become too high to protect the metal tubes, and this is achieved by a PI controller, to maintain the steam temperature at the outlet of the SSH to the control target of approximately 841 K. The steam temperatures in platen 2 and SSH are predicted to be very close for all cases investigated; while the biggest temperature differences are observed in PSHV, platen 1 and water sprayer.

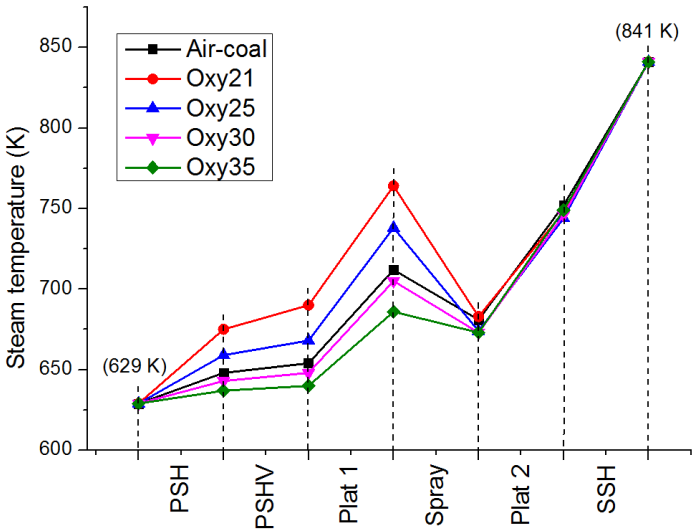

Figure 5.15 Predicted steam temperatures at the inlet/outlet of the heat exchangers.

5.3 Conclusions and limitations

In this chapter, the CFD modelling of the large scale boiler of the 500MW$_e$ Didcot-A power plant has been performed. Non-gray radiation models have not been employed due to the scale of the problem, since the computational cost required by a non-gray model is unacceptable in the modelling of a large scale utility boiler. In order to investigate the differences in the heat transfer characteristics under air-coal and oxy-coal operations, an air-coal

case and several oxy-cases (Oxy21, Oxy25, Oxy30 and Oxy35) have performed with a high performance computer (ARC 2) installed at the University of Leeds and 28 processors (each has 1.5 GB RAM) were allocated for each case but it still required more than 20 hours to obtain converged results. The CFD cases have been simulated under the full load condition and a comparison between the air-coal and the oxy-coal cases indicate that the temperature and heat transfer characteristics inside the boiler under the air-coal firing condition can be matched to the oxy-coal firing with between 25% and 30% oxygen concentration.

In the second part of this chapter, a process model that represents the Didcot-A power plant is described and this plant model has been virtually extended to oxy-coal combustion by adding an air separation unit model, a CO2 compression unit model and a flue gas recycle loop. Again, an air-coal and several oxy-coal full load cases (Oxy21, Oxy25, Oxy30 and Oxy35) have been simulated based on this full plant model. The oxy-coal results are then compared to the air-coal results and the comparison suggests that the steam generation and heat transfer to the water/steam cycle of the air-coal operation can be matched between 25% and 30% of oxygen concentration under oxy-coal operations.

However, this full plant process model contains several assumptions which may not be suitable for oxy-coal modelling and these limitations are listed as follows:

(i) The two model constants (κ_{evap} and κ_{tfr}) that account for the heat transfer in the furnace, are obtained by fitting to the RWE npower‘s MOPEDS data. Hence they are suitable for air-coal conditions only.

(ii) The split fractions λ_i (see Eq.(5.25) and Eq.(5.26)) that define the total radiation to each superheater, are fixed in this full plant model. However, these fractions may be different under oxy-coal firing conditions.

(iii) The furnace model is based on a set of zero-dimensional equations which may not be able to accurately model the effects on heat transfer brought by the geometrical configuration of the boiler and the superheaters.

(iv) The change in the oxidant gas flow rate entering the boiler may affect the flow field (which has an impact on the heat transfer profile) in the boiler. Hence the original model constants (κ_{evap} , κ_{tfr} and λ_i) must change accordingly.

Therefore, an integrated CFD-process simulation approach is developed in the following chapter in order to address these challenges.

Chapter 6. Evaluation of the Potential of Retrofitting a Coal Power Plant to Oxy-firing Using CFD and Process Co-Simulation

In this chapter, a new approach has been developed for estimating the potential of retrofitting an existing power plant to oxy-firing and determining the safe operation regime of the boiler under enriched oxy-combustion. A CFD technique has been employed to simulate the complex coal combustion and heat transfer to the boiler heat exchangers under air-firing and oxy-firing conditions. A set of reduced order models (ROMs) has been developed to link the CFD predictions to an efficient whole plant process model in order to simulate the performance of the power plant under different load and oxygen enrichment conditions if retrofitted to oxy-firing. The simulations of a 500MW_e power plant unit indicate that it is possible to retrofit to oxy-firing without affecting the overall performance of the unit. Similar heat transfer characteristics and steam generation can be achieved to those under air-firing.

6.1 Research background

Unlike the conventional air-firing process, oxy-combustion takes place in a mixture of O_2 and CO_2 or recycled flue gas. This produces a high concentration CO_2 (>85%) in the flue gas stream that is almost ready for compression and sequestration after purification. Because of the changes in the gas compositions in the furnace, the temperature and heat transfer characteristics of the boiler are different from those of air-firing. From the view point of the economics and safe operation of the plant, it is desirable that these changes do not deviate too much from the designed air-firing conditions after the retrofitting of an existing conventional power plant [200]. Whole plant process computer simulations are as a flexible and economic tool that has been widely employed in modelling power plant operation for both air and oxy-fired scenarios [201-203]. However, a major challenge for large scale whole plant process simulations lies in the difficulty of accurately modelling the combustion and thermal characteristics of the boiler where

complex fluid dynamics dominates and the heat transfer characteristics are strongly affected by the fundamental properties of the oxidant gas and boiler geometries. Based on the previous studies [141, 142, 172], in order to accurately predict the performance of a power plant, the heat transfer to the steam side inside the furnace must be accurately calculated both at the points with CFD simulations and those without. The steam generation, and the resulting heating, up are directly affected by the heat transfer to the heating surfaces. Computational Fluid Dynamics (CFD) is effective in the modelling of the details of the combustion process and can produce accurate representations of the temperature and heat transfer distributions in the combustion boiler and this has been extensively documented in the literature [34, 204-211]. However, CFD is not capable of modelling all components of a complex power plant efficiently and economically, in particular in an integrated manner. In order to take advantages of the efficiency of process modelling and the accuracy of the CFD modelling techniques, we have linked the CFD simulations to a power plant model of a 500 MW_e pulverised coal combustion boiler in our previous publications [142, 172], in addition to the attempts made by [212-214] for air-firing systems. In previous investigations, CFD and process modelling were directly linked in such a way that CFD simulations have to be performed at each of the operational conditions that are required in the plant process model. This approach is straightforward but requires a significant amount of time for the CFD calculations to cover a whole range of operational conditions of a power plant. In particular, this will become unacceptable when performing power plant dynamic simulation. In this research, in order to investigate the potential of retrofitting an existing power plant to oxy-firing and to predict the safe operational regime that matches the designed air-firing conditions and maintain high flexibility and efficiency, an efficient reduced order model (ROM) has been developed to combine the CFD simulations with the whole plant process simulations.

In this chapter, we have considered the Didcot-A coal fired power plant [147] to be retrofitted to oxy-firing, see Figure 5.7. The boiler has been modelled by a CFD approach while other components, such as the convective heat exchangers, steam turbines, air separation unit (ASU) and CO_2 purification

unit (CPU), are modelled by the process simulation models. Reduced order models (ROMs) for the heat transfer in the boiler have been developed based on a series of properly designed CFD simulations that accurately represent the thermal characteristics of the furnace in the integrated whole plant simulation. Finally, with the newly developed integrated full plant model, the range of oxygen concentrations at the boiler inlet for oxy-coal operation of the power plant is identified in order to match the heat transfer, the steam generation and the steam temperatures inside the superheaters to those of the designed air-coal firing conditions. For each CFD case, 24 2.8 GHz Intel processors from a high performance computer (HPC) were allocated, but it still required 16-24 h to obtain converged results. With the implementation of the fast CFD ROMs, the integrated CFD-process model can simulate an operation case of the whole plant within about 15 min using only one 2.2 GHz Intel processor from a laptop.

6.2 Essential component models for the co-simulation of the whole plant

As discussed in Section 6.1, in order to take advantages of the efficiency of the process modelling and the accuracy of the detailed CFD modelling, a co-simulation strategy has been employed. Thermodynamic calculation is an important method for boiler design. In the process modelling of a power plant, the heat transfer to the water wall and superheat components, as well as the steam temperatures of the heat transfer tube banks in the boiler, are usually calculated using empirical equations. For oxy-fuel combustion, there are no such empirical equations that may be employed with confidence. Therefore, CFD modelling with proper ROMs has been employed to address this problem. Thus it was decided that the commercial process simulation software gPROMS 3.6.0, combined with a CFD based ROM, should be employed for the whole power plant simulation. The heat transfer to the steam side inside the steam generation/superheat components of the boiler, up to the exit of the FRH, is simulated using a 3D CFD approach to generate the required ROMs to be incorporated in the plant simulation, and the rest of the steam cycle and other process units, such as the convective heat exchangers, columns, pumps, and compressors are modelled using process

models based on basic mass and energy balance equations. It should be noted that in this co-simulation work, the CFD models that account for the modelling the coal combustion and heat transfer processes inside the boiler have been described in Chapter 5.

The CFD based ROMs for oxy-coal combustion take the oxygen concentration and coal feed rate as dependent variables and these ROMs are created from the CFD simulations using the Kriging method [215], which cover different thermal inputs and oxygen concentrations. These fast ROMs account for the heat transfer to different radiant parts of the boiler, the gas temperature leaving the boiler and the maximum temperature on the metal wall of the boiler. In the full plant process model, the ROMs are used to drive the steam generation and superheating in the main radiative superheaters, the gas temperature leaving the boiler drives the downstream convective heat exchange process and the maximum temperature on the water wall provides reference for evaluating the boiler safety.

The heat transfer characteristics and steam generation are critical to the power plant. Models for the natural circulation, superheat exchangers and furnace are described in this section and these model equations are vital in the co-simulation, since in these model equations the CFD results are used to calculate the heat transfer values and gas temperatures. It should be noted that the natural circulation and the radiative heat exchanger models employed in this chapter are based on the model that has been described in Chapter 5, but some modifications have been made in order to efficiently incorporate the CFD ROMs.

As for the other models that account for the convective heat exchangers, steam turbines, distillation columns and CO_2 compression unit, they are the same as those described in Section 5.2.2, and therefore, a repeat of them are not necessary.

6.2.1 The natural circulation model

The model for the natural circulation employed in this section is almost the same as that has been described in Section 5.2.2.4. It should be noted that in this chapter the heat transfer ($\dot{Q}_{XR}$) to the water/steam inside the water wall in Eq.(5.20) will be calculated, based on the CFD modelling through the

reduced order model (ROM) developed in Section 6.3, as a function of the coal feed rate and the volume concentration of oxygen entering the boiler. Therefore, the Eq.(5.20) is updated in this section and can be written as the following equation:

$$\dot{m}_{XR}(h_{WDC} - h_{XR}) + \dot{Q}_{XR}(\dot{m}_{coal}, y_{ox}) = V_R \frac{dh_{XR}}{dt} \tag{6.1}$$

where $\dot{Q}_{XR}$ is a function of the coal feed rate $\dot{m}_{coal}$ and the volume concentration of oxygen y_{ox} that enter the boiler.

6.2.2 The radiative heat exchanger model

The radiative heat exchangers refer to the superheaters (platen 1, platen 2, SSH and FRH) in the furnace. A single model is employed for the heat transfer to the steam side of the superheaters platen 1, platen 2, SSH and the reheater FRH. It should be noted that a fraction of the combustion gas in fact bypasses platen 1 and platen 2 and this can be easily understood by investigating the layout of the hanging superheaters shown in Figure 5.1 and since the bypass fractions are difficult to obtain, the gas side is not modelled. The heat transfer from the gas side to the steam side is calculated by the CFD ROMs.

The dynamic mass balance for the steam side is given by:

$$\dot{m}_{s,in} - \dot{m}_{s,out} = V_s \frac{d\rho_s}{dt} \tag{6.2}$$

where $\dot{m}_{s,in}$ and $\dot{m}_{s,out}$ are the mass flow rates of the steam at the inlets and the outlets of the superheaters, respectively, V_s is the volume occupied by the steam in the superheater tubes and ρ_s is the steam density.

The pressure loss of the fluid passing through the relevant exchanger is calculated as follows:

$$P_{s,in} - P_{s,out} = \frac{\ell}{\rho_s} \dot{m}_s^2 \tag{6.3}$$

where ℓ is a modified friction factor and is equivalent to the product of the Darcy-Weisbach frictional factor divided by the square of the cross-sectional area of the heat exchanger pipes.

The dynamic enthalpy balance for the fluid through the exchanges is given by:

$$\rho_s V_s \frac{dh_{av}}{dt} = \dot{m}_{s,in} h_{s,in} - \dot{m}_{s,out} h_{s,out} + \dot{Q}_s(\dot{m}_{coal}, y_{ox}) \tag{6.4}$$

where h_{av} is the average mass specific enthalpy of the steam and is estimated by the average temperature of the inlet and the outlet steam, $h_{s,in}$ and $h_{s,out}$ are the mass specific enthalpies of the steam at the inlets and the outlets, respectively, $\dot{Q}_s$ is the heat transfer to the steam in the hanging tubes and is calculated, based on the CFD modelling through the reduced order model (ROM) developed in Section 6.3, as a function of the coal feed rate $\dot{m}_{coal}$ and the volume concentration of oxygen y_{ox} entering the boiler.

6.2.3 The furnace model

Since the heat transfer to the water walls and superheaters in the combustion furnace have been covered by the CFD based ROM, then empirical equations [141] for coal combustion and heat release are not necessary. Therefore the furnace model only accounts for the mass balance, the outlet temperature and the peak temperature of the metal wall. The mass balance in the furnace is described as follows:

$$\omega_{air}\dot{m}_{airlk} + \omega_{ox}\dot{m}_{ox} + \omega_{coal}\dot{m}_{coal} = \omega_{gas}\dot{m}_{gas} + \omega_{ash}\dot{m}_{ash} \tag{6.5}$$

where ω is the mass fraction of the relevant species, $\dot{m}_{airlk}$ is the mass flow rate of the air leakage into the furnace and a value of 16kg/s is employed, which is the same as that in the CFD simulations. When the system operates in the air-coal mode, $\dot{m}_{ox}$ is the mass flow rate of the feed air; when the system operates in the oxy-coal mode, $\dot{m}_{ox}$ is the mass flow rate of the oxidant consisting of oxygen and recycled flue gas.

Further, the gas temperature $T_{gas}(\dot{m}_{coal}, y_{ox})$ at the outlet of the furnace (immediately after the FRH) and the maximum temperature on the metal wall $T_{\max}(\dot{m}_{coal}, y_{ox})$ are directly calculated by the ROM which is described in Section 6.3.

6.3 The ROM development

In order to determine the feasible operating conditions of the “retrofitted” Didcot-A power unit, and in particular to determine the safe operation regime of the plant under retrofitted oxy-firing conditions, numerous plant performances have to be simulated with the whole plant model discussed in Section 6.2 at different operating conditions in order to cover the whole range of possible scenarios of the power plant. Each of these simulated conditions requires a CFD simulation and this will be prohibitively expensive. In fact it is impossible to obtain exhaustive values of data at every desired point due to the extensive computational cost required by each CFD case. Therefore the development of a reduced order model based on the advanced interpolation of a limited number of CFD simulations is desired which can be integrated into the full plant process simulations. A simple solution to link the CFD predictions, such as the heat transfer, to the process modelling is to use a linear interpolation. However, the heat transfer in the boiler is highly nonlinear with respect to the coal feed rate and/or oxygen concentration. Lang et al. [216] employed a principal component analysis (PCA) with a neural network mapping technique to develop the ROMs to interpolate the flow field inside a gasifier and results with a satisfactory fidelity were obtained. However, this approach is quite complicated in its mathematical form. Kriging is a response surface method for spatial data interpolation and is widely used in the areas of geology and aerology research [217-220]. Kriging uses spatial relationships of known points and their distribution to predict an unknown point, and it is a statistical, unbiased, and minimum variance predictor in which errors can be determined at specified points. This results in the non-linear characteristics of the data being preserved and therefore in this thesis, the Kriging method is employed to build the ROMs.

6.3.1 Kriging interpolation

Detailed introductions to the Kriging interpolation procedure can be found in many existing publications [217-220]. In the application of the Kriging interpolation to this study, $Y(x)$ is the interested response (i.e. the heat transfer, exit temperature) at an unknown point x and x is taken as the

design variable, having two components: the oxygen concentration and the coal feed rate entering the furnace.

In the Kriging system, the response $\mathrm{Y}(\mathrm{x})$ is expressed as the following regression model:

$$\mathrm{Y}(\mathrm{x}) = \mathbf{f}^{\mathrm{T}}(\mathrm{x})\boldsymbol{\beta} + \mathrm{E}(\mathrm{x}) \tag{6.6}$$

where $\mathbf{f}(\mathrm{x}) = [\, f_1(\mathrm{x}), f_2(\mathrm{x}), ..., f_m(\mathrm{x})]^{\mathrm{T}}$, $\boldsymbol{\beta} = [\beta_1, \beta_2, ..., \beta_m]^{\mathrm{T}}$ and m is the number of the basic functions in the regression model, $f(\mathrm{x})$ is a known kernel function of x, $\boldsymbol{\beta}$ is the regression coefficient vector, the first term on the right hand of the equation, $\mathbf{f}^{\mathrm{T}}(\mathrm{x})\boldsymbol{\beta}$, is the mean structure of the response and the second term $\mathrm{E}(\mathrm{x})$ is a stochastic process used to model the deviation from the mean structure, having zero mean and covariance which is written as follows:

$$\mathrm{Cov}(\mathrm{x}_i, \mathrm{x}_j) = \sigma^2 R(\mathrm{x}_i, \mathrm{x}_j), \qquad i, j = 1, 2, ..., n \tag{6.7}$$

where n denotes the number of the sample points, $R(\mathrm{x}_i, \mathrm{x}_j)$ is the correlation function and σ^2 is the process variance.

Consider n sample points, $\mathbf{x} = [\mathrm{x}_1, \mathrm{x}_2, ..., \mathrm{x}_n]$ with $\mathrm{x}_i \in \mathrm{R}^p$, P is the number of the design variables. Therefore, x is a $n \times P$ design matrix. The corresponding n responses are noted by $\mathbf{Y} = [\mathrm{y}(\mathrm{x}_1), \mathrm{y}(\mathrm{x}_2), ..., \mathrm{y}(\mathrm{x}_n)]$. From these sampled responses, the unknown parameters $\boldsymbol{\beta}$ and σ^2 can be estimated from the generalized least square regression:

$$\hat{\boldsymbol{\beta}} = (\mathbf{F}^{\mathrm{T}}\mathbf{R}^{-1}\mathbf{F})^{-1}\mathbf{F}^{\mathrm{T}}\mathbf{R}^{-1}\mathbf{Y} \tag{6.8}$$

$$\hat{\sigma}^2 = \frac{1}{n}(\mathbf{Y} - \mathbf{F}\hat{\boldsymbol{\beta}})^{\mathrm{T}}\mathbf{R}^{-1}(\mathbf{Y} - \mathbf{F}\hat{\boldsymbol{\beta}}) \tag{6.9}$$

where $\mathbf{F}$ is a vector including the values of $f(\mathrm{x})$ evaluated at the sample points and $\mathbf{R}$ is the correlation matrix, which is composed of the correlation function evaluated at each possible combination of the sample points:

$$\mathbf{R} = \begin{bmatrix} R(\mathrm{x}_1, \mathrm{x}_1) & \cdots & R(\mathrm{x}_1, \mathrm{x}_n) \\ \vdots & \ddots & \vdots \\ R(\mathrm{x}_n, \mathrm{x}_1) & \cdots & R(\mathrm{x}_n, \mathrm{x}_n) \end{bmatrix} \tag{6.10}$$

The Gaussian form correlation function is widely used in engineering problems and may be expressed as follows:

$$R(\mathrm{x}_i,\mathrm{x}_j)=\exp\left[-\sum_{k=1}^{p}\theta_k(\mathrm{x}_i^k-\mathrm{x}_j^k)^2\right] \tag{6.11}$$

where x_i^k is the k^{th} component of the sample point. The parameter θ is estimated by using a maximum likelihood estimation, and the problem converts to the minimization of the following function:

$$\Gamma(\boldsymbol{\theta})=\frac{1}{2}\left[\ln|\mathbf{R}|+n\ln(\hat{\sigma}^2)\right] \tag{6.12}$$

For an estimation of these parameters, the best linear unbiased prediction of the response at x is given by:

$$\hat{y}(\mathrm{x})=\mathbf{f}^{\mathrm{T}}(\mathrm{x})\hat{\boldsymbol{\beta}}+\mathbf{r}^{\mathrm{T}}(\mathrm{x})\mathbf{R}(\mathbf{Y}-\mathbf{F}\hat{\boldsymbol{\beta}}) \tag{6.13}$$

where $\mathbf{r}^{\mathrm{T}}(\mathrm{x})$ is a vector representing the correlation between the unknown point x and all known sample points:

$$\mathbf{r}^{\mathrm{T}}(\mathrm{x})=\left[R(\mathrm{x},\mathrm{x}_1),R(\mathrm{x},\mathrm{x}_2),...,R(\mathrm{x},\mathrm{x}_n)\right] \tag{6.14}$$

6.3.2 Design of experiments (DOE) for the ROM development

DOE is the preparation for the ROM development and its main task is to properly and efficiently design the sampling points so that the ROM developed can accurately represent the original physical models in the design space. Numerous sampling approaches have been developed, such as Latin Hypercube Design [221], Full Factorial Design [222], Fractional Factorial Design [223] and Orthogonal Arrays Design [224]. For this study, the Orthogonal Arrays Design approach is used because it is comparatively easy to realize when the numbers of the design variables are moderate, but more importantly, the obtained sampling points from the Orthogonal Arrays Design approach provide the convenience for comparison and analysis.

The design variables for the ROMs are the coal feed rate and the oxygen molar concentration of the oxidant gas mixture entering the boiler, which both highly affects the fluid dynamics, combustion and heat transfer in the furnace. The information required to drive the whole plant simulation, i.e. the heat transfer rate to the water wall and superheaters, the gas temperature

leaving the boiler and the peak temperature on the metal wall of the boiler, are set as the responses of the ROMs.

The coal feed rate for the full load operation (500 WM_e) of the original air-coal plant is 46.7 kg/s [56]. It is important for a power plant to be able to operate flexibly to follow as much as possible the fluctuating demand. However, a power plant cannot operate at a condition below its base load factor, which is between 60% and 70% [225] for Didcot-A, corresponding to a partial load of 350 WMe, or a coal feed rate of about 33 kg/s. Therefore this is the lower limit of the operating conditions investigated in this thesis. Therefore, for the full consideration of the possible working range, as well as the flexible operation of the plant, in the design space then the coal feed rate is set to be between 31.7 kg/s and 51.7 kg/s. This ensures that the full operational range of the 350-500 MW_e is covered, and the design space of the oxygen molar concentration varies from 21% to 35%.

Within the identified design space, the Orthogonal Arrays Design approach is performed in terms of both the thermal inputs and the oxygen enrichments so that twenty oxy-coal and five air-coal cases are selected, as summarised in Table 6.1. The ASU was assumed to provide an oxygen purity of 95%, with 5% inert gases. The oxidant gas stream flow rate is determined so that an oxygen concentration at the boiler exit of 5% by volume (dry basis) is achieved. Air leakage into the boiler was assumed to be 16 kg/s and this was assumed to come through the ash hopper [57]. The flue gas is recycled on a wet basis. The coal and primary air/gas enters the furnace at a temperature of 363 K and the swirled secondary and tertiary air/gas is preheated to a temperature of 530 K.

The CFD model results for the heat transfer to the water wall and superheaters, the furnace exit temperature and the peak wall temperature of these sampling cases (listed in Table 6.1), which are required for the integrated full plant simulation, are summarised in Table 6.7. Further, the boundary settings for the operating burners at different coal input rates are summarised from Table 6.2 to Table 6.6. It should be noted that the spilt fractions of the mass flow rates of the oxidant gas that enters the primary, secondary and tertiary inlets have been summarised in Chapter 3.

Coal, kg/s	O_2, vol%	Air	21	25	30	35
51.7	Recycle ratio, %	0	76.4	71.3	65.1	59.1
	Gas mass flow, kg/s	599.9	688.4	555.9	447.2	373.3
	Excess O2, vol%	5	5	5	5	5
	Air leakage, kg/s	16	16	16	16	16
46.7	Recycle ratio, %	0	76.2	71.0	64.8	58.8
	Gas mass flow, kg/s	540.3	619.3	500.1	402.3	335.9
	Excess O_2, vol%	5.0	5.0	5.0	5.0	5.0
	Air leakage, kg/s	16	16	16	16	16
41.7	Recycle ratio, %	0	75.9	70.7	64.5	58.4
	Gas mass flow, kg/s	480.8	550.2	444.3	357.4	298.4
	Excess O_2, vol%	5.0	5.0	5.0	5.0	5.0
	Air leakage, kg/s	16	16	16	16	16
36.7	Recycle ratio, %	0	75.5	70.3	64.0	58.0
	Gas mass flow, kg/s	421.2	481.2	388.5	312.5	260.9
	Excess O_2, vol%	5.0	5.0	5.0	5.0	5.0
	Air leakage, kg/s	16	16	16	16	16
31.7	Recycle ratio, %	0	75.1	69.8	63.4	57.3
	Gas mass flow, kg/s	361.6	412.2	332.7	267.7	223.5
	Excess O_2, vol%	5.0	5.0	5.0	5.0	5.0
	Air leakage, kg/s	16	16	16	16	16

Table 6.1 Operating conditions of the sampling points for the CFD simulations of the furnace.

	Air	Oxy21	Oxy25	Oxy30	Oxy35
Mass flow rate (kg/s)					
Primary	2.0	2.3	1.8	1.5	1.2
Secondary	1.5	1.7	1.4	1.1	0.9
Tertiary	6.5	7.4	6.0	4.8	4.0
Inlet temperature(k)					
Primary	363	363	363	363	363
Secondary	530	530	530	530	530
Tertiary	530	530	530	530	530
Oxygen concentration (mass %)					
Primary	23.2	19.3	19.3	19.3	19.3
Secondary	23.2	19.3	24.0	30.0	35.9
Tertiary	23.2	19.3	24.0	30.0	35.9

Table 6.2 Boundary settings for the operating burners at 31.7kg/s coal input rate.

	Air	Oxy21	Oxy25	Oxy30	Oxy35
Mass flow rate (kg/s)					
Primary	2.3	2.7	2.2	1.7	1.4
Secondary	1.8	2.0	1.6	1.3	1.1
Tertiary	7.6	8.7	7.0	5.6	4.7
Inlet temperature(k)					
Primary	363	363	363	363	363
Secondary	530	530	530	530	530
Tertiary	530	530	530	530	530
Oxygen concentration (mass %)					
Primary	23.2	19.2	19.2	19.2	19.2
Secondary	23.2	19.2	23.9	29.8	35.8
Tertiary	23.2	19.2	23.9	29.8	35.8

Table 6.3 Boundary settings for the operating burners at 36.7kg/s coal input rate.

	Air	Oxy21	Oxy25	Oxy30	Oxy35
Mass flow rate (kg/s)					
Primary	2.7	3.1	2.5	2.0	1.7
Secondary	2.0	2.3	1.9	1.5	1.2
Tertiary	8.7	9.9	8.0	6.5	5.4
Inlet temperature(k)					
Primary	363	363	363	363	363
Secondary	530	530	530	530	530
Tertiary	530	530	530	530	530
Oxygen concentration (mass %)					
Primary	23.2	19.2	19.1	19.1	19.1
Secondary	23.2	19.2	23.8	29.7	35.7
Tertiary	23.2	19.2	23.8	29.7	35.7

Table 6.4 Boundary settings for the operating burners at 41.7kg/s coal input rate.

	Air	Oxy21	Oxy25	Oxy30	Oxy35
Mass flow rate (kg/s)					
Primary	2.9	3.4	2.8	2.2	1.9
Secondary	2.2	2.6	2.1	1.7	1.4
Tertiary	9.5	11.2	9.0	7.3	6.1
Inlet temperature(k)					
Primary	363	363	363	363	363
Secondary	530	530	530	530	530
Tertiary	530	530	530	530	530
Oxygen concentration (mass %)					
Primary	23.2	19.1	19.1	19.1	19.1
Secondary	23.2	19.1	23.8	29.7	35.7
Tertiary	23.2	19.1	23.8	29.7	35.7

Table 6.5 Boundary settings for the operating burners at 46.7kg/s coal input rate.

	Air	Oxy21	Oxy25	Oxy30	Oxy35
Mass flow rate (kg/s)					
Primary	3.3	3.8	3.1	2.5	2.1
Secondary	2.5	2.9	2.3	1.9	1.6
Tertiary	10.8	12.4	10.0	8.1	6.7
Inlet temperature(k)					
Primary	363	363	363	363	363
Secondary	530	530	530	530	530
Tertiary	530	530	530	530	530
Oxygen concentration (mass %)					
Primary	23.2	19.1	19.1	19.1	19.1
Secondary	23.2	19.1	23.7	29.6	35.6
Tertiary	23.2	19.1	23.7	29.6	35.6

Table 6.6 Boundary settings for the operating burners at 51.7kg/s coal input rate.

Coal, kg/s	O_2, vol%	Air	Oxy21	Oxy25	Oxy30	Oxy35
51.7	Heat transfer to water walls, MW	472.9	370.7	432.1	508.2	567.8
	Heat transfer to super heaters, MW	425.5	414.2	455.1	479.2	467.5
	Total heat transfer, MW	898.4	784.9	887.2	987.4	1035.3
	Furnace exit temperature, K	1133.5	1141.7	1133.4	1112.1	1096.6
	Maximum wall temperature, K	1662.7	1537.8	1684	1804.8	1891.3
46.7	Heat transfer to water wall, MW	456.7	358.5	413.3	482.1	519.8
	Heat transfer to super heaters, MW	388.8	373.6	409.6	427.9	417.0
	Total heat transfer, MW	845.5	732.1	822.9	910.0	936.8
	Furnace exit temperature, K	1094.1	1112.0	1107.0	1082.8	1053.6
	Maximum wall temperature, K	1623.3	1499.6	1656.9	1773.3	1842.5
41.7	Heat transfer to water wall, MW	422.1	341.3	405.8	474.8	484.1
	Heat transfer to super heaters, MW	353.9	338.8	361.9	367.8	364.9
	Total heat transfer, MW	776.0	680.1	767.7	842.6	849.0
	Furnace exit temperature, K	1069.9	1082	1072.6	1055.9	1035.4
	Maximum wall temperature, K	1578.7	1463.3	1587.3	1697.9	1785
36.7	Heat transfer to water wall, MW	401.0	291.7	351.6	408.5	445.3
	Heat transfer to super heaters, MW	291.1	315.1	338.3	329.4	310.4
	Total heat transfer, MW	692.1	606.8	689.9	737.9	755.7
	Furnace exit temperature, K	1040.6	1038.5	1029.6	1011.2	996.9
	Maximum wall temperature, K	1531.8	1457.4	1599.7	1678.4	1723.8
31.7	Heat transfer to water wall, MW	370.9	274.4	325.8	375.2	407.3
	Heat transfer to super heaters, MW	254.2	288.6	290.5	279.6	261.5
	Total heat transfer, MW	625.1	563.0	616.3	654.8	678.8
	Furnace exit temperature, K	1004.9	1008.9	994.6	983.2	978.7
	Maximum wall temperature, K	1470.8	1440.4	1555.9	1620.7	1677.1

Table 6.7 Heat transfer and furnace exit temperature predictions from the boiler CFD simulations.

It should be noted that the CFD model has been validated by comparing the model predictions for the air-coal 46.7 kg/s base case listed in Table 6.5, with the in-house data from RWE npower and the available experimental measurements in section 5.1.3 (see Table 6.6). The CFD prediction of the furnace exit temperature of 1672 K is within 5% of the experimental measurement of 1591 K, and in close agreement with the in-house model used by the power station (1656 K).

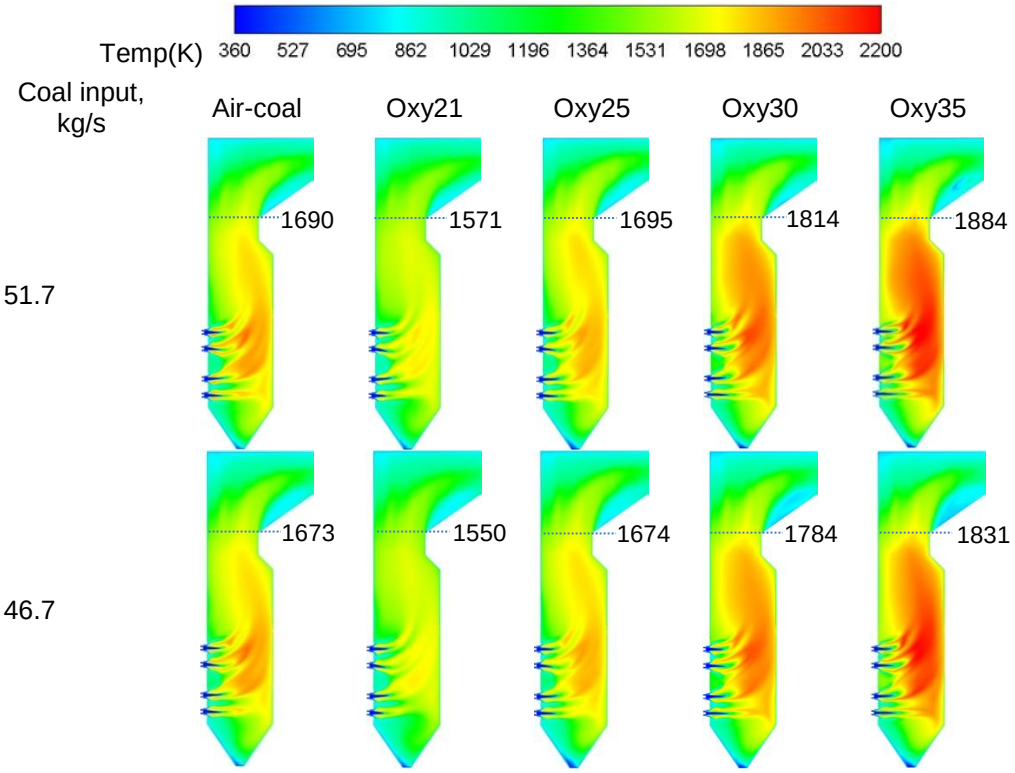

Figure 6.1 Part of the predicted temperature contours inside the boiler.

The CFD predicted results shown in Table 6.7 for the cases investigated indicate that the total heat transfer to the water walls and the superheaters are in general close to the data of the designed air-coal cases when the oxygen concentration lies within the range 25% - 30%, and this is in-line with the previous numerical and experimental results reported in the literature [56, 57, 226]. At the oxygen concentration of 21%, the total heat transfer values are about 10-13% lower than the corresponding air-coal cases; while at the oxygen concentration of 35%, the total heat transfer values is about 9% - 15% higher than the corresponding air-coal cases. Temperature distributions in the cross sections through the third column of

the burners are shown in Figure 6.1 for some of the air-coal and oxy-coal cases at two coal feed rates, in order to provide an indication of the variation in the temperature distributions in the furnace at different operating conditions.

Overall furnace temperatures for the oxy21 cases are lower than that of the air cases. On increase in the oxygen enrichments, the volume of the flame and the furnace temperature in general significantly increase and this would enhance the heat transfer to the water walls and also have an impact on the heat transfer to the downstream heat exchangers. The gas temperatures at furnace throat are marked out and as expected, these temperatures are observed to increase as the oxygen concentration and coal feed rate increase. The four separate rows of flames can be clearly seen, where the release and combustion of volatiles takes place. The burnout of the char particles is then completed in the regime above the volatile flames in the combined stream of hot gases rising towards the superheaters.

6.3.3 The obtained ROMs

The results obtained from the designed CFD simulations (see Table 6.7) are used as the input for the Kriging code so that if the unknown parameters $\hat{\boldsymbol{\beta}}$ and σ^2 in the Eq.(6.8) and (6.9) can be calculated, then the Kriging reduced order models in the form of Eq.(6.13) can be obtained. These reduced order models can be used to predict the following information at the unknown points: the heat transfer values to the different heat exchangers, the gas temperature at the boiler exit and the maximum wall temperature and they are obtained as a set of response surfaces (see Figure 6.2); with the coal feed rate varying from 31 kg/s to 52 kg/s and oxygen concentration varying from 21% to 35% (or 0.21 to 0.35).

These response surfaces will be used to model the transfer to the water/steam side of different heat transfer components inside the furnace, namely the water wall (Figure 6.2-(a)), platen 1 (Figure 6.2-(b)), platen 2 (Figure 6.2-(c)), SSH (Figure 6.2-(d)) and FRH (Figure 6.2-(e)). In addition, the ROMs for the exit gas temperature (Figure 6.2-(f)) and the peak temperature on the furnace wall (Figure 6.2-(g)) are also developed in order to drive the full plant simulation. Response surfaces for air-firing may also be

built and in this case the surfaces become curves as shown in Figure 6.3 and the air-coal ROMs only take the coal feed rate as the design variable, also varying from 31 kg/s to 52kg/s and the air-coal ROMs for the heat transfer to the water wall and the outlet gas temperature are presented.

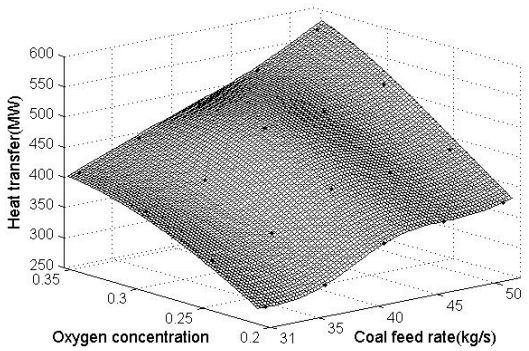

(a) Heat transfer to the water wall.

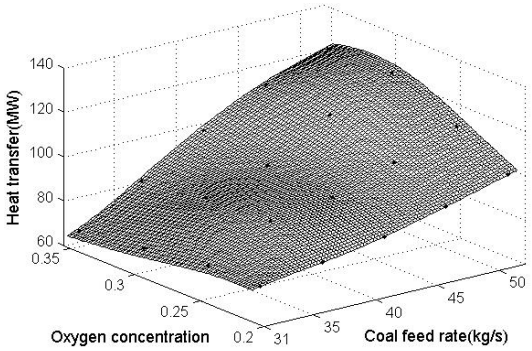

(b) Heat transfer to platen 1.

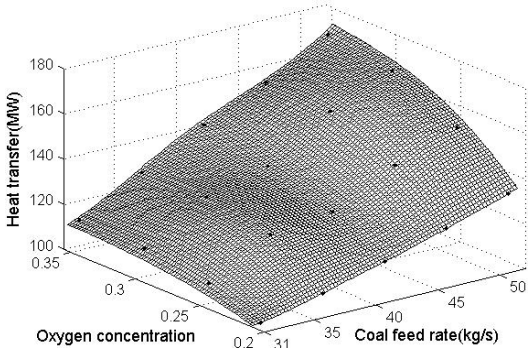

(c) Heat transfer to platen 2.

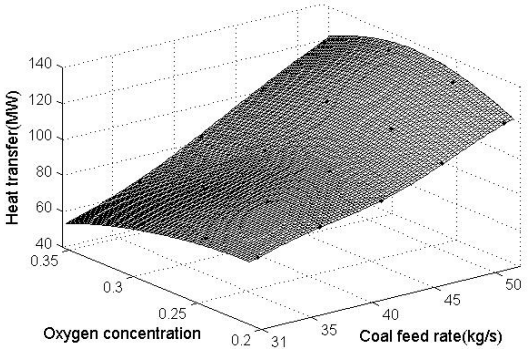

(d) Heat transfer to SSH.

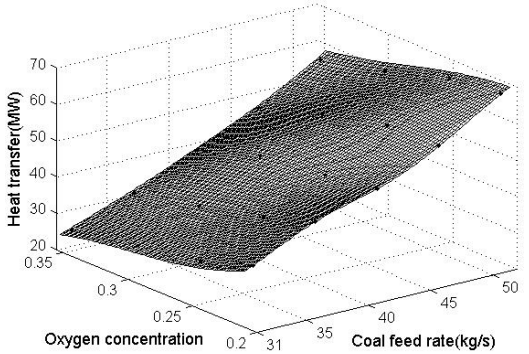

(e) Heat transfer to FRH.

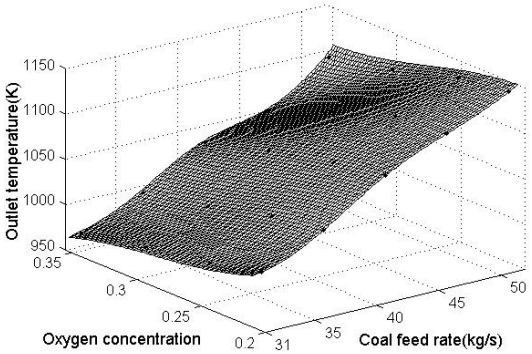

(f) Outlet temperature.

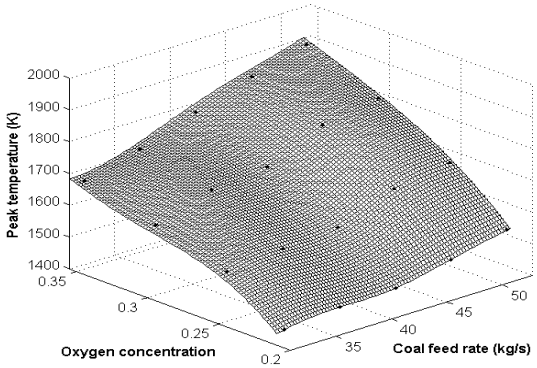

(g) Peak temperature on the metal wall.

Figure 6.2 ROMs for oxy-coal combustion of the boiler.

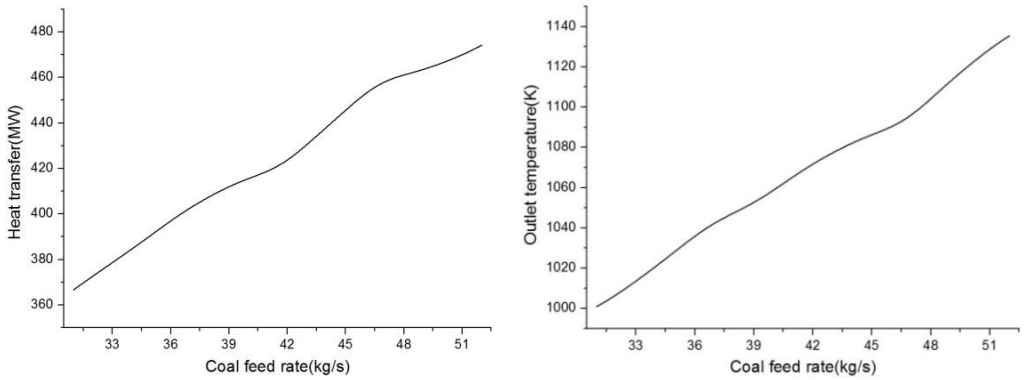

(a) Heat transfer to the water wall. (b) Outlet temperature.

Figure 6.3 ROMs for the air-coal combustion of the boiler.

As expected, the spatial nonlinearity of these ROMs, shown in Figure 6.2 and Figure 6.3, respect to the oxygen concentration and coal feed rate is clear. Therefore, a nonlinear interpolation method, such as Kriging, is required to represent the nonlinearity in developing the ROMs. In general, the heat transfer and temperatures increase as the coal feed rate increases. The changes in the coal feed rate and oxygen concentration on the one hand affect the thermal properties of the combustion gas, such as specific heat and radiation absorption capability, and on the other hand impact on the flow field in the furnace, such as velocity profiles, since the gas mass flow rate needs to vary accordingly. A combination of these two aspects leads to different trends at different coal feed rate conditions: (i) at a high coal feed rate, the heat transfer to water wall, platen 1, platen 2 and SSH generally increases as the oxygen concentration increases; (ii) however, in the low coal feed rate regime, the heat transfer to platen 1 and SSH presents a decreasing trend as oxygen concentration increases, this is mainly due to the change in the flow field. As for the heat transfer to the FRH, the heat transfer reduces throughout the design space as the oxygen concentration increases; this is because in each coal feed rate condition, the total heat transfer to the upstream water wall and superheaters is predicted to increase as oxygen concentration increases, thus less heat is carried by the flue gas travelling through the FRH, which is the last heat exchange component considered in the CFD modelling; and accordingly, the gas temperature at the outlet shows a similar decreasing trend. Further, the peak temperature of the furnace wall, including water wall and superheaters,

provides important safety information as to whether the wall temperature goes beyond the limit of the tube material and the peak temperature is predicted to be located on the bottom of the superheater platen 2.

6.3.4 Validation of the ROMs

In order to validate the accuracy of the ROMs, four additional CFD oxy-coal cases (cases 1-4), see Table 6.8, and two extra air-coal cases (cases 5, 6), see Table 6.8, are randomly chosen and calculated and the results obtained are compared to the ROMs values.

Case number	1	2	3	4	5	6
Coal feed rate (kg/s)	35.0	38.0	43.0	46.7	39.0	50.0
O_2 concentration	0.24	0.23	0.27	0.325	air	air

Table 6.8 Coal feed rates and oxygen concentrations of the validation cases.

		Water wall (MW)	Platen 1 (MW)	Platen 2 (MW)	SSH (MW)	FRH (MW)	Outlet T (K)	Max T (K)
Case 1	CFD	328.1	86.7	115.1	86.1	39.3	1017.1	1560.2
	ROMs	323.8	83.9	117.5	83.6	38.2	1018.5	1549.2
	error	-1.3%	-3.2%	2.1%	-3.0%	-2.2%	0.1%	-1.0%
Case 2	CFD	330.8	89.5	120.6	90.6	45.2	1045.6	1534.1
	ROMs	336.3	86.3	118.6	88.6	43.7	1046.3	1520.0
	error	1.7%	-3.6%	-1.7%	-2.2%	-3.3%	0.1%	-1.0%
Case 3	CFD	431.4	99.2	136.7	95.5	48.8	1074.8	1675.5
	ROMs	444.2	95.9	134.1	98.5	49.0	1076.7	1652.3
	error	3.0%	-3.3%	-1.9%	3.1%	0.4%	0.2%	-1.4%
Case 4	CFD	509.1	112.4	156.2	111.2	49.7	1069.3	1812.9
	ROMs	506.7	112.9	154.6	108.4	49.5	1067.4	1810.1
	error	-0.5%	0.4%	-1.0%	-2.5%	-0.4%	-0.2%	-0.2%
Case 5	CFD	406.2	82.2	115.4	81.0	40.2	1050.9	1566.8
	ROMs	412.0	81.9	115.0	79.4	40.2	1052.7	1553.8
	error	1.4%	-0.4%	-0.3%	-2.0%	0.0	0.2%	-1.0%
Case 6	CFD	469.2	98.8	137	110.5	59.3	1125.5	1641.7
	ROMs	466.5	102	139.1	113.3	58.7	1121.1	1650.2
	error	-0.6%	3.2%	1.5%	2.5%	-1.0%	-0.4%	1.0%

Table 6.9 Comparisons of heat transfer and temperature predictions between the CFD and ROMs.

The comparisons of the results from CFD and ROMs are summarised in Table 6.9. The maximum relative error between the results from CFD and

ROMs is within ±4%, and therefore the ROMs are considered to be sufficiently accurate to be used in calculating the heat transfer, outlet temperature and maximum temperature on the metal wall within the modelled range. With the newly developed ROMs, the heat transfer and temperature values can be calculated very efficiently and the CPU time is negligible in comparison to CFD simulations.

6.4 Model validation and discussions on the whole plant co-simulations

6.4.1 Validation of the integrated CFD/process full plant model

This integrated full plant model is validated by comparing the results obtained to those obtained from RWE's in-house code MOPEDS, which was developed for modelling the air-coal firing of the power plant and only full load air-coal firing simulation results are available. The predicted steam/water and gas temperatures entering and leaving the heat exchangers are shown in Table 6.10 and Table 6.11, respectively.

Temperatures (K)						
	Inlet			Outlet		
	This model	MOPEDS	Error, %	This model	MOPEDS	Error, %
Platen 1	656	654	0.3	728	718	1.4
Platen 2	676	682	-1.0	764	752	1.6
SSH	761	752	1.2	841	841	0
FRH	760	736	3.3	832	841	-1.1
PSHV	649	648	0.2	651	654	-0.5
PSH	629	628	0.2	655	648	1.1
Econ	522	523	-0.2	581	573	1.4
PRHV	706	694	1.7	766	736	4.1
PRH	625	638	-2.0	711	694	2.5

Table 6.10 A comparison in the temperature predictions on the steam side from MOPEDS and the full plant model for the heat exchangers.

Since the gas side temperatures of the superheaters are considered in the CFD model rather than the full plant model, the gas temperature for platen 1, platen 2, SSH and FRH are not compared. The values in the Table 6.10 and Table 6.11 indicate that the maximum relative difference between the results

from MOPEDS and the integrated CFD/process model is found be the temperature of the gas at the inlet of the economiser (Econ), which is about 4%. The predicted results of the steam generation mass flow rate, steam pressure and steam temperature in the steam drum are compared in Table 6.12, showing the relative errors are within ±1%. Considering that MOPEDS was built on measurements for this particular type of furnace, it is considered to be reliable and therefore it may be concluded that this newly developed integrated full plant model can give reasonable representations of the real power plant.

	Temperatures (K)					
	Inlet			Outlet		
	This model	MOPEDS	Error, %	This model	MOPEDS	Error, %
PSHV	1091	1054	3.5	1062	1027	3.4
PSH	1062	1027	3.4	783	756	3.6
Econ	786	756	4.0	636	621	2.4
PRHV	1062	1027	3.4	955	923	3.5
PRH	957	923	3.7	793	769	3.1

Table 6.11 A comparison in the temperature predictions on the gas side from MOPEDS and the full plant model for the heat exchangers.

	Steam generated (kg/s)	Drum pressure (bar)	Steam temperature (K)
This model	393	178	629
MOPEDS	390	178	628
Error	0.7%	0	-0.1

Table 6.12 A comparison in the predictions of MOPEDS and the full plant model for the steam drum.

6.4.2 Results and discussions

When a conventional coal-fired power plant is retrofitted into an oxy-coal power plant, the fundamental combustion environment in the furnace is changed, and thus impacts on the heat transfer characteristics of the boiler. In order to investigate the impact of an oxy-coal upgrade on the heat transfer and steam generation of this conventional power plant, this section analyses the simulation results of the “retrofitted” power plant under the working scenarios of air-coal, oxy21, oxy23, oxy25, oxy27.5, oxy30, oxy32.5 and oxy35 in four different electricity load levels, namely 500MW_e (full load),

450MW_e, 400MW_e and 350MW_e, which cover the designed full operational regime of the power plant. In these investigated power load levels, the coal consumption rates are predicted to be different and these obtained values are about 47 kg/s for 500MW_e operation, 42 kg/s for 450MW_e operation, 38 kg/s for 400M_e operation and 33 kg/s for 350MW_e operation.

6.4.2.1 Impacts of the oxy-coal retrofit on the evaporative heat transfer and steam generation

A key parameter describing the output capacity of a coal-fired power plant is the generated steam mass flow rate, which is dictated by the heat transferred to the water walls, namely the evaporative heat. With an oxy-coal retrofit, the original evaporative heat transfer under air-coal firing condition is changed.

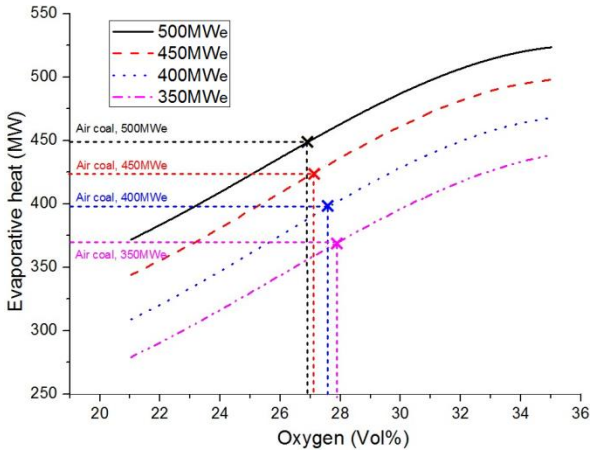

Figure 6.4 The predicted evaporative heat as a function of oxygen concentration.

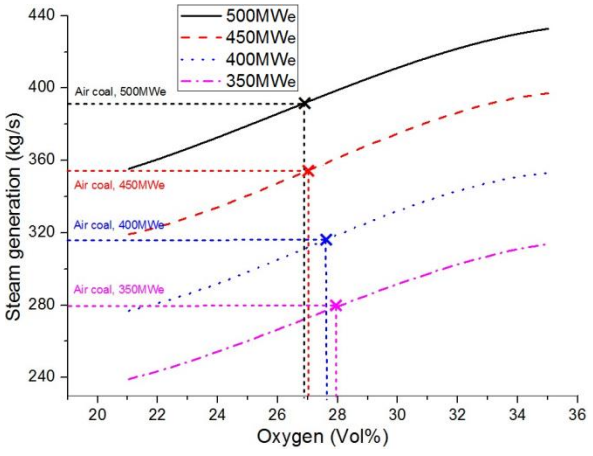

Figure 6.5 The predicted steam generation as a function of the oxygen concentration.

The predicted evaporative heat transfer and steam generation rates from the steam drum at the four different electricity output levels are plotted in Figure 6.4 and Figure 6.5 as a function of the oxygen concentration. For comparison, the corresponding evaporative heat values under air-coal firing mode are marked by the symbol ×. The intersections of the vertical dashed lines and the horizontal axis are the matching points where the evaporative heat or steam generation from the steam drum under oxy-coal can be matched with the air-coal conditions. In general, the evaporative heat as the oxygen concentration rises is because the flame temperature in the combustion furnace increases when the oxygen concentration of the gas entering the boiler increases, thus the radiation to the surrounding water walls becomes more intense. The steam generation from the steam drum is the physical phenomenon of the evaporative heat transfer and therefore the steam generation from the drum also increases as the oxygen concentration increases. The steam generation can be approximately matched to air-coal firing within the oxygen concentration range of 27%-28% for the full operational range of the plant.

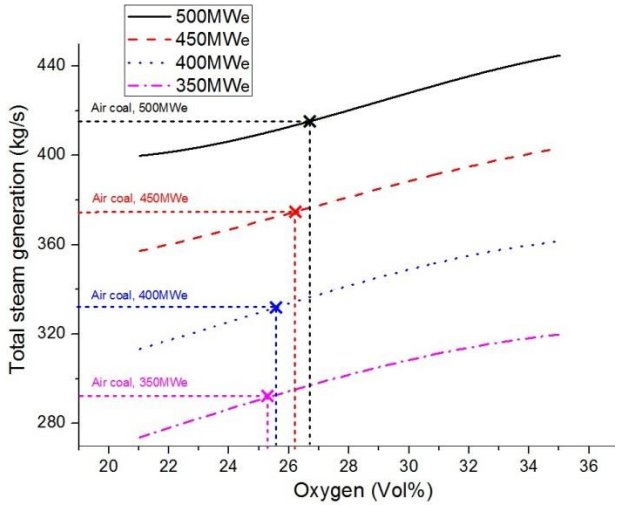

Figure 6.6 The predicted steam generation as a function of the oxygen concentration.

It should be noted that the steam generated from the steam drum is not the total steam that drives the steam turbines. Although most steam comes from the steam drum, a small amount of additional steam is introduced by the external water sprayed into the superheat steam at the inlet of superheater

platen 2, in order to maintain an endurable wall temperature for the superheaters. If more water spray is required then less steam would be required from the steam drum. The total steam generated that enters the steam turbine is presented in Figure 6.6, and it indicates that the total steam generation can be matched with the air-firing cases within the oxygen concentration range 25%-27%. It is interesting to note that when comparing the total steam generation with the steam generation from the drum shown in Figure 6.5, less steam would be required from the drum when the plant is retrofitted to oxy-firing, in particular at low load conditions.

6.4.2.2 Impacts of an oxy-coal retrofit on the heat transfer inside and outside the furnace

In the furnace, where combustion of coal takes place, the heat transfer to the water wall, platen superheaters and the reheater (platen 1, platen 2, SSH and FRH shown in Figure 5.1), which are calculated from the CFD ROMs, are dominated by radition, i.e. radiative heat transfer. As the flue gas comes out from the furnace, the gas temperature is about 1100 K (for 500MW_e operation) or even lower, and the steam/water temperatures in the downstream heat exchangers (PSHV, PRHV, PRH, PSH and ECON shown in Figure 5.7) vary from 600 to 800 K. Thus radiation is not considered the dominant form of heat transfer [141] but by convective heat transfer. Figure 6.7 and Figure 6.8 respectively compares the contributions of the radiative and convective heat transfers to the steam generation cycle.

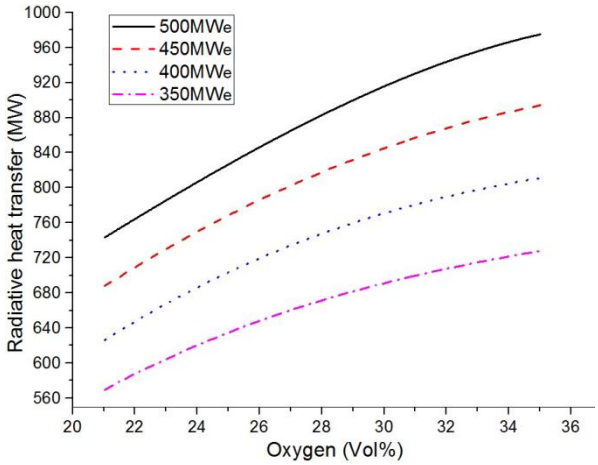

Figure 6.7 The predicted radiative heat transfer as a function of the oxygen concentration.

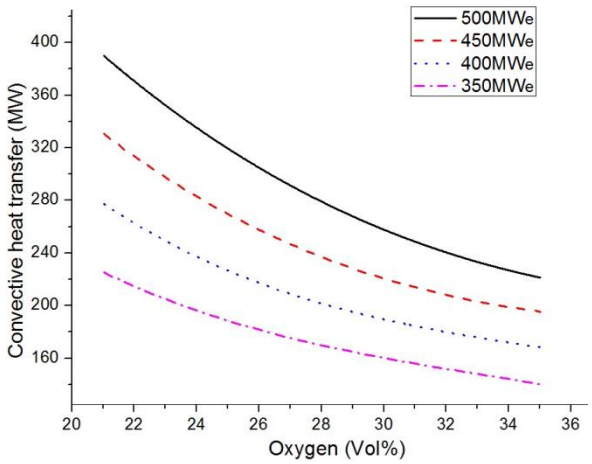

Figure 6.8 The predicted convective heat transfer to the water/steam cycle as a function of oxygen concentration.

Clearly, the radiative heat dominates the process and it increases as the oxygen concentration increases while the opposite trend can be observed for the convective part. As the oxygen concentration increases, the gas temperature increases so that the radiation is also strengthened [56, 57]. On the other hand, (i) as the oxygen concentration increases, the recycle ratio of the flue gas decreases, leading to a lower mass flow rate of the flue gas going through the convective heat exchangers; (ii) as the oxygen concentration increases, the gas temperature leaving the final reheater (FRH), which is the last heat transfer component considered in the CFD model, decreases since the total heat input to the furnace is kept almost constant. These two factors cause a decrease in the internal heat carried by the flue gas that goes through the convective heat exchangers.

6.4.2.3 Impacts of the oxy-coal retrofit on the steam temperatures

In the super heat region of the boiler, the super heat steam passes through the platen 1, water sprayer, platen 2 and SSH sequentially. In addition to investigating the heat transfer from the gas side, it is of interest to look into the steam temperature change along these super heat components on the steam side. Therefore the predicted steam temperatures at the inlet/outlet of these elements are presented in Figure 6.9 and Figure 6.10 in a sequential order that the steam goes through, and they are linked with straight lines in order to show the general trend of the temperature variations. In addition, only the 500MW_e and 400MW_e simulation results are presented, since the 450MW_e and 350MW_e results show similar patterns. In general, the steam

temperatures increase as the super heat steam passes through platen 1 to SSH. Significant drops are observed in the water sprayer where the super heat steam mixes with the sprayed water so that the downstream steam temperature would not become too high to protect the metal tubes, and this is achieved by a PI controller, to maintain the steam temperature at the outlet of the SSH to the control target of approximately 841 K. The steam temperatures in platen 2 and SSH are predicted to be very close for all the cases investigated; while the largest temperature differences are observed in platen 1 and the water sprayer.

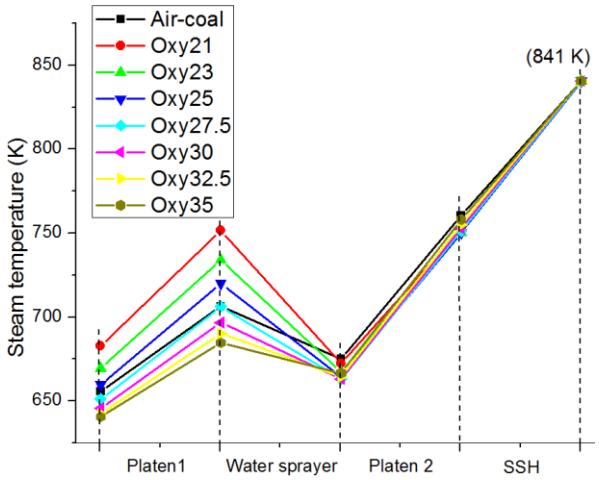

Figure 6.9 Predicted steam temperatures at the inlet/outlet of the super heat components at 500MW$_e$ operation.

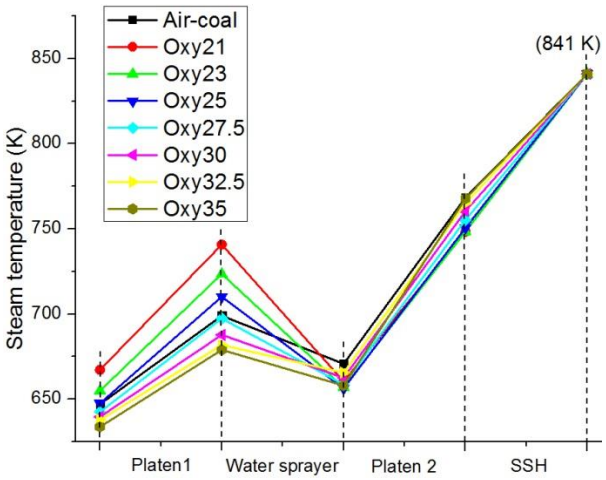

Figure 6.10 Predicted steam temperatures at the inlet/outlet of the super heat components at 400MW$_e$ operation.

6.4.2.4 Impacts of the oxy-coal retrofit on the steam temperatures

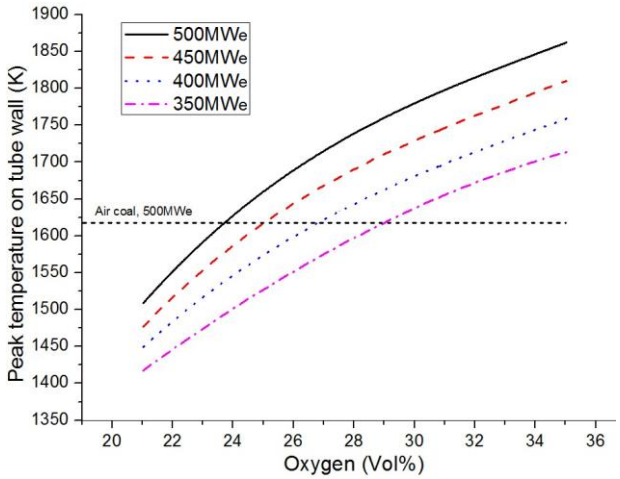

Figure 6.11 Predicted peak temperatures on the tube wall.

As discussed in Section 6.3.3, the peak wall temperature was predicted to be located at the bottom of the superheater platen 2. Under air-firing, the highest wall temperature is approximately 1620 K at full load, see Figure 6.11. It is important to note that the predicted peak temperatures of the tube wall under oxy-coal firing are higher than 1620 K under full load air-coal firing when the oxygen concentrations are higher than about 23.5% for 500MWe, 25% for 450MWe, 27% for 400MWe and 29% for 350MWe, see Figure 6.11. If the retrofitted unit is to be operated at an oxygen level of 25%-27% then: (i) for the full load operation of 500MWe, the temperature increase is approximately 60 (for 25%)-100 (for 27%) K above 1620 K; (ii) for the partial load condition of 450MWe, the temperature increase is negligible at the oxygen level of 25%, but gradually increases to 70 K at the oxygen level of 27%; (iii) for other partial load conditions of 400MWe and 350MWe, the peak temperature increases is lower than 1620 K for oxygen concentrations of 25%-27%.

Therefore, attention must be paid when this retrofitted power plant operates beyond 450MWe, due to the temperature increase. If the tube material of platen 2 cannot endure the temperature increase, then an upgrade on the material is required.

6.5 Conclusions

This chapter investigates the potential of retrofitting a conventional air-coal power plant to oxy-coal firing and the possible required inlet oxygen concentrations to achieve a similar plant performance to that of air-coal firing. To achieve this, an integrated full plant co-simulation model has been developed. In order to accurately model the heat transfer and temperature characteristics in the furnace, a high fidelity CFD method is used to account for the fluid dynamics, combustion, and heat transfer inside the furnace. Then a set of fast reduced order models (ROMs) has been built using the Kriging method which can be efficiently integrated into the process model.

A range of air-coal and oxy-coal conditions in different power loads from 350MW_e to 500MW_e, has been simulated. The results obtained indicate that it is possible to retrofit the air-coal firing power plant to oxy-coal firing and achieve the original designed performances of the power plant in air-coal firing. However, the impact of the retrofit is expected to be different for different parts of the plant. The biggest impacts observed are to the steam generation from the steam drum and the steam temperature at the exit of the super heater platen 1. It is suggested that an oxygen enrichment range of 25%-27% would be adequate for the retrofitted plant to match the performance achievable under air-firing for the full operational load regime of the plant. Clearly, optimisation of the retrofitted plant would be required to determine the optimal oxygen enrichment for each particular load. Further, the peak temperature would increase in the oxy-coal mode, in particular on the superheater platen 2. If the tube material cannot endure the temperature increase, then an upgrade on the material may be required.

Chapter 7. Summary and the recommended work for f

7.1 Summary

The CO_2 emitted from the coal-fired power plants is one of the most significant boosters that contribute to the global warming. Therefore, it is urgent to employ carbon capture technologies, such as the oxy-coal combustion and post-combustion approaches that can be applied to the existing or new built power plants. These technologies are close to commercial use, however, further investigations are still required to fully address the technical barriers, e.g. the heat transfer characteristics switching from air-coal firing to oxy-coal firing which then disturbs the performances of the power plants which were originally designed for air-coal operations. The use of a CFD modelling approach with sub-models offers a good opportunity to accurately investigate the detailed heat transfer distributions under both air-coal and oxy-coal conditions inside the boiler; however, apart from the combustion boiler, a large-scale power plant includes a number of other components which would be inhibited to be modelled by CFD techniques due to huge demand on computational resources and time. The whole system process modelling techniques provide a promising option to efficiently study the engineering processes involving carbon capture technologies as much less computation time is required. However, traditional process modelling depends on zero or one-dimensional equations with a number of empirical constants for the gaseous radiative properties in order to describe the combustion and heat transfer process in the combustion boiler. Thus, the exact boiler configurations and arrangements of the heat exchanger, which affects the heat transfer distributions, are difficult to be accurately represented by the traditional process modelling approaches. In addition, the empirical constants, may be insufficient to describe the gaseous radiative properties under oxy-combustion environments, where the fundamental properties and compositions of the combustion gas are quite different from air-coal firing conditions.

In this case, it has become state-of-the-art to use a CFD and process co-simulation approach to investigate the performances of the coal-fired power plants using CO_2 capture technologies. The co-simulation strategy can be simply described as follows: the CFD techniques account for the coal combustion process and the complex heat transfer distributions inside the boiler, then the predicted heat transfer to the water/steam side or the gas compositions at the outlet can be used to drive the process simulation for rest part of the system. Then, the process simulation predicts the coal feed rate to the boiler to generate sufficient amount of steam and to achieve a required electricity output level. The predicted coal feed rate is returned to the CFD models as boundary conditions to start new CFD simulations so that a direct link between CFD and process modelling is achieved.

However, the direct coupling between CFD and process modelling is impractical and inefficient because a CFD simulation usually consumes much more time compared to a process simulation, especially when the CFD simulation is based on three dimensional involving complex chemical reactions, strong turbulence and heat transfer and all of these need to be solved using a large size of computational mesh. Therefore, to develop an efficient communication between CFD and process modelling is very important and this is the major task of this thesis.

Towards the main task, the investigations in this thesis have been performed step by step:

(i) In order to preliminarily test the feasibility of applying the CFD and process co-simulation approaches to the CO_2 capture technologies, the pilot-scale PACT CCS facility in Beighton is taken to be modelled using a CFD and process co-simulation approach. Specially, the coal combustion process in the 250 kW_{th} furnace of the facility is modelled by a CFD approach; the capture of CO_2 in the PACT amine capture plant is achieved by a chemical absorption plant using MEA and this process is modelled using a process simulator. The furnace CFD model and the CO_2 capture plant process model are separately validated by comparing their simulation results to the experimental data. The temperatures, mass flow rates and compositions of the flue gas at the furnace outlet are obtained from CFD simulations, which

accounts for the firing of the furnace with different thermal inputs. These information will be used as the input data to drive the CO_2 capture process simulations. It has been confirmed that the direct link between CFD and process modelling is impractical and inefficient, therefore, the predicted gas temperatures and mass flow rates at the burner outlet are regressed as polynomial curves vary with thermal input to the furnace. As for the gas compositions, they are considered as averaged constants as they vary little at different thermal inputs once the exit oxygen concentration is kept the same.

Then these polynomial curves and composition information are coded into the PACT system process model and a preliminary CFD and process co-simulation scheme is achieved. A set of simulations at different thermal inputs to the combustion facility and CO_2 capture ratios have been performed and the simulation results indicate that the operations of a CO_2 capture plant can be similar under a certain CO_2 capture ratio once the L/G ratio is set the same.

It needs to be noted that, the integration of the CFD and the process simulation techniques can be achieved in different manners, e.g. the CFD modelling techniques can be used to simulate the chemical absorption process inside the column so that the temperature, pressure and compositions profiles along the height of the column can be used in the process simulation models in the form of reduced order models. However, the CFD simulation of the absorber column is technically challenging since the mesh of the three dimensional random packing, the multiphase flow and the chemical reaction kinetics are difficult to be properly considered. Thus, these integration manners are not investigated in this thesis, although they are meaningful.

(ii) Further, in Chapter 5, the research object is extended to a large-scale power plant. Typically, the process models for the whole plant are introduced and a detailed CFD model for the utility boiler of the power plant is developed.

The CFD simulations for the utility boiler of this power plant have been performed under both air-coal and oxy-coal firing conditions in order to

investigate the differences between the two firing modes in terms of heat transfer characteristics. As for the process models for the power plant, each process component is represented by a set of fundamental equations which account for the mass balance, energy balance and physical properties. Both the CFD and the process simulations indicate that the heat transfer characteristics inside the boiler under the air-coal firing condition can be matched to oxy-coal firing between 25% and 30% of oxygen concentration. However, the simulations do not consider the impacts of the coal feed rate to the boiler. It needs to be noted that, under different coal feed rates, the heat transfer distributions to the different heat exchangers of the boiler may vary. In addition, the full plant process model contains several assumptions which may not be suitable for oxy-coal modelling and the major limitation is that the model constants used to calculate the heat transfer were originally developed from an air-coal firing database, thus they may not be suitable for oxy-coal conditions.

Currently, there are no such model constants can be confidently used in oxy-coal conditions, therefore, it is necessary to integrate the oxy-coal CFD predictions to the process simulations.

(iii) In chapter 6, a new approach has been developed for achieving a CFD and process co-simulation strategy for simulating the operations of the Didcot-A large-scale power plant. This approach is used to estimate the potential of retrofitting this originally air-coal firing power plant to oxy-firing.

Based on the heat transfer and temperature predictions from the CFD boiler simulations, a set of reduced order models (ROM) has been developed to link the CFD predictions to the whole plant process model in order to simulate the performance of the power plant under different load and oxygen enrichment conditions if retrofitted to oxy-firing. Specifically, the ROMs are developed using the Kriging non-linear interpolation approach from a range of CFD simulations that cover the possible working range of the boiler at different coal feed rates and oxygen enrichments entering the boiler. The ROMs are able to calculate the heat transfer and temperature values very efficiently and the CPU time is negligible in comparison to CFD simulations.

A set of co-simulations have been performed at different load conditions and different oxygen concentrations entering the boiler. The results reveal that this 500 MW_e power plant is possible to be retrofitted to oxy-firing without disturbing the overall performance of the plant. Similar heat transfer characteristics and steam generation in the boiler can be maintained to those under air-firing. The oxygen molar enrichment between 25% and 27% is found to be feasible for the oxy-coal operations of this retrofitted power plant at different power loads conditions. However, the peak temperature on one superheater may increase in the oxy-coal mode so that an upgrade on the material may be required if the tube material cannot endure the temperature increase.

7.2 Future work

There are several issues that require further investigations:

(i) Currently, the modelling of the CO_2 capture process using MEA in a absorber column totally depends on process simulations which involves empirical correlations for the mass transfer, chemical reactions, pressure drop along the height of the column. In addition, the traditional process simulation does not consider the actual configurations of the packing inside the column. All these may cause errors. Therefore, the CFD modelling techniques can be used directly to model the chemical absorption process inside the column and the simulation results can be used to generate fast reduced order models to be integrated into the process models so that efficient and accurate co-simulation models can be obtained.

(ii) The biomass is also an attractive optional fuel for the power plants for its fast regeneration ability and comparatively low pollution. The co-simulation approach developed in this thesis can be used to simulate the operations of the power plants under the oxy-biomass firing mode. Similar to the Chapter 6, the potential of retrofitting the conventional air-coal power plant to oxy-biomass firing can be evaluated. In addition, the oxy-coal and the oxy-biomass firing modes can be compared to the original air-coal firing mode in order to identify the different impacts of these modes on the overall

performance, such as heat transfer and steam generation, of the power plant. This part of work will be performed as an extension of this thesis.

(iii) The reduced order models generated in this thesis are based on a set of steady-state CFD simulations, thus they are only eligible for steady-state process simulations. However, in fact the operations of the power plants are dynamic and an understanding of the dynamic response of the whole system to the changes in operations is important. Therefore, dynamic reduced order models are required. However, the generation of the dynamic reduced order models is challenging as dynamic CFD simulations can be quite computationally expensive, especially for a three dimensional large-scale boiler.

List of References

[1] Coal in 2013, Department of Energy & Climate Change, 2014.

[2] Environmental Consequences of the Chernobyl Accident and their Remediation: Twenty Years of Experience, International Atomic Energy Agency, 2006.

[3] BP Statistical Review of World Energy, BP, 2014.

[4] Fukushima Nuclear Accident Analysis Report, (2012).

[5] International Energy Policy in the Aftermath of the Fukushima Nuclear Disaster, Center for Energy and Environmental Policy, University of Delaware, 2013.

[6]http://www.visualphotos.com/image/2x4656220/coal_burner_in_furnace_in_power_station.

[7]http://www.theccc.org.uk/tackling-climate-change/the-science-of-climate-change/climate-variations-natural-and-human-factors/greenhouse-gas-emissions/.

[8] http://en.wikipedia.org/wiki/Chernobyl_disaster.

[9] Kyoto Protocol to the United Nations Framework Convention on Cilmate Change, United Nations, 1998.

[10] A Roadmap for moving to a competitive low carbon economy in 2050, European Commission, 2011.

[11] R.L. Jane Leggett, Carl Ek, Larry Parker, An Overview of Greenhouse Gas (GHG) Control Policies in Various Countries, Congressional Research Service, 2009.

[12] J. Ramseur, State CO2 Emission Rate Goals in EPA's Proposed Rule for Existing Power Plants, Congressional Research Service, 2014.

[13] America's Dirtiest Power Plants, Environment America Research & Policy Center, 2014.

[14] I.E.A. (IEA), Technology Roadmap Carbon Capture and Storage, Paris, 2013.

[15] CO2 Capture Technologies: Pre-combustion Capture, Global CCS Institute, 2012.

[16] P. Edge, Modelling and simulation of oxy-coal fired power plants, University of Leeds, PhD, 2011.

[17] Carbon capture technology: future fossil fuel use and mitigating climate change, Grantham Institute for Climate Change, Imperial College London, 2010.

[18] http://www.ccsassociation.org/why-ccs/ccs-projects/current-projects/.

[19] M. Wang, A. Lawal, P. Stephenson, J. Sidders, C. Ramshaw, Post-combustion CO2 capture with chemical absorption: A state-of-the-art review, Chemical Engineering Research and Design, 89 (2011) 1609-1624.

[20] C. Sun, S. Wang, S. Zhou, C. Chen, SO2 effect on monoethanolamine oxidative degradation in CO2 capture process, International Journal of Greenhouse Gas Control, 23 (2014) 98-104.

[21] K. Goto, K. Yogo, T. Higashii, A review of efficiency penalty in a coal-fired power plant with post-combustion CO2 capture, Applied Energy, 111 (2013) 710-720.

[22] K. Stéphenne, Start-up of World's First Commercial Post-combustion Coal Fired CCS Project: Contribution of Shell Cansolv to SaskPower Boundary Dam ICCS Project, Energy Procedia, 63 (2014) 6106-6110.

[23]http://www.hd.jxgroup.co.jp/english/newsrelease/upload_pdf/20140715_02_01_1050061.pdf.

[24]http://www.power-technology.com/projects/peterhead-carbon-capture-and-storage-ccs-project-scotland/.

[25] T. Wall, Y. Liu, C. Spero, L. Elliott, S. Khare, R. Rathnam, F. Zeenathal, B. Moghtaderi, B. Buhre, C. Sheng, R. Gupta, T. Yamada, K. Makino, J. Yu, An overview on oxyfuel coal combustion—State of the art research and technology development, Chemical Engineering Research and Design, 87 (2009) 1003-1016.

[26] H. Hagi, M. Nemer, Y. Le Moullec, C. Bouallou, Towards Second Generation Oxy-pulverized Coal Power Plants: Energy Penalty Reduction Potential of Pressurized Oxy-combustion Systems, Energy Procedia, 63 (2014) 431-439.

[27] A.R. Smith, J. Klosek, A review of air separation technologies and their integration with energy conversion processes, Fuel Processing Technology, 70 (2001) 115-134.

[28] A. Komaki, T. Gotou, T. Uchida, T. Yamada, T. Kiga, C. Spero, Operation Experiences of Oxyfuel Power Plant in Callide Oxyfuel Project, Energy Procedia, 63 (2014) 490-496.

[29]http://www.whiteroseccs.co.uk/about-carbon-capture-storage/oxyfuel-technology-processes.

[30] J.F. Price, Lagrangian and Eulerian Representations of Fluid Flow: Kinematics and the Equations of Motion, Woods Hole Oceanographic Institution, 2006.

[31] Y. Fei, S. Black, J. Szuhánszki, L. Ma, D.B. Ingham, P.J. Stanger, M. Pourkashanian, Evaluation of the potential of retrofitting a coal power plant to oxy-firing using CFD and process co-simulation, Fuel Processing Technology, 131 (2015) 45-58.

[32] A. Williams, M. Pourkashanian, J.M. Jones, N. Skorupska, Combustion and gasfication of coal, Taylor & Fracncis, New York, 1999.

[33] M.M. Baum, P.J. Street, Predicting the Combustion Behaviour of Coal Particles, Combustion Science and Technology, 3 (1971) 231-243.

[34] L. Chen, S.Z. Yong, A.F. Ghoniem, Oxy-fuel combustion of pulverized coal: Characterization, fundamentals, stabilization and CFD modeling, Progress in Energy and Combustion Science, 38 (2012) 156-214.

[35] J. Yu, J.A. Lucas, T.F. Wall, Formation of the structure of chars during devolatilization of pulverized coal and its thermoproperties: A review, Progress in Energy and Combustion Science, 33 (2007) 135-170.

[36] P.R. Solomon, M.A. Serio, E.M. Suuberg, Coal pyrolysis: Experiments, kinetic rates and mechanisms, Progress in Energy and Combustion Science, 18 (1992) 133-220.

[37] J.R. Gibbins, R. Kandiyoti, The effect of variations in time-temperature history on product distribution from coal pyrolysis, Fuel, 68 (1989) 895-903.

[38] G.M. Kimber, M.D. Gray, Rapid devolatilization of small coal particles, Combustion and Flame, 11 (1967) 360-362.

[39] S. Badzioch, P.G.W. Hawksley, Kinetics of Thermal Decomposition of Pulverized Coal Particles, Industrial & Engineering Chemistry Process Design and Development, 9 (1970) 521-530.

[40] H. Kobayashi, J.B. Howard, A.F. Sarofim, Coal devolatilization at high temperatures, Symposium (International) on Combustion, 16 (1977) 411-425.

[41] A. Silaen, T. Wang, Effect of turbulence and devolatilization models on coal gasification simulation in an entrained-flow gasifier, International Journal of Heat and Mass Transfer, 53 (2010) 2074-2091.

[42] T.H. Fletcher, D.R. Hardesty, Compilation of Sandia Coal Devolatilization Data: Milestone Report. SAND92-8209, (1992).

[43] S.K. Ubhayakar, D.B. Stickler, C.W. Von Rosenberg, R.E. Gannon, Rapid devolatilization of pulverized coal in hot combustion gases, Symposium (International) on Combustion, 16 (1977) 427-436.

[44] T.H. Fletcher, A.R. Kerstein, R.J. Pugmire, D.M. Grant, Chemical percolation model for devolatilization. 2. Temperature and heating rate effects on product yields, Energ Fuel, 4 (1990) 54-60.

[45] R. Bassilakis, Y. Zhao, P.R. Solomon, M.A. Serio, Sulfur and nitrogen evolution in the Argonne coals. Experiment and modeling, Energ Fuel, 7 (1993) 710-720.

[46] S. Niksa, FLASHCHAIN Theory for Rapid Coal Devolatilization Kinetics. 6. Predicting the Evolution of Fuel Nitrogen from Various Coals, Energ Fuel, 9 (1995) 467-478.

[47] J.M. Jones, P.M. Patterson, M. Pourkashanian, A. Williams, A. Arenillas, F. Rubiera, J.J. Pis, Modelling NOx formation in coal particle combustion at high temperature: an investigation of the devolatilisation kinetic factors, Fuel, 78 (1999) 1171-1179.

[48] A. Williams, R. Backreedy, R. Habib, J.M. Jones, M. Pourkashanian, Modelling coal combustion: the current position, Fuel, 81 (2002) 605-618.

[49] R. Jovanovic, A. Milewska, B. Swiatkowski, A. Goanta, H. Spliethoff, Sensitivity analysis of different devolatilisation models on predicting ignition point position during pulverized coal combustion in O2/N2 and O2/CO2 atmospheres, Fuel, 101 (2012) 23-37.

[50] C.R. Shaddix, A. Molina, Particle imaging of ignition and devolatilization of pulverized coal during oxy-fuel combustion, P Combust Inst, 32 (2009) 2091-2098.

[51] A. Williams, M. Pourkashanian, J.M. Jones, Combustion of pulverised coal and biomass, Progress in Energy and Combustion Science, 27 (2001) 587-610.

[52] C.H. Priddin, Turbulent Combustion Modelling — A Review: A. Johansson, P.H. Alfredsson (Eds.) Advances in Turbulence 3, Springer Berlin Heidelberg, 1991, pp. 279-299.

[53] B.F. Magnussen, B.H. Hjertager, On mathematical modeling of turbulent combustion with special emphasis on soot formation and combustion, Symposium (International) on Combustion, 16 (1977) 719-729.

[54] P. Edge, S.R. Gubba, L. Ma, R. Porter, M. Pourkashanian, A. Williams, LES modelling of air and oxy-fuel pulverised coal combustion—impact on flame properties, P Combust Inst, 33 (2011) 2709-2716.

[55] M. Gharebaghi, R.M.A. Irons, L. Ma, M. Pourkashanian, A. Pranzitelli, Large eddy simulation of oxy-coal combustion in an industrial combustion test facility, International Journal of Greenhouse Gas Control, 5, Supplement 1 (2011) S100-S110.

[56] S. Black, J. Szuhánszki, A. Pranzitelli, L. Ma, P.J. Stanger, D.B. Ingham, M. Pourkashanian, Effects of firing coal and biomass under oxy-fuel conditions in a power plant boiler using CFD modelling, Fuel, 113 (2013) 780-786.

[57] J. Szuhánszki, S. Black, A. Pranzitelli, L. Ma, P.J. Stanger, D.B. Ingham, M. Pourkashanian, Evaluation of the Performance of a Power Plant Boiler Firing Coal, Biomass and a Blend Under Oxy-fuel Conditions as a CO2 Capture Technique, Energy Procedia, 37 (2013) 1413-1422.

[58] B. Magnussen, On the structure of turbulence and a generalized eddy dissipation concept for chemical reaction in turbulent flow, 19th Aerospace Sciences Meeting, American Institute of Aeronautics and Astronautics, 1981.

[59] N. Peters, Laminar flamelet concepts in turbulent combustion, Symposium (International) on Combustion, 21 (1988) 1231-1250.

[60] N. Peters, Turbulent Combustion, Cambridge University Press, 2000.

[61] S.B. Pope, PDF methods for turbulent reactive flows, Progress in Energy and Combustion Science, 11 (1985) 119-192.

[62] R.I. Backreedy, R. Habib, J.M. Jones, M. Pourkashanian, A. Williams, An extended coal combustion model, Fuel, 78 (1999) 1745-1754.

[63] L.D. Smoot, P. Smith, NO x Pollutant Formation in Turbulent Coal Systems, Coal Combustion and Gasification, Springer US, 1985, pp. 373-403.

[64] Y. Fei, S. Black, J. Szuhánszki, L. Ma, D.B. Ingham, P.J. Stanger, M. Pourkashanian, Evaluation of the potential of retrofitting a coal power plant to oxy-firing using CFD and process co-simulation, Fuel Processing Technology, 131 (2015) 45-58.

[65] R. Kurose, H. Makino, A. Suzuki, Numerical analysis of pulverized coal combustion characteristics using advanced low-NOx burner, Fuel, 83 (2004) 693-703.

[66] I.W. Smith, The combustion rates of coal chars: A review, Symposium (International) on Combustion, 19 (1982) 1045-1065.

[67] I.W. Smith, The intrinsic reactivity of carbons to oxygen, Fuel, 57 (1978) 409-414.

[68] R. Hurt, J.-K. Sun, M. Lunden, A Kinetic Model of Carbon Burnout in Pulverized Coal Combustion, Combustion and Flame, 113 (1998) 181-197.

[69] M. Gharebaghi, R.M. Irons, M. Pourkashanian, A. Williams, An investigation into a carbon burnout kinetic model for oxy–coal combustion, Fuel Processing Technology, 92 (2011) 2455-2464.

[70] C. Kuhr, M. Ehmann, S. Rehfeldt, C. Bergins, J. Maier, G. Scheffknecht, S. Wu, Modeling of char combustion in CO2/O2 and N2/O2 atmospheres, The 35th international technical conference on clean coal and fuel systems. Clearwater, FL, 2010.

[71] C. Fenimore, Formation of nitric oxide in premixed hydrocarbon flames, Symposium (International) on Combustion, Elsevier, 1971, pp. 373-380.

[72] F. Normann, K. Andersson, B. Leckner, F. Johnsson, Emission control of nitrogen oxides in the oxy-fuel process, Progress in Energy and Combustion Science, 35 (2009) 385-397.

[73] L. Álvarez, M. Gharebaghi, J.M. Jones, M. Pourkashanian, A. Williams, J. Riaza, C. Pevida, J.J. Pis, F. Rubiera, Numerical investigation of NO emissions from an entrained flow reactor under oxy-coal conditions, Fuel Processing Technology, 93 (2012) 53-64.

[74] L. Álvarez, M. Gharebaghi, J.M. Jones, M. Pourkashanian, A. Williams, J. Riaza, C. Pevida, J.J. Pis, F. Rubiera, CFD modeling of oxy-coal combustion: Prediction of burnout, volatile and NO precursors release, Applied Energy, 104 (2013) 653-665.

[75] J. Ahn, R. Okerlund, A. Fry, E.G. Eddings, Sulfur trioxide formation during oxy-coal combustion, International Journal of Greenhouse Gas Control, 5, Supplement 1 (2011) S127-S135.

[76] A.L. Brown, T.H. Fletcher, Modeling Soot Derived from Pulverized Coal, Energ Fuel, 12 (1998) 745-757.

[77] J. Hayashi, N. Hashimoto, N. Nakatsuka, H. Tsuji, H. Watanabe, H. Makino, F. Akamatsu, Soot formation characteristics in a lab-scale turbulent pulverized coal flame with simultaneous planar measurements of laser induced incandescence of soot and Mie scattering of pulverized coal, P Combust Inst, 34 (2013) 2435-2443.

[78] C.K. Stimpson, A. Fry, T. Blanc, D.R. Tree, Line of sight soot volume fraction measurements in air- and oxy-coal flames, P Combust Inst, 34 (2013) 2885-2893.

[79] W.J. Morris, D. Yu, J.O.L. Wendt, A comparison of soot, fine particle and sodium emissions for air- and oxy-coal flames, with recycled flue gases of various compositions, P Combust Inst, 34 (2013) 3453-3461.

[80] Theory Guide, ANSYS FLUENT, 2013.

[81] P. Cheng, Two-dimensional radiating gas flow by a moment method, Aiaa J, 2 (1964) 1662-1664.

[82] J.Y. Murthy, S.R. Mathur, Finite Volume Method for Radiative Heat Transfer Using Unstructured Meshes, Journal of Thermophysics and Heat Transfer, 12 (1998) 313-321.

[83] F.C. Lockwood, N.G. Shah, A new radiation solution method for incorporation in general combustion prediction procedures, Symposium (International) on Combustion, 18 (1981) 1405-1414.

[84] W. Richter, M. Heap, A Semistochastic Method for the Prediction of Radiative Heat Transfer in Combustion Chambers, Proceedings of the Spring Meeting of the Western States Section of the Combustion Institute, 1981.

[85] R. Johansson, B. Leckner, K. Andersson, F. Johnsson, Influence of particle and gas radiation in oxy-fuel combustion, International Journal of Heat and Mass Transfer, 65 (2013) 143-152.

[86] M.F. Modest, Radiative Heat Transfer (Third Edition), Academic Press, Boston, 2013.

[87] R.M. Goody, A statistical model for water-vapour absorption, Quarterly Journal of the Royal Meteorological Society, 78 (1952) 165-169.

[88] D.K. Edwards, A. Balakrishnan, Thermal radiation by combustion gases, International Journal of Heat and Mass Transfer, 16 (1973) 25-40.

[89] E.R.G. Eckert, Radiative transfer, H. C. Hottel and A. F. Sarofim, McGraw-Hill Book Company, New York, 1967. 52 pages, Aiche J, 15 (1969) 794-796.

[90] T.F. Smith, Z.F. Shen, J.N. Friedman, Evaluation of Coefficients for the Weighted Sum of Gray Gases Model, Journal of Heat Transfer, 104 (1982) 602-608.

[91] R. Johansson, K. Andersson, B. Leckner, H. Thunman, Models for gaseous radiative heat transfer applied to oxy-fuel conditions in boilers, International Journal of Heat and Mass Transfer, 53 (2010) 220-230.

[92] R. Johansson, B. Leckner, K. Andersson, F. Johnsson, Account for variations in the H2O to CO2 molar ratio when modelling gaseous radiative heat transfer with the weighted-sum-of-grey-gases model, Combustion and Flame, 158 (2011) 893-901.

[93] D. Edwards, A. GENLN, general line-by-line atmospheric transmittance and radiance model, NCAR Tech, Note TN-367-/-STR, Natl. Cent. for Atmos. Res., Boulder, Colo, 1992.

[94] T. Kangwanpongpan, F.H. França, R.C. da Silva, P.S. Schneider, H.J. Krautz, New correlations for the weighted-sum-of-gray-gases model in oxy-fuel conditions based on HITEMP 2010 database, International Journal of Heat and Mass Transfer, 55 (2012) 7419-7433.

[95] R. Porter, F. Liu, M. Pourkashanian, A. Williams, D. Smith, Evaluation of solution methods for radiative heat transfer in gaseous oxy-fuel combustion environments, Journal of Quantitative Spectroscopy and Radiative Transfer, 111 (2010) 2084-2094.

[96] A. Kempf, LES Validation from Experiments, Flow Turbulence Combust, 80 (2008) 351-373.

[97] F.G. Schmitt, About Boussinesq's turbulent viscosity hypothesis: historical remarks and a direct evaluation of its validity, Comptes Rendus Mécanique, 335 (2007) 617-627.

[98] P. Bradshaw, Possible origin of Prandt's mixing-length theory, Nature, 249 (1974) 135-136.

[99] S. P, A. S, A one-equation turbulence model for aerodynamic flows, 30th Aerospace Sciences Meeting and Exhibit, American Institute of Aeronautics and Astronautics, 1992.

[100] B.E. Launder, Lectures in mathematical models of turbulence [by] B. E. Launder and D. B. Spalding, Academic Press, London, New York, 1972.

[101] S.A. Orszag, V. Yakhot, W.S. Flannery, F. Boysan, D. Choudhury, J. Maruzewski, B. Patel, Renormalization group modeling and turbulence simulations, Near-wall turbulent flows, (1993) 1031-1046.

[102] T.-H. Shih, W.W. Liou, A. Shabbir, Z. Yang, J. Zhu, A new k-ϵ eddy viscosity model for high reynolds number turbulent flows, Computers & Fluids, 24 (1995) 227-238.

[103] L. Ma, J.M. Jones, M. Pourkashanian, A. Williams, Modelling the combustion of pulverized biomass in an industrial combustion test furnace, Fuel, 86 (2007) 1959-1965.

[104] R.I. Backreedy, L.M. Fletcher, L. Ma, M. Pourkashanian, A. Williams, Modelling Pulverised Coal Combustion Using a Detailed Coal Combustion Model, Combustion Science and Technology, 178 (2006) 763-787.

[105] D.C. Wilcox, Turbulence Modeling for CFD (Second Edition), DCW Industries, 1998.

[106] F.R. Menter, Two-equation eddy-viscosity turbulence models for engineering applications, Aiaa J, 32 (1994) 1598-1605.

[107] M.M. Gibson, B.E. Launder, Ground effects on pressure fluctuations in the atmospheric boundary layer, J Fluid Mech, 86 (1978) 491-511.

[108] B.E. Launder, G.J. Reece, W. Rodi, Progress in the development of a Reynolds-stress turbulence closure, J Fluid Mech, 68 (1975) 537-566.

[109] H.E. Stanley, Turbulence: The legacy of A. N. Kolmogorov, J Stat Phys, 88 (1997) 521-523.

[110] G. Erlebacher, M.Y. Hussaini, C.G. Speziale, T.A. Zang, Toward the large-eddy simulation of compressible turbulent flows, J Fluid Mech, 238 (1992) 155-185.

[111] J. Smagorinsky, GENERAL CIRCULATION EXPERIMENTS WITH THE PRIMITIVE EQUATIONS, Monthly Weather Review, 91 (1963) 99-164.

[112] M. Germano, U. Piomelli, P. Moin, W.H. Cabot, A dynamic subgrid-scale eddy viscosity model, Studying Turbulence Using Numerical Simulation Databases. 3: Proceedings of the 1990 Summer Program, 1990, pp. 5-17.

[113] D.K. Lilly, A proposed modification of the Germano subgrid ‐ scale closure method, Physics of Fluids A: Fluid Dynamics (1989-1993), 4 (1992) 633-635.

[114] F. Nicoud, F. Ducros, Subgrid-Scale Stress Modelling Based on the Square of the Velocity Gradient Tensor, Flow Turbulence Combust, 62 (1999) 183-200.

[115] A.G. Clements, S. Black, J. Szuhánszki, K. Stęchły, A. Pranzitelli, W. Nimmo, M. Pourkashanian, LES and RANS of air and oxy-coal combustion in a pilot-scale facility: Predictions of radiative heat transfer, Fuel, 151 (2015) 146-155.

[116] POST COMBUSTION CAPTURE (PCC), Global CCS Institute; https://www.globalccsinstitute.com/publications/co2-capture-technologies-post-combustion-capture-pcc, 2012.

[117] IPCC, Carbon Dioxide Capture and Storage, https://www.ipcc.ch/pdf/special-reports/srccs/srccs_wholereport.pdf, 2005.

[118] M.R. Abu-Zahra, Z. Abbas, P. Singh, P. Feron, Carbon dioxide post-combustion capture: solvent technologies overview, status and future directions, Materials and processes for energy: communicating current research and technological developments. Formatex Research Center, Badajoz, (2013) 923-934.

[119] A.B. Rao, E.S. Rubin, A Technical, Economic, and Environmental Assessment of Amine-Based CO2 Capture Technology for Power Plant Greenhouse Gas Control, Environ Sci Technol, 36 (2002) 4467-4475.

[120] S. Freguia, G.T. Rochelle, Modeling of CO2 capture by aqueous monoethanolamine, Aiche J, 49 (2003) 1676-1686.

[121] P.D. Vaidya, E.Y. Kenig, CO2-Alkanolamine Reaction Kinetics: A Review of Recent Studies, Chem Eng Technol, 30 (2007) 1467-1474.

[122] M. Caplow, Kinetics of carbamate formation and breakdown, J Am Chem Soc, 90 (1968) 6795-6803.

[123] H. Hikita, S. Asai, H. Ishikawa, M. Honda, The kinetics of reactions of carbon dioxide with monoethanolamine, diethanolamine and triethanolamine by a rapid mixing method, The Chemical Engineering Journal, 13 (1977) 7-12.

[124] R. Schneider, E.Y. Kenig, A. Górak, Dynamic Modelling of Reactive Absorption with the Maxwell-Stefan Approach, Chemical Engineering Research and Design, 77 (1999) 633-638.

[125] C. Noeres, E.Y. Kenig, A. Górak, Modelling of reactive separation processes: reactive absorption and reactive distillation, Chemical Engineering and Processing: Process Intensification, 42 (2003) 157-178.

[126] W.G. Whitman, The two film theory of gas absorption, International journal of heat and mass transfer, 5 (1962) 429-433.

[127] R. Higbie, The rate of absorption of a pure gas into still liquid during short periods of exposure, 1935.

[128] P.V. Danckwerts, Gas-liquid reactions, McGraw-Hill Book Co., 1970.

[129] H.M. Kvamsdal, J. Hetland, G. Haugen, H.F. Svendsen, F. Major, V. Kårstad, G. Tjellander, Maintaining a neutral water balance in a 450 MWe NGCC-CCS power system with post-combustion carbon dioxide capture

aimed at offshore operation, International Journal of Greenhouse Gas Control, 4 (2010) 613-622.

[130] X. Liu, J. Chen, X. Luo, M. Wang, H. Meng, Study on heat integration of supercritical coal-fired power plant with post-combustion CO2 capture process through process simulation, Fuel, 158 (2015) 625-633.

[131] T. Nagy, P. Mizsey, Model verification and analysis of the CO2-MEA absorber–desorber system, International Journal of Greenhouse Gas Control, 39 (2015) 236-244.

[132] A. Lawal, M. Wang, P. Stephenson, H. Yeung, Dynamic modelling of CO2 absorption for post combustion capture in coal-fired power plants, Fuel, 88 (2009) 2455-2462.

[133] C. Biliyok, A. Lawal, M. Wang, F. Seibert, Dynamic Validation of Model for Post-Combustion Chemical Absorption CO2 Capture Plant, B. Ian David Lockhart, F. Michael (Eds.) Computer Aided Chemical Engineering, Elsevier, 2012, pp. 807-811.

[134] A. Lawal, M. Wang, P. Stephenson, G. Koumpouras, H. Yeung, Dynamic modelling and analysis of post-combustion CO2 chemical absorption process for coal-fired power plants, Fuel, 89 (2010) 2791-2801.

[135] A. Lawal, M. Wang, P. Stephenson, O. Obi, Demonstrating full-scale post-combustion CO2 capture for coal-fired power plants through dynamic modelling and simulation, Fuel, 101 (2012) 115-128.

[136] Y. Hu, J. Yan, H. Li, Effects of flue gas recycle on oxy-coal power generation systems, Applied Energy, 97 (2012) 255-263.

[137] A. Haryanto, K.-S. Hong, Modeling and simulation of an oxy-fuel combustion boiler system with flue gas recirculation, Comput Chem Eng, 35 (2011) 25-40.

[138] B. Jin, H. Zhao, C. Zheng, Dynamic simulation for mode switching strategy in a conceptual 600 MWe oxy-combustion pulverized-coal-fired boiler, Fuel, 137 (2014) 135-144.

[139] A. Gopan, B.M. Kumfer, J. Phillips, D. Thimsen, R. Smith, R.L. Axelbaum, Process design and performance analysis of a Staged, Pressurized Oxy-Combustion (SPOC) power plant for carbon capture, Applied Energy, 125 (2014) 179-188.

[140] Y.R. Lee, H.S. Choi, H.C. Park, J.E. Lee, A numerical study on biomass fast pyrolysis process: A comparison between full lumped modeling and hybrid modeling combined with CFD, Comput Chem Eng, 82 (2015) 202-215.

[141] P.J. Edge, P.J. Heggs, M. Pourkashanian, P.L. Stephenson, A. Williams, A reduced order full plant model for oxyfuel combustion, Fuel, 101 (2012) 234-243.

[142] P.J. Edge, P.J. Heggs, M. Pourkashanian, P.L. Stephenson, Integrated fluid dynamics-process modelling of a coal-fired power plant with carbon capture, Applied Thermal Engineering, 60 (2013) 456-464.

[143] S. Black, Oxy-fuel Combustion for Carbon Capture using Computational Fluid Dynamics, University of Leeds, PhD, 2014.

[144] G. Coraggio, Measurement Equipment Suction Pyrometer. Technical Report, Doc. No. C76/y/1/17b, IFRF, (2009).

[145] P. Rosin, E. Rammler, The laws governing the fineness of powdered coal, Institute of Fuel, 7 (1933) 29-36.

[146] E.O. Agbonghae, T. Best, K.N. Finney, C.F. Palma, K.J. Hughes, M. Pourkashanian, Experimental and Process Modelling Study of Integration of a Micro-turbine with an Amine Plant, Energy Procedia, 63 (2014) 1064-1073.

[147] A document on the Didcot powerplant; https://www.rwe.com/web/cms/mediablob/en/97532/data/97538/4/rwe-npower/about-us/our-businesses/power-generation/didcot/dl-leaf.pdf.

[148] J.A. Mobsby, Thermal modelling of fossil-fired boilers, in: 1st UK Heat Transfer Conference, Leeds, 1984.

[149] http://www.psenterprise.com/power/ccs/gccs.html.

[150] B.E. Launder, D.B. Spalding, The numerical computation of turbulent flows, Computer Methods in Applied Mechanics and Engineering, 3 (1974) 269-289.

[151] T. Lundstedt, E. Seifert, L. Abramo, B. Thelin, Å. Nyström, J. Pettersen, R. Bergman, Experimental design and optimization, Chemometrics and Intelligent Laboratory Systems, 42 (1998) 3-40.

[152] D.D.D. Pinto, T.W. Brodtkorb, S.J. Vevelstad, H. Knuutila, H.F. Svendsen, Modeling of Oxidative MEA Degradation, Energy Procedia, 63 (2014) 940-950.

[153] A.J. Reynolds, T.V. Verheyen, S.B. Adeloju, A.L. Chaffee, E. Meuleman, Evaluation of methods for monitoring MEA degradation during pilot scale post-combustion capture of CO2, International Journal of Greenhouse Gas Control, 39 (2015) 407-419.

[154] S.J. Vevelstad, I. Eide-Haugmo, E.F. da Silva, H.F. Svendsen, Degradation of MEA; a theoretical study, Energy Procedia, 4 (2011) 1608-1615.

[155] G.S. Goff, G.T. Rochelle, Monoethanolamine Degradation: O2 Mass Transfer Effects under CO2 Capture Conditions, Ind Eng Chem Res, 43 (2004) 6400-6408.

[156] M.T. Luu, N. Abdul Manaf, A. Abbas, Dynamic modelling and control strategies for flexible operation of amine-based post-combustion CO2 capture systems, International Journal of Greenhouse Gas Control, 39 (2015) 377-389.

[157] A.S. Joel, M. Wang, C. Ramshaw, Modelling and simulation of intensified absorber for post-combustion CO2 capture using different mass transfer correlations, Applied Thermal Engineering, 74 (2015) 47-53.

[158] J. Rodriguez, A. Andrade, A. Lawal, N. Samsatli, M. Calado, A. Ramos, T. Lafitte, J. Fuentes, C.C. Pantelides, An Integrated Framework for the Dynamic Modelling of Solvent-based CO2 Capture Processes, Energy Procedia, 63 (2014) 1206-1217.

[159] R. Krishnamurthy, R. Taylor, A nonequilibrium stage model of multicomponent separation processes. Part I: Model description and method of solution, Aiche J, 31 (1985) 449-456.

[160] A. Gil-Villegas, A. Galindo, P.J. Whitehead, S.J. Mills, G. Jackson, A.N. Burgess, Statistical associating fluid theory for chain molecules with attractive potentials of variable range, The Journal of Chemical Physics, 106 (1997) 4168-4186.

[161] T. Lafitte, A. Apostolakou, C. Avendaño, A. Galindo, C.S. Adjiman, E.A. Müller, G. Jackson, Accurate statistical associating fluid theory for chain molecules formed from Mie segments, The Journal of Chemical Physics, 139 (2013) 154504.

[162] H.P. Mangalapally, H. Hasse, Pilot plant experiments for post combustion carbon dioxide capture by reactive absorption with novel solvents, Energy Procedia, 4 (2011) 1-8.

[163] F.A. Tobiesen, H.F. Svendsen, O. Juliussen, Experimental validation of a rigorous absorber model for CO2 postcombustion capture, Aiche J, 53 (2007) 846-865.

[164] R. Idem, D. Gelowitz, P. Tontiwachwuthikul, Evaluation of the Performance of Various Amine Based Solvents in an Optimized Multipurpose Technology Development Pilot Plant, Energy Procedia, 1 (2009) 1543-1548.

[165] T. Mejdell, T. Vassbotn, O. Juliussen, A. Tobiesen, A. Einbu, H. Knuutila, K.A. Hoff, V. Andersson, H.F. Svendsen, Novel full height pilot plant for solvent development and model validation, Energy Procedia, 4 (2011) 1753-1760.

[166] J.N. Knudsen, J.N. Jensen, P.-J. Vilhelmsen, O. Biede, Experience with CO2 capture from coal flue gas in pilot-scale: Testing of different amine solvents, Energy Procedia, 1 (2009) 783-790.

[167] R.E. Dugas, Pilot plant study of carbon dioxide capture by aqueous monoethanolamine, in, M.S.E thesis, University of Texas at Austin, USA, 2006.

[168] A. Lawal, Study of post-combustion CO2 capture for coal-fired power plant through modelling and simulation, in, Cranfield University, 2010.

[169] H.M. Kvamsdal, J.P. Jakobsen, K.A. Hoff, Dynamic modeling and simulation of a CO2 absorber column for post-combustion CO2 capture, Chemical Engineering and Processing: Process Intensification, 48 (2009) 135-144.

[170] PSE, gPROMS V3.6 Release Notes, (2012).

[171] ANSYS, ANSYS FLUENT Theory Guide, Release 14.0, (2011).

[172] P.J. Edge, P.J. Heggs, M. Pourkashanian, A. Williams, An integrated computational fluid dynamics–process model of natural circulation steam generation in a coal-fired power plant, Comput Chem Eng, 35 (2011) 2618-2631.

[173] T.F.W. S.P.Khare, R.P.Gupta, L.K.Elliott, B.J.P.Buhre, Retrofitting of a conventional coal fired plant to oxy-firing: heat transfer impacts for the

furnace and associated oxygen level, in: 5th Asia-Pacific Conference on Combustion, 2005.

[174] R.I. Backreedy, J.M. Jones, L. Ma, M. Pourkashanian, A. Williams, A. Arenillas, B. Arias, J.J. Pis, F. Rubiera, Prediction of unburned carbon and NOx in a tangentially fired power station using single coals and blends, Fuel, 84 (2005) 2196-2203.

[175] S. Brookes, J. Moss, Predictions of soot and thermal radiation properties in confined turbulent jet diffusion flames, Combustion and Flame, 116 (1999) 486-503.

[176] P. Edge, M. Gharebaghi, R. Irons, R. Porter, R.T.J. Porter, M. Pourkashanian, D. Smith, P. Stephenson, A. Williams, Combustion modelling opportunities and challenges for oxy-coal carbon capture technology, Chemical Engineering Research and Design, 89 (2011) 1470-1493.

[177] L. Ma, M. Gharebaghi, R. Porter, M. Pourkashanian, J.M. Jones, A. Williams, Modelling methods for co-fired pulverised fuel furnaces, Fuel, 88 (2009) 2448-2454.

[178] T. Kangwanpongpan, R. Corrêa da Silva, H.J. Krautz, Prediction of oxy-coal combustion through an optimized weighted sum of gray gases model, Energy, 41 (2012) 244-251.

[179] G. Krishnamoorthy, A new weighted-sum-of-gray-gases model for CO2–H2O gas mixtures, International Communications in Heat and Mass Transfer, 37 (2010) 1182-1186.

[180] V. Becher, A. Goanta, H. Spliethoff, Validation of spectral gas radiation models under oxyfuel conditions – Part C: Validation of simplified models, International Journal of Greenhouse Gas Control, 11 (2012) 34-51.

[181] M.B. Toftegaard, J. Brix, P.A. Jensen, P. Glarborg, A.D. Jensen, Oxy-fuel combustion of solid fuels, Progress in Energy and Combustion Science, 36 (2010) 581-625.

[182] S. Nakayama, Y. Noguchi, T. Kiga, S. Miyamae, U. Maeda, M. Kawai, T. Tanaka, K. Koyata, H. Makino, Pulverized coal combustion in O2/CO2 mixtures on a power plant for CO2 recovery, Energ Convers Manage, 33 (1992) 379-386.

[183] G. Scheffknecht, L. Al-Makhadmeh, U. Schnell, J. Maier, Oxy-fuel coal combustion—A review of the current state-of-the-art, International Journal of Greenhouse Gas Control, 5, Supplement 1 (2011) S16-S35.

[184] J.P. Smart, P. O'Nions, G.S. Riley, Radiation and convective heat transfer, and burnout in oxy-coal combustion, Fuel, 89 (2010) 2468-2476.

[185] D.J. Hersh, J.M. Abrardo, Air Separation Plant Design, Cryogenics, 17 (1977) 383-390.

[186] S. Posch, M. Haider, Optimization of CO2 compression and purification units (CO2CPU) for CCS power plants, Fuel, 101 (2012) 254-263.

[187] K.S. Bhambare, S.K. Mitra, U.N. Gaitonde, Modeling of a Coal-Fired Natural Circulation Boiler, Journal of Energy Resources Technology, 129 (2006) 159-167.

[188] Z.U. Hasan, Dynamic modelling and simulation for coal-fired boilers, University of Cranfield, MSc, 2008.

[189] E.J. Adam, J.L. Marchetti, Dynamic simulation of large boilers with natural recirculation, Comput Chem Eng, 23 (1999) 1031-1040.

[190] K.J. Åström, R.D. Bell, Drum-boiler dynamics, Automatica, 36 (2000) 363-378.

[191] J.A. Sidders, ANYDYM - a Fossil Fired Total Plant Model, CEGB report, 1989.

[192] T.E. Cormier, R. Agrawal, A.L. Prentice, D.W. Woodward, Production of ultra-high purity oxygen from cryogenic air separation plants, in, Google Patents, 1991.

[193] C.-t. Chou, C.-L. Wu, A.S.T. Chiang, A complementary pressure swing adsorption process configuration for air separation, Separ Technol, 4 (1994) 93-103.

[194] M.C. Campo, F.D. Magalhães, A. Mendes, Separation of nitrogen from air by carbon molecular sieve membranes, J Membrane Sci, 350 (2010) 139-147.

[195] D.-Y. Peng, D.B. Robinson, A New Two-Constant Equation of State, Industrial & Engineering Chemistry Fundamentals, 15 (1976) 59-64.

[196] A.K.D. B.F. Dodge, An investigation of the coexisting liquid and vapor phase of solutions of oxygen and nitrogen, Am. Chem. Soc, 49 (1927) 591-610.

[197] B.F. Dodge, Isotherms and isobars for air separation studies, Chem. Metall. Eng, 35 (1928) 622.

[198] B.H.L.B. B. Roffel, de Ruijter, Comput. Chem. Eng, 24 (2000) 111.

[199] M.H. G. Y. Zhu, L. Megan, Sep. Purif. Technol, 24 (2001).

[200] L. Zheng, Oxy-Fuel Combustion for Power Generation and Carbon Dioxide (CO_2) Capture, Woodhead Publishing Limited, UK, 2011.

[201] J. Xiong, H. Zhao, C. Zheng, Exergy Analysis of a 600 MWeOxy-combustion Pulverized-Coal-Fired Power Plant, Energ Fuel, 25 (2011) 3854-3864.

[202] X. Pei, B. He, L. Yan, C. Wang, W. Song, J. Song, Process simulation of oxy-fuel combustion for a 300MW pulverized coal-fired power plant using Aspen Plus, Energ Convers Manage, 76 (2013) 581-587.

[203] T.G. Chao Fu, Heat Integration of an Oxy-Combustion Process for Coal-Fired Power Plants with CO2 Capture by Pinch Analysis, Chemical Engineering Transactions, 21 (2010) 181-186.

[204] A.H. Al-Abbas, J. Naser, D. Dodds, CFD modelling of air-fired and oxy-fuel combustion of lignite in a 100KW furnace, Fuel, 90 (2011) 1778-1795.

[205] L. Álvarez, M. Gharebaghi, M. Pourkashanian, A. Williams, J. Riaza, C. Pevida, J.J. Pis, F. Rubiera, CFD modelling of oxy-coal combustion in an entrained flow reactor, Fuel Processing Technology, 92 (2011) 1489-1497.

[206] E.L.K. Buhre B. J. P., Sheng C. D., Gupta R. P., Wall T. F., Oxy-fuel combustion technology for coal-fired power generation, Progress in Energy and Combustion Science, 31 (2005) 283-307.

[207] M. Gharebaghi, R.M.A. Irons, L. Ma, M. Pourkashanian, A. Pranzitelli, Large eddy simulation of oxy-coal combustion in an industrial combustion test facility, International Journal of Greenhouse Gas Control, 5, Supplement 1 (2011) S100-S110.

[208] Z.C. Zhou Wu, Duan Lunbo, Liu Daoyin, Chen Xiaoping, CFD modeling of oxy-coal combustion in circulating fluidized bed, International Journal of Greenhouse Gas Control, 5 (2011) 1489-1497.

[209] I. Constenla, J.L. Ferrín, L. Saavedra, Numerical study of a 350MWe tangentially fired pulverized coal furnace of the As Pontes Power Plant, Fuel Processing Technology, 116 (2013) 189-200.

[210] P. Warzecha, A. Boguslawski, Simulations of pulverized coal oxy-combustion in swirl burner using RANS and LES methods, Fuel Processing Technology, 119 (2014) 130-135.

[211] S.R. Gubba, D.B. Ingham, K.J. Larsen, L. Ma, M. Pourkashanian, H.Z. Tan, A. Williams, H. Zhou, Numerical modelling of the co-firing of pulverised coal and straw in a 300MWe tangentially fired boiler, Fuel Processing Technology, 104 (2012) 181-188.

[212] S.E. Zitney, Process/equipment co-simulation for design and analysis of advanced energy systems, Comput Chem Eng, 34 (2010) 1532-1542.

[213] D. Sloan, W. Fiveland, S. Zitney, M. Syamlal, Power plant simulations using process analysis software linked to advanced modules, in: Proceedings of the 29th international technical conference on coal utilization & fuel systems, Clearwater, FL, 2004.

[214] L.I. Díez, C. Cortés, A. Campo, Modelling of pulverized coal boilers: review and validation of on-line simulation techniques, Applied Thermal Engineering, 25 (2005) 1516-1533.

[215] M.L. Stein, Interpolation of Spatial Data: Some Theory for Kriging, Springer, Chicago, USA, 1999.

[216] M.A. Lang Y. D., Biegler L. T., Munteanu S., Madsen J. I., Zitney S. E., Reduced Order Model Based on Principal Component Analysis for Process Simulation and Optimization, Energ Fuel, 23 (2009) 1695-1706.

[217] C. Thiart, A. Stein, Continental-scale kriging of gold-bearing commodities, Spatial Statistics, 6 (2013) 57-77.

[218] G. Jia, A.A. Taflanidis, Kriging metamodeling for approximation of high-dimensional wave and surge responses in real-time storm/hurricane risk assessment, Computer Methods in Applied Mechanics and Engineering, 261–262 (2013) 24-38.

[219] R.M. Sampson Paul D., Szpiro Adam A., Bergen Silas, Sheppard Lianne, Larson Timothy V., Kaufman Joel D., A regionalized national universal kriging model using Partial Least Squares regression for estimating annual PM2.5 concentrations in epidemiology, Atmos Environ, 75 (2013) 383-392.

[220] Z. Masoomi, M.S. Mesgari, M.B. Menhaj, Modeling uncertainties in sodium spatial dispersion using a computational intelligence-based kriging method, Computers & Geosciences, 37 (2011) 1545-1554.

[221] M.D. McKay, R.J. Beckman, W.J. Conover, A Comparison of Three Methods for Selecting Values of Input Variables in the Analysis of Output From a Computer Code, Technometrics, 42 (2000) 55-61.

[222] J. Antony, 6 - Full Factorial Designs, in: J. Antony (Ed.) Design of Experiments for Engineers and Scientists (Second Edition), Elsevier, Oxford, 2014, pp. 63-85.

[223] J. Antony, 7 - Fractional Factorial Designs, in: J. Antony (Ed.) Design of Experiments for Engineers and Scientists (Second Edition), Elsevier, Oxford, 2014, pp. 87-112.

[224] E.S.L. R.N. Kacker, J.J. Filliben, Taguchi's orthogonal arrays are classical designs of experiments, Research of NIST, 96 (1991) 577-591.

[225] Operating flexibly - Didcot A makes over 750 starts in one year, in, RWE Power International.

[226] A.H. Al-Abbas, J. Naser, D. Dodds, CFD modelling of air-fired and oxy-fuel combustion in a large-scale furnace at Loy Yang A brown coal power station, Fuel, 102 (2012) 646-665.